

Dang, Wenting (2018) *Stretchable interconnects for smart integration of sensors in wearable and robotic applications*. PhD thesis.

<https://theses.gla.ac.uk/40994/>

Copyright and moral rights for this work are retained by the author

A copy can be downloaded for personal non-commercial research or study, without prior permission or charge

This work cannot be reproduced or quoted extensively from without first obtaining permission in writing from the author

The content must not be changed in any way or sold commercially in any format or medium without the formal permission of the author

When referring to this work, full bibliographic details including the author, title, awarding institution and date of the thesis must be given

# **Stretchable Interconnects for Smart Integration of Sensors in Wearable and Robotic Applications**

**Wenting Dang**

A thesis submitted to

School of Engineering, University of Glasgow

*Doctor of Philosophy*

2018

## Abstract

Stretchable electronic systems are needed in realising a wide range of applications, such as wearable healthcare monitoring where stretching movements are present. Current electronics and sensors are rigid and non-stretchable. However, after integrating with stretchable interconnects, the overall system is able to withstand a certain degree of bending, stretching and twisting. The presence of stretchable interconnects bridges rigid sensors to stretchable sensing networks. In this thesis, stretchable interconnects focusing on the conductive polymer Poly (3,4-ethylenedioxythiophene): poly (4-styrenesulfonate) (PEDOT:PSS), the composite and the metallic-polyimide (PI) are presented. Three types of stretchable interconnects were developed including gold (Au) -PEDOT:PSS hybrid film interconnects, Graphite-PEDOT:PSS composite interconnects and Au-PI dual-layered interconnects. The Au-PEDOT:PSS hybrid interconnects' stretchability can reach 72%. The composite exhibits a stretchability of 80% but with an extremely high variation in resistance (100000%). The Au-PI interconnects that have a serpentine shape with the arc degree of  $260^\circ$  reveal the highest stretchability, up to 101%, and its resistance variation remains within 0.2%. Further, the encapsulation effect, cyclic stretching, and contact pad's influence, are also investigated.

To demonstrate the application of developed stretchable interconnects, this thesis also presents the optimised interconnects integrated with the electrochemical pH sensor and CNT-based strain sensor. The integrated stretchable system with electrochemical pH sensor is able to wirelessly monitor the sweat pH. The whole system can withstand up to 53% strain and more than 500 cycles at 30% strain. For the CNT-based strain sensor, the sensor is integrated on the pneumatically actuated soft robotic finger to monitor the bending radius (23 mm) of the finger. In this way, the movement of the soft robotic finger can be controlled. These two examples of sensor's integration with stretchable interconnects successfully demonstrate the concept of stretchable sensing network. Further work will focus on realising a higher density sensing and higher multifunctional sensing stretchable system seamlessly integrated with cloth fibres.

# Table of Contents

Abstract .....	2
List of Tables.....	6
List of Figures .....	7
Acknowledgement.....	13
Author's Declaration .....	14
Definitions/Abbreviations .....	15
Chapter 1 Introduction .....	16
1.1 Background and motivation .....	16
1.2 Objectives of the Ph.D. research .....	19
1.3 Structure of the thesis.....	20
1.4 Key contributions of this thesis.....	21
Chapter 2 State-of-the-art.....	23
2.1. Substrate Materials.....	25
2.2. Other materials .....	27
2.2.1. Semiconductors .....	27
2.2.2. Conductors .....	28
2.2.3. Geometry.....	38
2.4. Fabrication process.....	42
2.4.1. Microfabrication.....	42
2.4.2. Contact printing.....	43
2.4.3. Spray coating.....	43
2.4.4. Inkjet printing .....	44
2.4.5. Screen printing .....	44
2.4.6. Comparison between different printing technologies .....	45
2.5. Approaches adopted in this thesis .....	46
Chapter 3 Design, modelling and simulation .....	48
3.1 Bendability and stretchability .....	48



3.2 Thin film conductor on stretchable substrate .....	49
3.3 Serpentine-shaped interconnects .....	55
3.4 Electro-mechanical behaviour of interconnects .....	59
Summary .....	61
Chapter 4 Fabrication of stretchable interconnects .....	63
4.1 PDMS substrate and metallic thin film interconnects .....	63
4.2 Metal-conductive polymer hybrid film interconnects .....	68
4.2.1. PEDOT:PSS Spray-coating .....	71
4.2.2. PEDOT:PSS Spin-coating .....	74
4.3 Graphite-conductive polymer composite based interconnects .....	78
4.4 Metal-Polyimide dual layer transferable interconnects .....	81
Summary .....	83
Chapter 5 Characterisation of stretchable interconnects .....	86
5.1 Characterisation setup .....	86
5.2 Metallic thin film interconnects .....	87
5.3 Metal-conductive polymer hybrid film interconnects .....	90
5.4 Graphite-conductive polymer composite based interconnects .....	93
5.5 Metal-Polyimide dual layer transferrable interconnects .....	94
DC range characterisation .....	94
AC range characterisation .....	102
Summary .....	104
Chapter 6 Sensors' integration and applications .....	106
6.1 Stretchable system for sweat pH monitoring .....	106
6.1.1 Introduction .....	106
6.1.2 Experiments .....	108
6.1.3 Results and discussion .....	114
6.1.4 Conclusion .....	119
6.2 Stretchable strain sensor integrated on the soft robotic finger .....	120
6.2.1 Introduction .....	120

6.2.2 Fabrication and Integration .....	122
6.2.3 Conclusion .....	129
Summary .....	130
Chapter 7 Conclusion and future perspective .....	131
7.1 Conclusion .....	131
7.2 Future perspective .....	134
Bibliography.....	135

## List of Tables

Table 2.1: Comparison between popular substrates to integrate stretchable electronic systems based on their mechanical property, electrical property and chemical stability.....	26
Table 2.2: Comparison of various nanocomposites based on carbon fillers with respect to properties such as filler's size, percolation ratio, maximum conductivity, and mechanical elasticity. ....	34
Table 2.3: Comparison among various nanocomposites based on metal fillers in terms of properties such as filler's geometry, percolation ratio, maximum conductivity and mechanical elasticity. ....	36
Table 2.4: Comparison in inks' viscosity, thickness of printed film, resolution of printing and accuracy among spray coating, screen printing and inkjet printing technologies.....	46
Table 3.1: Geometry design of stretchable interconnects. ....	57
Table 3.2: Material parameters used in COMSOL simulation. ....	57
Table 4.1: Comparison of change in morphology of Ti-Au film under different oxygen plasma conditions.....	66
Table 4.2: Comparison of change in morphology of Au film under different oxygen plasma conditions. ....	67
Table 4.3: Comparison in contact angle with different methods of surface treatment on PDMS substrate.....	70
Table 4.4: Comparison of the optical microscope images of the spin-coated PEDOT:PSS on PDMS and their two-terminal resistance with different ratio of solvents.....	75
Table 4.5: Comparison between each fabrication process for different materials to realise stretchable interconnects. ....	84
Table 5.1: Comparison of the stretchability and resistivity variation between three different designs of interconnects with/without PEDOT:PSS underlying layer.....	92
Table 5.2: Comparison of electro-mechanical response among stretchable interconnects based on different materials. ....	105
Table 6.1: Analytes in blood, tears, and sweat with their diagnostic significance. ....	107

## List of Figures

Figure 1.1: A variety of applications of stretchable electronics in major directions including healthcare monitoring, energy and storage, e-skin for robotics, consumer electronics and telecommunication over the past decade.....	17
Figure 1.2: The IDTechEx report of technology readiness in stretchable electronics from 2018 to 2028.....	18
Figure 1.3: The trend from accumulated number of publications during the period from 1965 to 2020. The data was extracted from Web of science by searching keywords such as flexible electronics and stretchable electronics. ....	18
Figure 2.1: Architecture of stretchable electronic systems (a) fully stretchable layered structure (b) semi-stretchable system where stretchable interconnects are integrated with rigid device/sensors.....	23
Figure 2.2: Comparison of elastic property of various materials (including dielectric polymers, organic conductive polymers, metals and carbon materials) for stretchable interconnects with electrical conductivity.....	24
Figure 2.3: Schematic diagram of theory of (a) percolated network and (b) tunnelling effect between adjacent nanowires.....	31
Figure 2.4: Plot of reported data points collected from Table 2.2 and Table 2.3. (a) Correlation between the maximum conductivity and aspect ratio of fillers from various nanocomposites, (b) Correlation between percolation ratio and aspect ratio among various nanocomposites, (c) The trend of percolation ratio and stretchability with respect to aspect ratio for carbon-based nanocomposite, (d) The mapping of data points with the elastic modulus against the maximum conductivity.....	33
Figure 2.5: Various engineered geometries of stretchable interconnects which are sorted according to their maximum elongation ratio (stretchability) with respect to the scale of structure size achieved by different patterning technologies. ....	38
Figure 2.6: (a) Schematic representation of the geometric variation of serpentine-shaped conductor under stretching and (b) the theoretical strain after fully straightening of serpentine routing designs.....	40
Figure 2.7: Graphical illustration of common fabrication technologies for realising stretchable interconnects including (a) Microfabrication, (b) Transfer printing, (c) Contact printing, (d) Spray coating, (e) inkjet printing and (f) Screen printing.....	45
Figure 3.1: (a) Schematic illustration for the mechanics in a bar when it is subjected to (b) stretching and (c) bending movements. ....	48
Figure 3.2: Mechanical analysis model for metallic thin film deposited on soft substrate..	49

Figure 3.3: Calculation results from Matlab regarding the normal stress and shear stress that substrate and conductor experienced while stretching. ....	52
Figure 3.4: FEM simulation results: comparison between the resistance and maximum von Mises stress within the conductor when the Young's Modulus of (a) substrate was swept between 1 MPa to 10 GPa and (b) conductor was swept between 1 MPa and 100 GPa; Maximum von Mises stress in conductor with (c) the thickness of substrate varies from 0.04 mm to 1mm and (d) the thickness of conductor varies from 50 nm to 1200 nm when the dual-layered film is stretched up to 50%; Variation of resistance when the film is stretched up to 50% with a change in (e) substrate (f) conductor's thickness. ....	53
Figure 3.5: Schematic illustration for the mechanics in the serpentine-shaped conductor. ....	55
Figure 3.6: Boundary condition of the FEM model. ....	56
Figure 3.7: The concentrated von Mises stress and the location of maximum von Mises stress within different interconnects under 70% stretching. ....	58
Figure 3.8: (a) Resistance of stretchable interconnects with different geometry design during stretching, (b) The variation in resistance of stretchable interconnects with different geometry design up to 70% stretching. ....	58
Figure 3.9: Von Mises stress and resistance variation in serpentine-shaped interconnect under strain up to 100% when the thickness of interconnects vary from 100 nm to 1 $\mu$ m. ....	59
Figure 3.10: Calculation results of inductance and Q factor's variation of a straight conductor under external strain. ....	60
Figure 4.1: The binding mechanism between PDMS and silica (a) without surface modification, the hydrogen bond is formed and leads to strong adhesion between PDMS and silica surface, (b) the chlorotrimethylsilane (CH <sub>3</sub> ) <sub>3</sub> SiCl replaces the –OH bond with –SiCH <sub>3</sub> to reduce the adhesion and (c) the effect of oxygen plasma on PDMS surface with the introduce of –OH bond to convert hydrophobic PDMS surface into hydrophilic. ....	64
Figure 4.2: Fabrication process for depositing and patterning gold directly on PDMS substrate. ....	65
Figure 4.3: SEM image of patterned gold interconnect on PDMS substrate. ....	68
Figure 4.4: Schematic diagram of the cross-section view when Au-PEDOT:PSS dual-layer is under applied strain. The PEDOT:PSS underlying layer provides the electrical path in the cracks area. ....	69
Figure 4.5: Schematic representing the effect under an applied strain in interconnect with underlying layer of PEDOT:PSS. ....	69
Figure 4.6: Fabrication process flow by incorporating spray-coated PEDOT:PSS between gold conducting film with PDMS substrate. ....	71

Figure 4.7: (a) Measurement results in sheet resistance and thickness of spray-coated PEDOT:PSS layer and (b) optical image of spray-coated PEDOT:PSS film on PDMS substrate.....	72
Figure 4.8: SEM image of fabricated interconnects with part of gold film cracked and delaminated due to the peeling of underlying PEDOT:PSS film.....	73
Figure 4.9: Microscopic image of fabricated interconnects with the delamination of PEDOT:PSS film. ....	73
Figure 4.10: Optical microscopic image of fabricated Au-PEDOT:PSS interconnects. ....	74
Figure 4.11: TLM measurement for spin-coated PEDOT:PSS film on PDMS. ....	76
Figure 4.12: AFM scan at the edge of PEDOT:PSS film to estimate the thickness of the film. ....	77
Figure 4.13: (a) Image of Graphite-PEDOT:PSS composite that was spun-coated on 2-inch PDMS substrate and (b) Optical microscopic image of dispersed graphite powder within PEDOT:PSS film. ....	78
Figure 4.14: (a) Raman spectra of PEDOT:PSS film with Lorentz fitting curve, (b) Raman spectra of Graphite-PEDOT:PSS composite film with Lorentz fitting curve.....	79
Figure 4.15: (a) AFM images of PEDOT:PSS film on PDMS substrate and (b) AFM images of Graphite-PEDOT:PSS composite film on PDMS substrate. ....	80
Figure 4.16: Linear curve fitting of the measurement results during TLM measurement...	80
Figure 4.17: Fabrication process flow which adopts polyimide as transfer support layer...	81
Figure 4.18: Transfer patterned interconnect from Si wafer to PDMS substrate with the assistance of water-soluble tape. ....	82
Figure 5.1: Flowchart of Labview programme to synchronise the stepper motor and electrical measurement machines (Multimeter/LCR meter).....	86
Figure 5.2: Electro-mechanical measurement setup for stretchable interconnects. ....	87
Figure 5.3: (a) Photograph shows the strip of PDMS deposited with gold thin film, (b) microscopic image of gold thin film at the beginning of stretching (c) microscopic image of gold thin film while breaking and (c) resistance variation of gold film under stretching....	88
Figure 5.4: Resistance variation of patterned gold interconnects while stretched to failure. ....	89
Figure 5.5: Microscopic images of patterned Au interconnects (a) serp60 (b) serp260 on PDMS after stretching test. ....	89
Figure 5.6: (a) Schematic diagram of TLM measurement and (b) the comparison of TLM results between gold and gold-PEDOT:PSS hybrid film on PDMS substrate.....	90

Figure 5.7: (a-c) Optical images on the trend in crack propagation with an increasing of external strain, (d) the electrical response respects to the regions with different crack density. ....	91
Figure 5.8: Microscopic images of interconnects under failure strain with different design in curvature (a) 60° (b) 180°. ....	93
Figure 5.9: (a) Linear curve fitting of the measurement results during TLM measurement, (b) Recorded resistance of Graphite-PEDOT:PSS composite film under external strain....	94
Figure 5.10: (a) Resistance variation of stretchable interconnects with different designs and (b-f) the comparison between the experimental results and COMSOL simulation results..	95
Figure 5.11: Optical images of various interconnect geometries comparing the beginning stage under stretching and nearly breaking stage in stretching: (a-b) serp60; (c-d) serp45; (e-f) serp180; (g-h) serp260 and (i-j) triangle. ....	96
Figure 5.12: Comparison of stretchable interconnects with different geometry design in terms of their maximum strain (stretchability).....	98
Figure 5.13: Optical microscopic images of connection area of fabricated interconnects including (a) the interconnect made with the pad size of $7 \times 14 \text{ mm}^2$ , the inset image shows the broken connection when the interconnect failed under stretching, (b) the interconnect bonded with the pad size of $1 \times 1 \text{ mm}^2$ .....	98
Figure 5.14: Sequence of optical images of (a-c) encapsulated interconnects and (d-f) without encapsulated interconnects under increasing stretching strain. ....	100
Figure 5.15: Results in cyclic stretching of stretchable interconnects (a) without encapsulation and (b) with encapsulation. ....	101
Figure 5.16: Results in (a) inductance variation and (b) Q factor variation and their comparison with simulation results.....	101
Figure 5.17: Results in (a) inductance variation and (b) Q factor variation and their comparison with simulation results.....	102
Figure 5.18: Comparison in (a-b) inductance variation between different interconnect designs and (c-d) Q factor variation between different interconnect designs.....	103
Figure 6.1: (a) Photo of a stretchable wireless system for sweat pH monitoring, (b) Schematic diagram of a stretchable pH sensor with graphite-polyurethane composite SE, Ag/AgCl-based RE and a pair of stretchable interconnects. Schematic diagram of the fabrication process for (c) stretchable interconnects, (d) SE electrodes (e) assembly and encapsulation of sensor patch.....	109

Figure 6.2 (a) Circuit design and (b) system-level block diagram for wireless pH data transmission with the inset image of antenna design and (c) Fabrication steps of stretchable antenna. ....	112
Figure 6.3: (a) CV curve and (b) Nyquist plot for graphite-polyurethane composite electrode at pH 7 buffer solution and fitted curve based on Randles circuit model (c) impedance versus pH measured between SE and RE at selected frequencies (d) hysteresis in pH response and (e) response time of the sensor (f) potentiometric performance of the pH sensor. ....	115
Figure 6.4: (a) The electro-mechanical characterisation setup controlled with custom LabVIEW programme. The inset shows the birds-eye-view of stretchable pH sensor mounted on the setup. The sensor is symmetrically integrated with two interconnects. During stretching, only one side (one interconnect with working electrode) is monitored dynamically. (b) The variation in resistance across pH sensing electrode and stretchable interconnect with respect to the external strain experienced by the pH sensor. (c) Cyclic stretching test for stretchable pH sensor up to 30% strain. (d) Comparison in resistance variation between the first cycle of stretching and releasing and 500 <sup>th</sup> cycle. ....	117
Figure 6.5: (a) Screenshot of smartphone App “SenseAble” and (b) photo of real-time pH monitoring system including stretchable pH sensor in sweat equivalent solution, stretchable antenna and mobile monitoring App. ....	119
Figure 6.6: Schematic illustration of soft robotic finger with integrated strain sensor. The strain sensor is based on the CNT network. ....	122
Figure 6.7: Schematic illustration of 3D printed mould to fabricate the soft robotic finger. ....	123
Figure 6.8: Photos of fabricated soft robotic finger before and after pneumatically actuated. ....	123
Figure 6.9: Fabrication steps related to strain sensor: (a) spin coating of PI solution, (b) metal deposition on PI film, (c) photolithography patterning of stretchable interconnects, (d) etching, (e) transferring from Si carrier wafer to PDMS substrate (d) dissolving transfer tape in DI water and (g) DEP assembly of CNTs. ....	124
Figure 6.10: AFM measurement of assembled CNT network with three locations’ width measurement. ....	125
Figure 6.11: Variation in the resistance of DEP assembled CNT network with respect to (a) peak-to-peak voltage ( $V_{pp}$ ) under constant AC frequency of 1 MHz, and (b) AC frequency under constant $V_{pp}$ voltage of 10 V. ....	126
Figure 6.12: SEM images of DEP assembled CNT network near electrode with variations in $V_{pp}$ and AC frequencies. ....	126



Figure 6.13: Variation in the resistance of the strain sensor on the PDMS substrate and Ecoflex substrate under applied strain. ....	127
Figure 6.14: (a) Variation in the resistance of sensor under applied strain and (b) the resistance of sensor under five cycles of 11% strain.....	128
Figure 6.15: Real-time monitoring of the bending of soft robotic finger with integrated CNT based strain sensor.....	129
Figure 7.1: Illustration of the major materials presented in Chapter 2 for stretchable interconnects and the comparison with the developed stretchable interconnects in the thesis. ....	131
Figure 7.2: General comparison between stretchable interconnects with different materials. ....	133

## Acknowledgement

First of all, I would like to thank my supervisor, Prof. Ravinder Dahiya, for providing me the opportunity to join the CONTEST-ITN project. Thank you for all the valuable guidance, suggestions and encouragements during the past four years. This experience helps me to become a better researcher.

I would also like to thank my second supervisor Dr. Leandro Lorenzelli. I thank him for his valuable guidance and support he offered. I would also like to thank him for his hospitality during my secondment in Fondazione Bruno Kessler (FBK). I am grateful for his hiking training, which has given me many great memories. I would also like to thank my third supervisor Dr. Vincenzo Vinciguerra. Thanks for hosting me in ST microelectronics in Catania. It was a great experience for me.

The work in this thesis was carried out from two labs: the lab from the Centre for Materials and Microsystems at Fondazione Bruno Kessler (FBK) and the James Watt Nanofabrication Centre at University of Glasgow. I owe my deepest gratitude to everyone from the labs and group for their help and support during my PhD period. Particularly, I would like to thank my colleagues: Dr. Sajina Tinku, Dr. Saleem Khan, Dr. William Taube Navaraj and Anton Polishchuk for all the support. I also extend my thanks to Dr. Dhayalan Shakthivel for his advice in research as well as in thesis writing. I am also deeply grateful to Dr. Libu Manjakkal for his guidance on the electrochemical sensors.

The special acknowledgement goes to Shoubhik Gupta and Nivasan Yogeswaran for our common experience in this special PhD programme. Thank you both for the enormous support throughout the years. You both made the working environment positive and full of joy.

At last, I would like to thank my parents for their unconditional way of supporting me in any decision I have taken. In particular, I would like to express my thanks and love to my mom, Dr. Yushu Xie, for her advice and accompany during the past many years.

## **Author's Declaration**

I declare that, except where explicit reference is made to the contribution of others, this thesis is the result of my own work and has not been submitted for any other degree at the University of Glasgow or any other institution.

Wenting Dang

## Definitions/Abbreviations

<b>AFM</b>	Atomic Force Microscopy
<b>CV</b>	Cyclic voltammetry
<b>DC/AC</b>	Direct current/Alternative current
<b>DEP</b>	Dielectrophoresis
<b>DMSO</b>	Dimethyl sulfoxide
<b>EG</b>	Exfoliated graphite
<b>FEM</b>	Finite Element Methods
<b>GNPs</b>	Graphene Nanoplatelets
<b>HF</b>	Hydrogen fluoride
<b>IPA</b>	Isopropanol
<b>KI</b>	Potassium Iodide
<b>MEMS/CMOS</b>	Micro-Electro-Mechanical Systems/ Complementary metal–oxide–semiconductor
<b>PANi</b>	Polyaniline
<b>PDMS</b>	Polydimethylsiloxane
<b>PEDOT: PSS</b>	Poly (3,4-ethylenedioxythiophene)-Poly (styrenesulfonate)
<b>PI</b>	Polyimide
<b>PMMA</b>	Poly(methyl methacrylate)
<b>PU</b>	Polyurethane
<b>RIE</b>	Reactive Ion Etching
<b>RFID</b>	Radio frequency identification
<b>SDS</b>	Sodium dodecyl sulfate
<b>SEBS</b>	Polystyrene-block-poly(ethylene-ran-butylene)-block-polystyrene
<b>SE</b>	Sensing electrode
<b>SEM</b>	Scanning Electron Microscopy
<b>SWNT</b>	Single-Walled Carbon Nanotubes
<b>TLM</b>	Transfer Line Measurement
<b>1D/2D</b>	One dimensional/ two dimensional

# Chapter 1 Introduction

## 1.1 Background and motivation

Stretchable electronics, as the emerging technology, have shifted the paradigm in electronics due to their wide range of applications such as healthcare monitoring [1]–[5], energy and storage [6]–[9], e-skin for robotics [10]–[13], consumer electronics [14]–[17] and telecommunications [18]–[21]. The trend of the development in stretchable electronics, which can be recognised as part of the “More than Moore” concept, which aims to develop electronic devices that incorporate more functionalities and can help people interact with the changing environment [22]. **Figure 1.1** shows several examples of stretchable electronics throughout the past decade when the development of stretchable electronics came into being. Healthcare monitoring has been benefiting extensively from stretchable electronics due to its requirement of a close interaction between human and electronics devices. The conformability or stretchability of healthcare monitoring devices can improve the reliability to collect non-invasive physiological parameters including heart rate, blood pressure, skin temperature, respiration rate and electrolyte concentration in body fluids [23]–[26]. Non-invasive systems for diagnosis and health monitoring (particularly for chronic illness) will have a major impact on healthcare practices, as patients are likely to be more compliant with such methods [27]. These non-invasive wearable electronics are also attracting a lot of attention due to ease of use.

Aiming at integrating a power supplying system in stretchable electronics, stretchable energy harvesting and storage system has started to attract huge attentions recently. The energy harvesting and storage system include smart battery, supercapacitor, piezoelectric power generation, and triboelectric power generation. Stretchable energy harvesting systems are often realised either through solar energy or kinetic energy [6]–[9]. Another application of stretchable electronics is the electronic skin (e-skin) for robotics. Robotics has been adopted in many fields, such as precise manufacturing, harvesting in agriculture and manoeuvring /exploring under extreme environment [28], [29]. Current robotics are programmed and controlled through computers with accurate programming instructions. However, they lack the accurate and real-time sensing feedback from the working environment, and this restricts them in providing a dynamic response. Those feedbacks can be tactile sensing, proximity sensing and extended to chemical sensing. In order to obtain the sensing information, the concept of “e-skin” was proposed to integrate multifunctional sensors with robotics. Rather than using traditional rigid electronics, stretchable electronics

could withstand certain deformation and ensure the electronics' performance even when robotics are moving, holding objects and gesturing. Such applications of e-skin can also be expanded for soft robotics. Unlike rigid-body robots that have restricted movements due to stiff joints, soft robotics expand their degree of freedom and allow them to perform complex movements of bending, wrinkling, buckling, and twisting. They are light in weight and soft

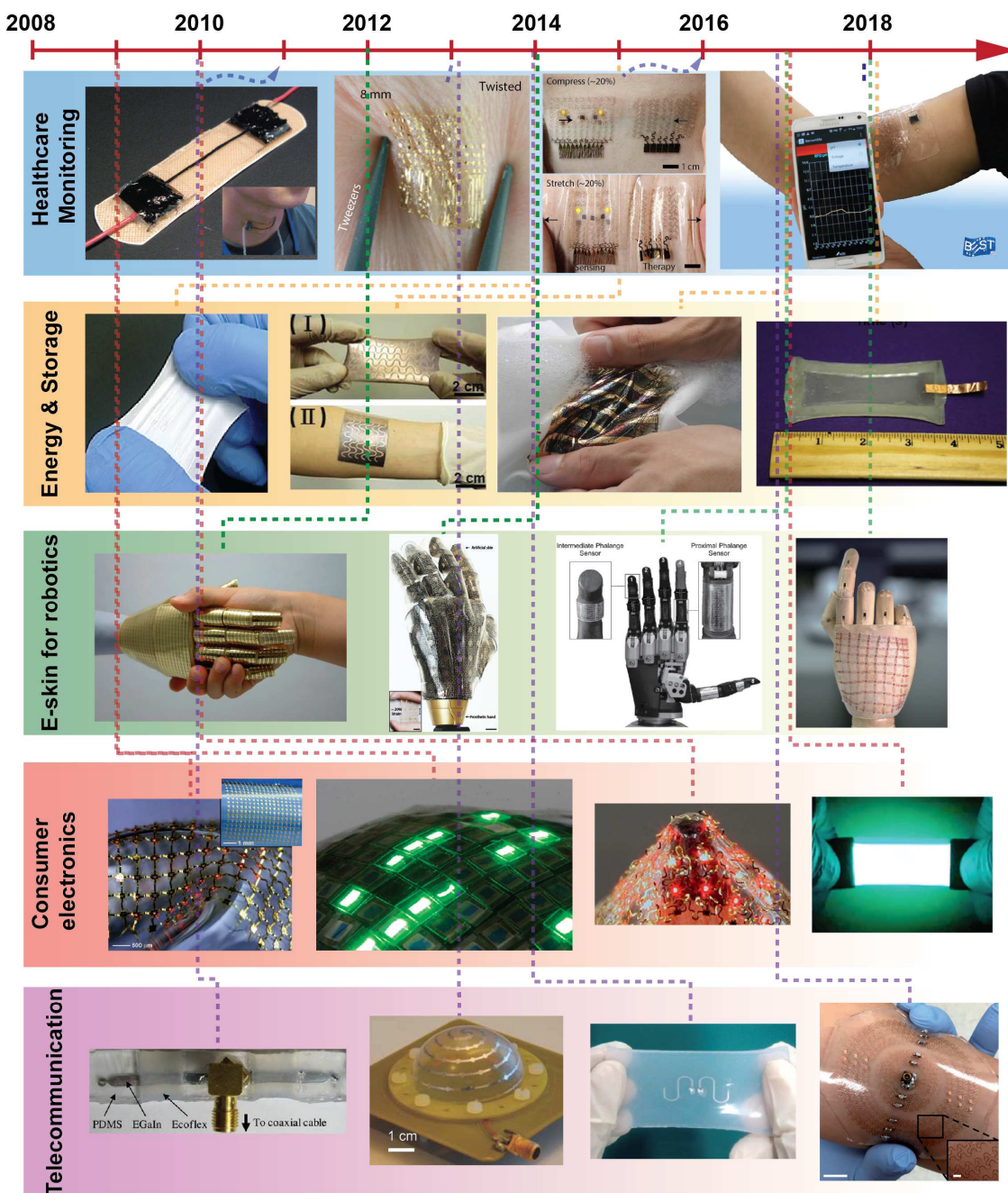


Figure 1.1: A variety of applications of stretchable electronics in major directions including healthcare monitoring, energy and storage, e-skin for robotics, consumer electronics and telecommunication over the past decade. Reprinted and adapted with permission, [1], [3], [5], [9-10], [12], [14], [16] copyright © Springer Nature, [2], [15] copyright © AAAS, [7-8], [11], [18-20] copyright © Wiley, [6], [21] copyright © RSC Publishing, [13] copyright © Cambridge University Press, [17] copyright © American Chemical Society.



**Figure 1.2** summarised the current technology in stretchable electronics in terms of the materials, components (sensors) and system, with their development stages [30]. In materials, the stretchable conductive inks have developed to an early commercial sales stage. These inks are mainly made from silver and carbon conductive particles. However, the biocompatibility issue of the commercial stretchable inks restrict their applications in wearable electronics. Some physical sensors including resistive sensors and inductive sensors have shifted from the proof of concept stage to maturity. However, most of the stretchable electronics at system level are still in the proof of concept and early prototype stages, such as stretchable energy storage and harvesting system and stretchable logic circuit system. In particular, the stretchable sensor systems, which integrated with energy supplying and data transmission modulus, have not yet developed to the proof of concept stage. This gap calls for a further investigation on stretchable electronics. Such a trend can also be reflected by the evidence of the exponential growth in publications in the field of stretchable electronics, especially in the past decade, as can be seen from **Figure 1.3**. In terms of an annual number of publications, stretchable electronics are expected to attract more than 5600 papers by the year 2020.

Amongst the components in stretchable electronics, stretchable interconnects play an important role due to their capability of providing traditional rigid electronic systems with an extra degree of freedom while retaining their electrical performance. Particularly in applications where large deformations are experienced at unconventional surfaces, such as the knees and elbows of a humanoid robot, where the need for tactile skin has been highlighted by many researchers [31]–[34], stretchable interconnects are indispensable. In another case where high-density sensing is required, the stretchable interconnects can connect each sensing pixel to allow distributive sensing. For example, an array of temperature sensors connected by stretchable interconnects allows distributed sensing over a curved and deformable surface [1], [35]. Current challenges still remain in the dilemma between the high electrical performance and the mechanical softness of electronics.

## 1.2 Objectives of the Ph.D. research

The general objectives of this thesis are to understand, design and characterise stretchable interconnects and their integration with sensors. The detailed major objectives are:



1. To understand the mechanism of stretchable interconnects, with respect to the structural mechanics of the deposited conductive films and stretchable substrate
2. To understand the relationship between the mechanical deformation and variation in electrical performance of interconnects
3. To investigate conductive materials that can withstand a certain degree of deformation
4. To optimise the fabrication process with conventional/unconventional materials for stretchable interconnects
5. To characterise the fabricated interconnects with various methodologies including uni-axial stretching, sheet resistance measurement, surface morphological measurement
6. To integrate stretchable interconnects with sensors in order to develop novel applications

### **1.3 Structure of the thesis**

This thesis is planned as follows: Chapter 2 introduces the state-of-the-art technologies on stretchable electronics. In particular, more discussion is about the conductive materials including conductive polymers, metal liquids and composites, which are the materials that have been used for stretchable interconnects. Different geometry designs and fabrication process for interconnects are also included in Chapter 2. This chapter obtained the object 3 in the previous section.

Chapter 3 discusses the mechanical and electrical analysis of stretchable interconnects. These analysis include the mechanical and mathematical modelling and Finite Element Methods (FEM) simulation (COMSOL). This chapter provides the theoretical support and guides for the design of stretchable interconnects. This chapter reached the object 1&2 in the previous section.

Chapter 4 presents stretchable interconnects' fabrication process. In this chapter, the fabrication processes of stretchable interconnects, which are made from gold (Au) thin film, Au-PEDOT:PSS hybrid film, graphite-PEDOT:PSS composite and Au-Polyimide (PI), are

optimised with the assistance of different methodologies. These methodological techniques include Atomic Force Microscopy (AFM), Raman spectroscopy, Scanning Electron Microscopy (SEM), high-resolution microscopy and optical/physical surface profilometry. The major fabrication process of interconnects includes the microfabrication process and spray-coating. This chapter aligned with the object 4 in the previous section.

Chapter 5 provides the results of the electro-mechanical characterisation of the fabricated stretchable interconnects. The chapter first introduces the setup system for electro-mechanical characterisation of interconnects. Then the interconnects based on Au thin film, Au-PEDOT:PSS hybrid film, graphite-PEDOT:PSS composite and Au-PI are characterised to obtain the ultimate strain before failure. More characterisations on Au-PI based interconnects are carried out including the encapsulation test, cyclic stretching test and different bond pad design test. In addition, the Au-PI based interconnects are characterised under AC condition. This chapter met the object 5 in the previous section.

Chapter 6 demonstrates the applications of stretchable interconnects that integrate with sensors. In this chapter, two applications are demonstrated, including stretchable sweat pH monitoring system and strain monitoring system of soft robotic fingers. This chapter realised the object 6 in the previous section. Following this chapter, the thesis will end with the conclusion and future perspective in Chapter 7.

## 1.4 Key contributions of this thesis

The key contributions of this thesis can be summarised as follows:

- The mechanical and electrical analysis of stretchable interconnects is carried out, which are important for material selection and interconnects' geometry designs.
- The optimised fabrication process is developed for stretchable interconnects through microfabrication technology. The interconnects are made from Au thin film, Au-PEDOT:PSS hybrid film and Au-PI dual layer. The Au thin film based interconnects exhibit a limited stretchability, which are not a suitable candidate for stretchable interconnects.
- The stretchable interconnects based on the hybrid film of Au and conductive polymer PEDOT:PSS show a higher stretchability, which is up to 72%.

- The stretchable interconnects based on Au-PI are suitable candidates for stretchable interconnects due to their higher stretchability (101%) and lower resistance variation (0.2%).
- The composite graphite-PEDOT:PSS also reveals high stretchability, which can reach 80%. However, the electrical performance of such material indicates an unstable behaviour under large strain. The variation of their resistance can reach 100000% at 80% strain.
- Two applications of the Au-PI based stretchable interconnects integrated with sensors are successfully demonstrated. One of the applications is on wearable electronics, when the stretchable interconnects are integrated with pH sensor. The whole system can be applied to monitor sweat pH. The other application is on soft robotics, where the interconnects are integrated with CNT-based strain sensor. This application allows the movement of the soft robotic finger to be monitored.

## Chapter 2 State-of-the-art

Common strategies to achieve stretchable electronic systems can be categorised into two type of architectures: the fully stretchable system and the semi-stretchable system, as illustrated in **Figure 2.1**. The fully stretchable system refers to the multilayered integration of various materials including the stretchable conductor, stretchable active materials/semiconductor and stretchable dielectrics. These materials exhibit excellent electrical performance, such as the soft conductor that can be compared to metal and the stretchable semiconductor that can be compared to silicon. In the meantime, these materials are able to regain their shapes after large deformations including stretching, bending and twisting [36]. The semi-stretchable system can also be described as a “bridge-island” structure, of which the “island” refers to the rigid electronic devices or sensors and the “bridge” is the stretchable interconnect. Unlike the fully stretchable systems where most layers (electrode, semiconducting/active material and dielectric) are monolithically integrated, semi-stretchable electronics system integrate devices and interconnect with the assistance of additional solder joints. In this system, the overall system can also withstand certain movement where the generated strain will concentrate on stretchable interconnects, but not on rigid electronic devices.

Aside from the architecture of stretchable electronic systems, the mechanical and electrical properties of materials play a vital role in establishing such systems. Traditionally, metals such as gold (Au) and copper (Cu) have been preferred for interconnects and electrodes, owing to their high electrical and thermal conductivity that permits the passage of large current and efficient transmission of signals. However, these metals have been found

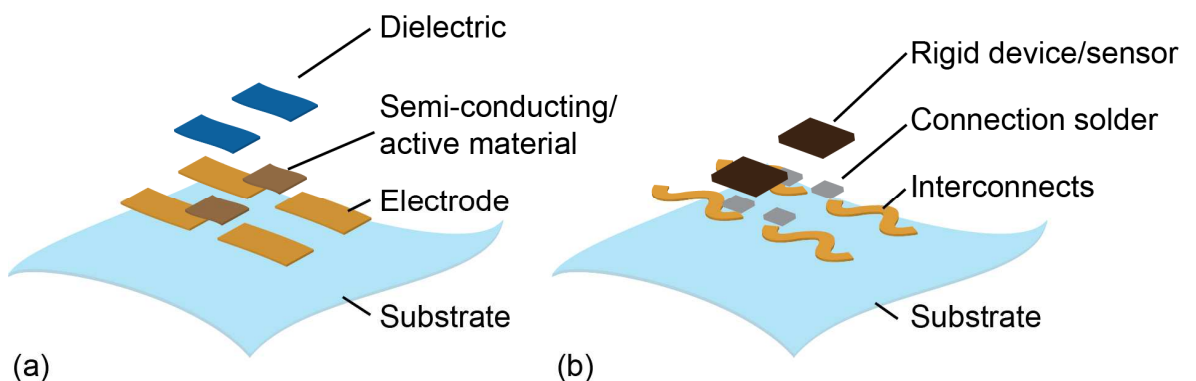


Figure 2.1: Architecture of stretchable electronic systems (a) fully stretchable layered structure (b) semi-stretchable system where stretchable interconnects are integrated with rigid device/sensors.

to have limited use for the stretchable system due to their limited elastic properties [37], [38]. As shown in **Figure 2.2**, metals, such as Au, Cu, and Ag exhibit an elastic modulus of about 100 GPa and a high electrical conductivity in the range of  $10^9$  S/m. On the other hand, highly stretchable elastomers, such as PDMS, PU, and Ecoflex, which are widely used as highly stretchable substrates, exhibit an elastic modulus below 1 MPa. Unlike traditional metals and polymeric substrates, conductive polymers, such as polyaniline (PANi) [39] and poly(3,4-ethylenedioxythiophene): poly(4-styrenesulfonate) (PEDOT: PSS) [40] have both moderate electrical conductivity and elastic modulus. Other materials, such as composite, exhibit high electrical conductivity and elasticity through mixing highly conductivity fillers (i.e. CNTs, graphene, AgNWs) with soft polymer matrix (i.e. PDMS, Ecoflex) [41], [42]. As illustrated in **Figure 2.2**, the high conductivity fillers (i.e. CNTs) exhibit high elastic modulus while most polymers, which are compliant to human skin due to similar softness, are insulating. The composite structure takes the advantages of high conductivity from fillers and softness from the polymers. Efforts have been made by researchers to further improve the behaviour of such composites through more efficient filler dispersion and solvent selection.

In the following sections, the further review on widely used stretchable substrates and stretchable materials including semiconductors and conductors will be presented. A more

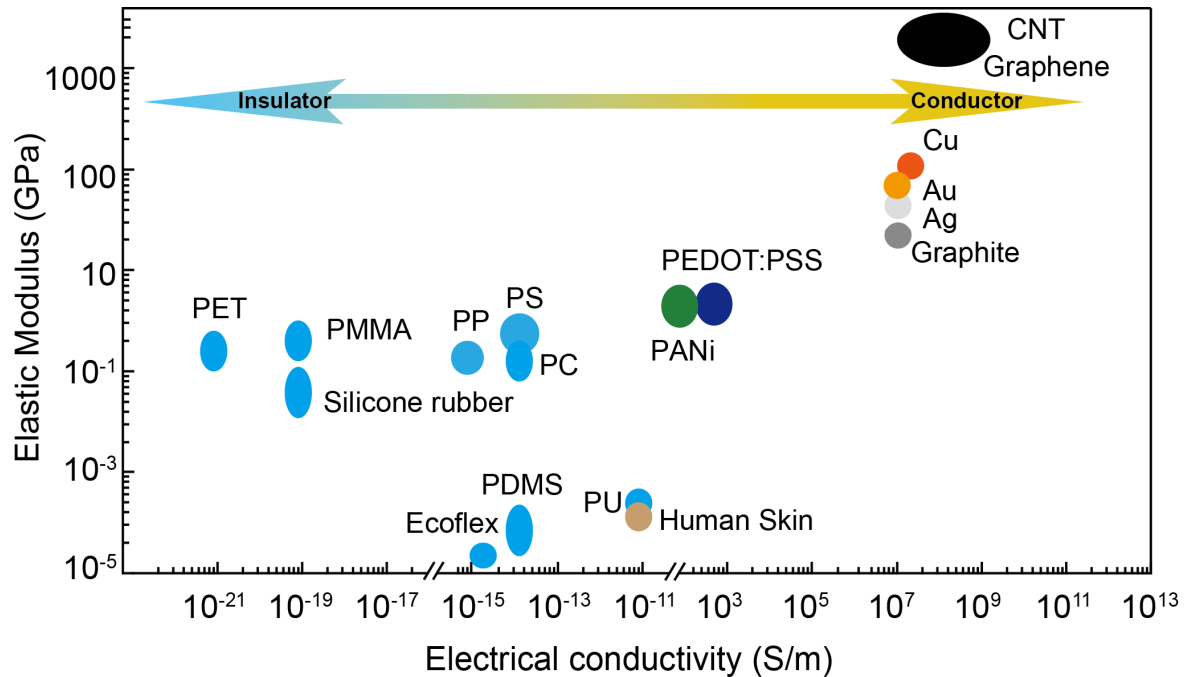


Figure 2.2: Comparison of elastic property of various materials (including dielectric polymers, organic conductive polymers, metals and carbon materials) for stretchable interconnects with electrical conductivity.

focused review on stretchable conductors regarding their geometries, materials and fabrication process will also be included.

## 2.1. Substrate Materials

Stretchable electronic systems are usually utilising hyper-elastic polymer as a substrate. The widely used polymers include PDMS [43], Polyurethane [44], Ecoflex [45], Parylene [9] and Polystyrene-block-poly(ethylene-ran-butylene)-block-polystyrene (SEBS) [36]. PDMS (Sylgard 184, Dow Corning, U.S) is a widely-used substrate material in which Young's modulus is tuneable with the varied ratio of base polymer and its crosslink agent. For example, a 10:1 ratio of base and crosslink PDMS is recommended by the manufacturer and its Young's modulus is 7.1 MPa, which is provided by the datasheet [46]. However, the actual Young's modulus may vary depending on the curing temperature during process, as well as the ratio between PDMS base polymer and the crosslink agent. As reported, the PDMS film is generally cured under 25°C and exhibits Young's modulus of 1.3 MPa, while the film cured under 200°C has Young's modulus of 2.97 MPa [47]. This data indicates that the low curing temperature can lead to a softer PDMS film. The amount of crosslinking agent while preparing the pre-polymer PDMS is vital for the mechanical property in PDMS film. When the ratio between PDMS base polymer and the crosslinking agent is increasing (e.g. from 10:1 to 15:1 and 20:1), the resulting PDMS will become much softer [43]. The chemical stability and physical properties of PDMS are compared with other polymers (**Table 2.1**). In comparison, PDMS is biocompatible and resistant to most of the alcohol, acid, and base. In addition, it is optically transparent throughout the visible spectrum down to 240 nm. Hence, PDMS is a popular candidate to be applied as encapsulation for implants [48][49], replicable mold in soft lithography [50] and microfluidic systems [51]. Another elastic polymer that is widely used for the stretchable substrate is Ecoflex® (Smooth-on, U.S), which is chemically termed as Polybutylene adipate terephthalate (PBAT). Unlike the transparent PDMS, Ecoflex is translucent. Ecoflex exhibits a compostable feature [52], which benefits in biodegradable electronics. The ultimate strain test indicates that the PDMS substrate can easily be stretched up to 150% longer than its original length, while the Ecoflex can be easily stretched to 650% without breaking [53]. Polyurethane is a common polymer that can be found in daily life, such as in cleaning foams, tubing, and vanish paint. The thermoplastic polyurethanes have good mechanical properties which can also be used for the stretchable substrate. Compared with PDMS and Ecoflex, the polyurethane is less compatible with solvents such as ethanol, isopropanol and other high-polar organic solvents [54]. SEBS draws the attention of researchers for its elastic property. In addition, due to its tuneable

viscosity under a levitated process temperature, it can be thermally drawn into fibres, which can be further integrated into wearable electronic applications [55]. Parylene, as a biocompatible material, is often used as an encapsulation layer for implants. It is highly resistant to acid and base solution and most of the solvents [56][57]. However, the stretchability of parylene is less, when compared with other polymers. Polyimide has a relatively higher strength, with the highest Young's modulus among all the polymer substrates. It is robust and can withstand a higher temperature (300°C), which makes it popular for flexible PCB substrate. Amongst the reviewed polymeric substrate, the PDMS has the advantage of chemically stable and biocompatible. In addition, its mechanical property is tuneable, which can meet different requirements. Compared with other expensive polymer (e.g. Polyimide from HD Microsystem costs around £747 for 1 kg), PDMS costs around £170 for 1 kg. Hence, the PDMS was chosen as the substrate in this thesis.

Table 2.1: Comparison between popular substrates to integrate stretchable electronic systems based on their mechanical property, electrical property and chemical stability.

Substrate materials	Young's modulus	Elongation at break (Stretchability)	Dielectric constant (at 1kHz)	Chemical compatibility
<b>PDMS</b>	1-7 MPa [43]	150% [53]	2.32-2.4 [58]	Biocompatible, low solubility in most alcohols, compatible with acid and base [59]
<b>Polybutylene adipate terephthalate (Ecoflex)</b>	22 kPa [21]	650% [53]	2.1 [21]	Biocompatible, biodegradable [52]
<b>Polyurethane</b>	1.1 MPa [60]	200% [61]	5.68 [60]	Swelled in alcohols such as ethanol and isopropanol, dissolved in the high polar organic solvent, resistant to diluted base and acid, biocompatible [62][63]

<b>SEBS</b>	10- 100MPa [64][65]	700% [64][55]	2.45 [65]	Dissolved in polar organic solvent, did not dissolve in acetone, methanol and DMSO [66]
<b>Parylene-C</b>	1.3-3.5 GPa [67]	18% [67]	3.1 [68]	Resistant to acid and base, low solubility in most alcohols Biocompatible [69]
<b>Polyimide</b>	2.84 GPa [70]	19% [70]	3.1-3.4 [71]	Resistant to most solvents and chemicals, biocompatible [56][57]

## 2.2. Other materials

The commonly used stretchable materials consist of semiconductors and conductors. Those materials are either intrinsically stretchable or can be engineered into a serpentine shape to increase its stretchability. In the following subsections, a review on stretchable materials including carbon-based nanomaterials (i.e. graphene, CNTs), semiconducting nanowires (i.e. SiNWs), conductive polymers (i.e. P3HT, PANI, PEDOT), metal liquid (i.e. EGaIn) and nanocomposite (i.e. MWCNTs-PDMS, AgNWs-PDMS) regarding their electromechanical properties, will be presented. Various engineered geometries designed to increase the stretchability in electronic systems will also be discussed.

### 2.2.1. Semiconductors

So far, research on stretchable semiconducting material have focused on silicon nanowires/nanoribbons [10], [72], [73], polymer-based semiconductor [36], [74], [75], carbon-based nanomaterials (graphene [76], CNTs [77]). Silicon, as a widely used semiconducting material, has been exploited to improve the device's performance regarding carrier mobility, transit frequency and  $I_{on}/I_{off}$  ratio. Reported device based on monocrystalline silicon can reach a mobility of  $1200 \text{ cm}^2\text{V}^{-1} \text{ s}^{-1}$  and an  $I_{on}/I_{off}$  ratio in the range of  $10^9$  [78]. In order to modify a non-stretchable and inorganic semiconductor, such as silicon, into deformable and stretchable, change in morphology and shape is the only option. These modifications include geometrical patterning of silicon membrane into “wavy” shaped ribbons [10], [79] and synthesising nanowire structures through bottom-up and top-down approaches [72]. Compared with conventional silicon-based semiconducting



nanostructured materials, carbon-based nanostructures such as graphene, CNTs etc. exhibit higher carrier mobility [76]. However, the wafer-level fabrication and processing of graphene-based devices are still challenging and it has a limited capability to withstand strain [80]. Semiconducting SWCNTs, on the other hand, attract researchers due to their excellent mechanical bendability. However, given the fact that the SWCNT network is often consisting of both semiconducting and metallic SWCNTs, it is challenging to obtain the device with high  $I_{on}/I_{off}$  ratio and mobility [77].

Conjugated polymers have drawn attention to be the candidates as stretchable semiconducting materials, due to their intrinsic semiconducting property, low weight and high flexibility. Furthermore, they can be processed in solution for large-scale manufacture, including ink-jet printing and roll-to-roll printing for printing in large scale [81]. For applications in stretchable electronics, semi-conducting and mechanical softness properties of conjugated polymers can be optimised through various methods. For example, pristine P3HT has Young's modulus of 0.92 GPa with limited tolerate strain [82]. However, if P3HT is synthesised with copolymer polyethylene, and transferred into P3HT-block-polyethylene copolymer (P3HT-PE), the modified polymer can be stretched up to 660% with a 240 MPa Young's modulus. The mobility can reach  $2 \times 10^{-2} \text{ cm}^2 \text{V}^{-1} \text{ s}^{-1}$  with device ON-OFF ratio of  $I_{on}/I_{off} \sim 10^5$  [83]. Another approach is based on the nanoconfinement process with different polymers [36], [74]. It was reported that the combination between conjugated polymer DPPT-TT and elastomer SEBS exhibits the nanoconfinement effect in crystallinity reduction, which significantly helps to reduce the crack propagation. Nanoconfinement effect is not only suppressing resultant polymer's crystallisation but also increasing the chain dynamics, which leads to producing more elasticity. Thus, it allows the semiconducting polymers to become soft enough for 1000 cycles up to 100% strain and the stretchability of 600%. In addition, the resultant polymer exhibits a mobility of  $1.37 \text{ cm}^2 \text{v}^{-1} \text{ s}^{-1}$ . A successful demonstration of the logic circuit based on this OFET has realised to perform a stretchable amplifier [36]. However, the challenges of such polymer-based electronic materials are their limited mobility and limited life time due to their sensitivity to become damaged by the organic solvent and ultraviolet light. Proper encapsulation is required for this type of material.

### 2.2.2. Conductors

A stretchable conductor should possess properties of softness (with a low Young's modulus  $E$ ), ability to retain the original shape after deformation (Poisson's ratio reaching

0.5), high electrical conductivity and ideally with negligible variation in electrical conductivity. Such materials for interconnects are discussed in detail in the following sections. A few examples of this type of stretchable conductors include elastic conductors based on Single-Walled Carbon Nanotubes (SWNT)-PDMS composite films [84]–[87]. In these interconnects, the nanotubes fillers conduct electricity and the rubber provides the stretchable matrix. These elastic conductors allow uniaxial and biaxial stretching of 70–100%—without mechanical damage or electrical loss. Microfluidics channels with conductive liquid/gel is another popular alternative that has been developed in recent years to obtain stretchable conductors [88]. These approaches are not yet at a stage where they can be employed in sensors' integration. Nonetheless, recent advances in material engineering show promise in this area.

### **i. Organic conductive polymer**

The organic conductive polymers have emerged as the popular candidate for filler materials, owing to their moderate electrical conductivity and mechanical softness [89]. Some of the widely used organic conductors include Polyaniline (PANI) [39] and Poly(3,4-ethylenedioxythiophene): poly(4-styrenesulfonate) (PEDOT:PSS) [40]. They are electrically conductive ( $\sim 100$  S/cm) in addition to having mechanical softness of up to 10% stretching without any cracks in the film [40]. Furthermore, PEDOT, as an efficient hole collector and transparent conductor, is popular to be applied in photovoltaic electronics and optoelectronic applications [90], [91]. The electrical conductivity of these conductive polymers can be tuned through different methods. In the case of PEDOT:PSS, the highly conductive PEDOT grains are surrounded by excess weakly ionic- conducting PSS. Although the PSS ions help PEDOT to be easily dispersed in water for a homogenous deposition, it separates PEDOT from establishing a conductive path [92]. A secondary doping can improve the electrical conductivity of the resulting PEDOT:PSS film [90], [93] and the maximum conductivity can reach to the order of 1000 S/cm, which is still low in comparison with metals. So far, the PEDOT:PSS film has been demonstrated to replace ITO sheet successfully in solar cells application [94].

### **ii. Metal liquid**

Eutectic metal liquids have been used for stretchable interconnects due to their high conductivity and low resistance variation when subjected to deformability [95]. It is an alloy that is composed of low melting point metals such as Mercury (Hg), Tin (Sn), Indium (In) and Gallium (Ga). Aiming at low vapour pressure and low toxicity, researchers tend to use

more of liquid metal alloys made of Galinstan (Ga 68.5 %, In 21.5 %, and Sn 10 %) and EGaIn (eutectic gallium-indium alloy, Ga 75.5 % and In 24.5 %) [19]. These metals can either be filled into microfluidic channels in a stretchable substrate [19], [96] or be directly 3D printed into a conductive pathway [95], [97]. The fluidic property of eutectic metal liquid allows the metal interconnect to deform without losing the electrical continuity. However, these low melting metals are inclined to become oxidised at room temperature. The oxide skin of metal liquid further prohibits the wetting of contact pads and increases the contact resistance, which brings the challenge for sensors' integration [98].

### **iii. Composite**

The conductive composite benefits from the high electrical conductivity of fillers dispersed in elastic polymer matrix and the softness nature of elastic polymer matrix. The synthesis of such composite with the appropriate ratio of fillers is critical in terms of optimising the composite's performance. The synthesis process requires three essential components: the conductive filler, the binder (polymer matrix) and the solvent [41]. To make sure that the fillers are homogeneously dispersed in the matrix, the appropriate solvent is selected to de-bundle the fillers with adjusted physical agitation. Mechanical milling and sonication are two common techniques for the physical agitation. The prior method utilises external mechanical stress to activate physical and chemical transformation in solid materials [99][100]. For instance, the ball milling method, which has been extensively used for composite synthesis shows its advantage on high efficiency and controllable synthesising conditions (i.e. temperature, rotating speed, pressure). In this method, powders are processed under mechanical stress from the collisions between milling tools and the material surface. However, during the composite synthesising process, not only will the chemical activation happen, but also the mechanical degradation can be found simultaneously. This mechanical degradation can fail the resulting composite, especially for polymeric composite [100]. The process required power from another physical agitation technique, sonication, can be much lower. The sonication power and duration can be tuned to transduce the energy for dispersing the fillers homogeneously without breaking them [101]. In general, the electrical behaviour of the final composite will be enhanced if the loading ratio of fillers is increased. However, the elastic modulus of the composite will also increase and therefore a balance is needed between the elastic modulus and electrical conductivity. The following sub-sections describe the theory governing this trade-off and further discussion on various composites based on various conductive fillers and the polymer matrix.

*a. Percolation and tunnelling theory*

The conductivity of composites varies as a result of variations in filler concentration [34]. The composite's conductivity is governed by the percolation theory, which is represented by **Equation 2.1** [102], [103]:

$$\sigma \approx \sigma_0(p - p_c)^t, \text{ for } p > p_c \quad (2.1)$$

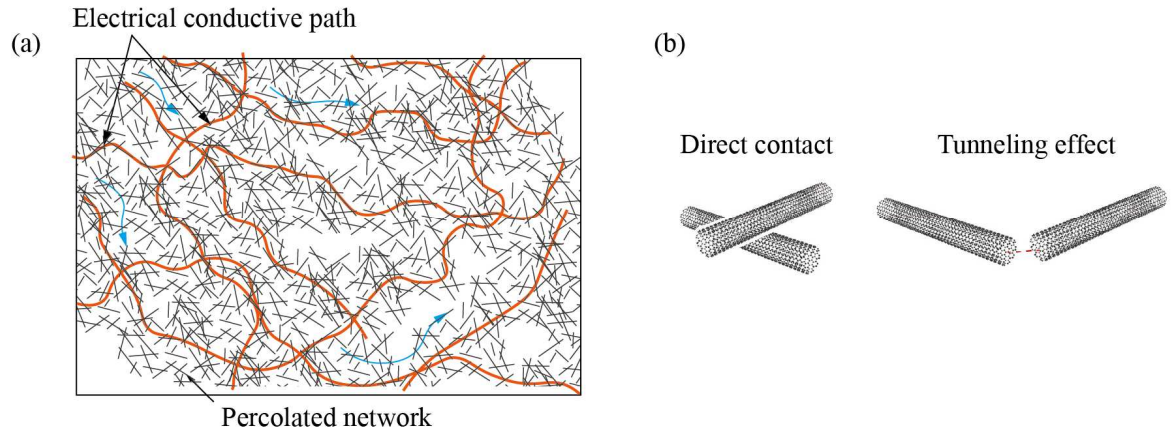


Figure 2.3: Schematic diagram of theory of (a) percolated network and (b) tunnelling effect between adjacent nanowires [238].

Where  $\sigma$  is the bulk conductivity of the composite,  $\sigma_0$  is the conductivity of the filler,  $p$  is the weight percentage of the filler and  $t$  is the critical exponent. The critical percentage  $p_c$  of the filler is defined as the percolation threshold. This critical fraction is obtained when a continuous electrical path is established within the polymer matrix, as illustrated in **Figure 2.3** [103]. The value of the percolation threshold is contributed by several parameters and these include the dimension of filler, the morphology of the filler, and synthesis method of the composite. Many numerical simulation and mathematical modelling studies have been carried out to investigate the effect of the filler's dimension on the percolation threshold [104]–[106]. For instance, in Balberg et al.'s theory, a composite system can be modelled as a lattice-like system and its percolation threshold is strongly dependent on the density and dimension of the fillers [107]. Some researchers have studied the composite system based on Monte Carlo Simulation. In that regard, the percolated network is dealt with as a statistic problem. Both studies suggest that the percolated threshold is proportional to the reciprocal of particle's aspect ratio [108] and is mathematically expressed in **Equation 2.2**, where  $L$  and  $D$  are the length and diameter of filler respectively.

$$p_c \propto \frac{1}{r}, r = \frac{L}{D} \quad (2.2)$$

The experimental results obtained from variously reported composites and plotted in **Figure 2.4(b)** and **(c)** are in line with the above theoretical relationship between the percolation threshold and the filler's aspect ratio. Extending further this relationship, **Figure 2.4(a)** also concludes the correlation between the maximum achieved conductivity and the aspect ratio of fillers among various composites. The global conductivity of the percolated network within the polymer matrix depends on the conductivity of the filler, the contact resistance between overlapped fillers and conductivity of electron tunnelling effect through the nearby fillers [109]. The distance of the tunnelling effect  $d_{tunnel}$  can be estimated as:

$$d_{tunnel} = \hbar / \sqrt{8m_e \Delta E} \quad (2.3)$$

Where,  $\hbar$  is the Planck's constant,  $m_e$  is the mass of electron and  $\Delta E$  is the difference in work function between filler and polymer matrix. However, this tunnelling effect can be ignored if the wrapped polymer between adjacent nanowires is thicker than a cutoff distance  $d_{cutoff}$ . [109].

#### *b. Elastic modulus of composite materials*

The studies estimating the elastic modulus of composite materials have a long history and they can date back to the 1970s [110]. The general form for the elastic modulus of the composite is defined as [111]:

$$\frac{M}{M_1} = \frac{1+AB\phi}{1-B\phi} \text{ where } B = \frac{M_2/M_1 - 1}{M_2/M_1 + A} \quad (2.4)$$

Where  $M$  represents the elastic modulus of composite and  $M_1$  and  $M_2$  are the modulus of the polymer matrix and filler respectively.  $\phi$  is the volume fraction of fillers and  $A$  is a critical parameter defined by the geometry of filler and the Poisson's ratio of the polymer matrix. This general equation skips some factors such as the sediments and aggregations of fillers, but it gives a fair estimation of the mechanical property of the resulting composite. Observed in **Figure 2.4(c)**, the trend in stretchability with respect to the filler's aspect ratio indicates a reciprocal relationship. With the same polymer and filler materials, lesser fillers lead to a softer and more elastic composite.

*c.. Carbon-based nanocomposite*

Carbon particles are widely used as conductive fillers due to the availability, high electrical conductivity and low cost. Many reported studies on carbon-based composite for applications in stretchable interconnects are listed in **Table 2.2**. It can be noted that graphite is one of the most widely used carbon fillers for stretchable and conformable electrodes. The filler size is above 10  $\mu\text{m}$ . Compared to CNTs, EG and GNPs, they are much larger. However, the bulk size of graphite does not provide lower percolation ratio within the composite. Hence, in order to achieve the desired level of electrical conductivity a large number of fillers are used, which leads to degradation of stretchability in graphite-based composites [112]. On the other hand, owing to the high aspect ratio of CNTs, CNT-based nanocomposite has a much lower percolation threshold [113]. However, due to the strong

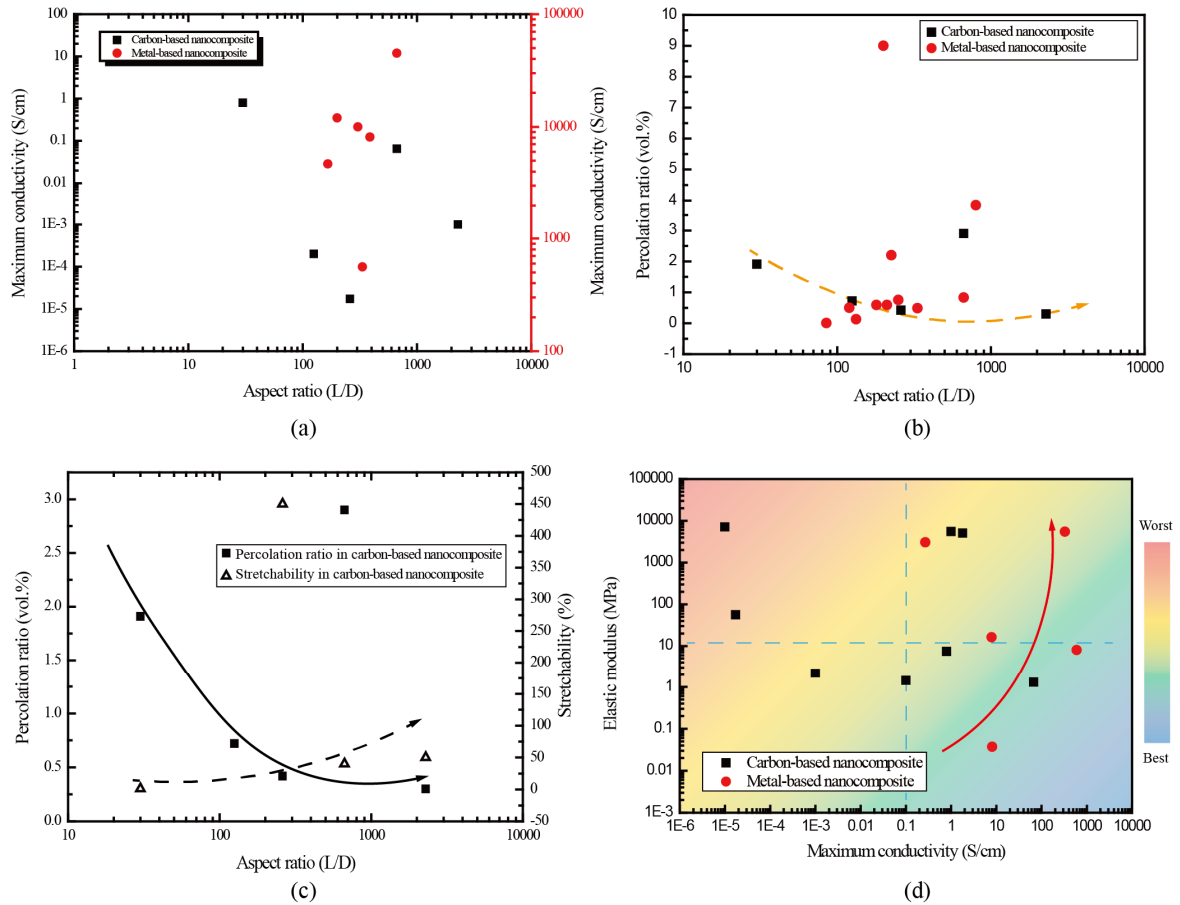


Figure 2.4: Plot of reported data points collected from Table 2.2 and Table 2.3. (a) Correlation between the maximum conductivity and aspect ratio of fillers from various nanocomposites, (b) Correlation between percolation ratio and aspect ratio among various nanocomposites, (c) The trend of percolation ratio and stretchability with respect to aspect ratio for carbon-based nanocomposite, (d) The mapping of data points with the elastic modulus against the maximum conductivity [238].

Van-der-Waal forces among carbon fillers, they tend to bundle and entangle together, which leads to an inhomogeneous conductivity. By evaluating the maximum conductivity of variously reported nanocomposites, it is observed that the group of Graphene Nanoplatelets (GNPs) nanocomposites exhibits a superior conductivity with low percolation ratio. This is because graphene has a large surface area of  $2630 \text{ m}^2\text{g}^{-1}$  and a high electrical conductivity of  $7200 \text{ S}\cdot\text{m}^{-1}$  [114]. In addition, the composite-based interconnects that was carried out in this thesis is also compared in **Table 2.2**. With similar size of graphite fillers, the achieved composite exhibits a much higher stretchability.

Table 2.2: Comparison of various nanocomposites based on carbon fillers with respect to properties such as filler's size, percolation ratio, maximum conductivity, and mechanical elasticity.

Material (Filler-polymer matrix)	Filler size	Aspect ratio (L/D)	Percolati on ratio	Maximum conductivit y	Elastic Modulus	Stretch ability	Ref.
Graphite-PDMS	25.4 $\mu\text{m}$	-	11.1 vol.%	1.8 S/cm	5.1 GPa	0.71%	[112]
Graphite-PDMS	10 $\mu\text{m}$	-	12 vol.%	$2\times 10^{-6}$ S/cm	-	-	[115]
Graphite-Epoxy	D: 10 $\mu\text{m}$ , t: 0.1 $\mu\text{m}$	-	1.3 vol.%	1 S/cm	5.56 GPa	-	[116]
Graphite-PU <sup>a</sup>	D: 10 $\mu\text{m}$ , t: 0.1 $\mu\text{m}$	-	1.7 vol.%	$1\times 10^{-5}$ S/cm	7.14 GPa	-	[116]
Graphite-Epoxy	4-44 $\mu\text{m}$	-	20 vol.%	$3.3\times 10^{-2}$ S/cm	-	-	[117]
Graphite-Phenolic Resin	< 1 $\mu\text{m}$	-	15 vol.%	66.7 S/cm	1.3 MPa	-	[118]
Graphite-PP <sup>b</sup>	21.3 $\mu\text{m}$	-	-	20.16 S/cm	-	-	[119]
Graphite-PVDF <sup>c</sup>	21.3 $\mu\text{m}$	-	-	0.56 S/cm	-	-	[119]
Graphite-LDPE <sup>d</sup>	2.1-82.6 $\mu\text{m}$	-	2.1 $\mu\text{m}\rightarrow$ 13.5 vol.%, 82.6 $\mu\text{m}\rightarrow$ 25.5 vol.%	1 S/cm	-	-	[120]
<sup>e</sup> EG-PANI	L: 400 nm, t: 10-40 nm	-	0.91 vol.%	35 S/cm	-	-	[121]
<sup>f</sup> GNP- PE <sup>g</sup>	L: 39-115 nm t: 3.6-7.1 nm	-	0.51, 1.2, 2.4 vol.%	-	-	-	[122]
<sup>h</sup> G-ODA-PDMS	t: 2.7 nm	-	0.63 vol.%	$2\times 10^{-6}$ S/cm	-	-	[114]
Graphite-PS <sup>i</sup>	D: 6.5 $\mu\text{m}$ ,	-	3.5 vol.%	$1\times 10^{-5}$ S/cm	-	-	[123]

	t: 100-300 nm							
<sup>j</sup> MWCNT-PDMS	L: 1-25 $\mu\text{m}$	-	2.1 vol.%	0.1 S/cm	1.43 MPa	45%	[113]	
	L: 5-15 $\mu\text{m}$							
MWCNT-PDMS	D: 60-100 nm	125	0.72 vol.%	$2 \times 10^{-4}$ S/cm	-	-	[124]	
	L: 30-50 $\mu\text{m}$							
MWCNT-PDMS	D: 15-20 nm	2285	0.3 vol.%	$1 \times 10^{-3}$ S/cm	2.18 MPa	50%	[125]	
	L: 10-30 $\mu\text{m}$							
MWCNT-PDMS	D: 20-40 nm	666	2.9 vol.%	$6.5 \times 10^{-2}$ S/cm	-	40%	[126]	
	L: 1-2 $\mu\text{m}$							
MWCNT-PDMS	D: 40-60 nm	30	1.91 vol.%	0.8 S/cm	7.38 MPa	1.2%	[127]	
	L: 30 $\mu\text{m}$							
<sup>k</sup> CNF-PU	D: 80-150 nm	260	0.42 vol.%	$1.72 \times 10^{-5}$ S/cm	56 MPa	450%	[128]	
Graphite-PEDOT:PSS	45 $\mu\text{m}$	-	~90 wt.%	0.535 $\Omega/\square$	-	50-80%	(Sect-ion 5.4)	

<sup>a</sup>PU: Polyurethanes, <sup>b</sup>PP: Polypropylene, <sup>c</sup>PVDF: Poly(vinylidene fluoride), <sup>d</sup>LDPE: Low density polyethylene, <sup>e</sup>EG: Exfoliated graphite, <sup>f</sup>GNP: Graphene Nanoplatelets, <sup>g</sup>PE: Polyethylene, <sup>h</sup>G-ODA: Alkyl-functionalized graphene, <sup>i</sup>PS: Polyester, <sup>j</sup>MWCNT: Multi-walled carbon nanotube, <sup>k</sup>CNF: Carbon Nanofiber.

#### d. Metal-based composite

Metal-based composites generally comprise metallic particles or nanowires (NWs) as filler materials. They are popular owing to their higher conductivity compared to carbon-based fillers. Silver flakes are widely used in commercially available conductive inks. Recently, the stretchable and conductive silver-based ink has been commercialised [42]. The reported silver based composites exhibit a high conductivity, with a range of  $10^3$ - $10^4$  S/cm, as shown in **Table 2.3**. In the process, the resulting composites tend to be softer, especially compared with graphite-based composites. The high aspect ratio of AgNWs can be the reason, due to its lower percolation threshold in the polymer matrix. However, the maximum conductivity of AgNWs nanocomposite does not indicate a strong correlation between the aspect ratio of NWs, based on the collected data from the reported literature (**Table 2.3**). In general, the percolation ratio of AgNWs nanocomposites is lower than that carbon-based nanocomposites. With a filler ratio of 0.005 vol.%, their conductivity can reach  $2.3 \times 10^{-2}$  S/cm [129]. On average, the stretchability of AgNW nanocomposites can reach 115%, which makes AgNW nanocomposites a good candidate for stretchable interconnects. Some other



metallic NW-based composites, such as CuNWs and AuNWs, show similar performance to that of AgNWs. Although metal-NWs composites have the advantages of high conductivity with a lower elastic modulus that are suitable for stretchable interconnects application, there are challenges with respect to their fabrication and chemical stability. For example, due to the fact that metallic NWs are usually manufactured in a solution-based method, the insulating ligands in the solvent should be removed to obtain a low contact resistance between adjacent NWs. Usually, a post-treatment process, such as thermal annealing, is introduced for this purpose and this poses a challenge for the devices on soft polymeric substrates which are sensitive to temperature variations. In the meanwhile, the metallic nanowires tend to oxidised easily, which requires a post-treatment to remove the oxidation layer. Such treatment often involves the acid or alkali solutions. To avoid post-treatment on metallic NWs, the idea of introducing conductive polymer PEDOT:PSS as the nano-solder junctions among wires can dramatically improve the performance of interconnects [130]. Other solutions, such as building up a hybrid system with AgNWs and other nano-fillers (CNTs [131] and Graphene [132]), also show highly stretchable and conductive performance.

Table 2.3: Comparison among various nanocomposites based on metal fillers in terms of properties such as filler's geometry, percolation ratio, maximum conductivity and mechanical elasticity.

Material (filler-polymer matrix)	Filler size	Aspect ratio (L/D)	Percolation ratio	Maximum conductivity	Elastic Modulus	Stretch ability	Ref
Ag flakes-PU	2-3 $\mu\text{m}$	-	56 vol. %	$3.6 \times 10^3 \text{ S/cm}$	-	600%	[133]
AgNW-poly(acrylate)	L: 5-15 $\mu\text{m}$ D: 60 nm	83-250	-	7.84 S/cm	16.25 MPa	50%	[134]
Ag Powder-PDMS	2-3.5 $\mu\text{m}$	-	12.6 vol. %	$6 \times 10^2 \text{ S/cm}$	8 MPa	150%	[135]
AgNW-PUA <sup>a</sup>	L: 15-25 $\mu\text{m}$ D: 25-35 nm	666	0.83 vol. %	$4.5 \times 10^4 \text{ S/cm}$	-	70%	[41]
AgNW-PDMS	L: 20-50 $\mu\text{m}$ D: 115 nm	304	-	$9.97 \times 10^3 \text{ S/cm}$	-	100%	[136]
AgNW-PDMS	L: 10-60 $\mu\text{m}$ D: 90 nm	388	-	$8.13 \times 10^3 \text{ S/cm}$	-	15%	[137]
Ag flakes-PU	-	-	-	$4.31 \times 10^4 \text{ S/cm}$	-	74%	[42]
AgNW-PDMS	L: 10 $\mu\text{m}$ D: 60 nm	166	-	$4.69 \times 10^3 \text{ S/cm}$	-	150%	[138]

<b>AgNW-PDMS</b>	L: 10-60 μm D: 90 nm	388	-	8.13×10 <sup>3</sup> S/cm	-	80%	[139]
<b>AgNW-PDMS</b>	L: 80 μm D: 100 nm	800	3.85 vol.%	20 S/cm	-	35%	[140]
<b>AgNW- poly(TBA-co- AA)<sup>b</sup></b>	L: 20 μm D: 60 nm	333	-	5.6×10 <sup>2</sup> S/cm	-	160%	[141]
<b>AgNW-PLA<sup>c</sup></b>	L: 8 μm D: 60 nm	133	0.13 vol.%	0.27 S/cm	3048 MPa	3%	[142]
<b>AgNW-MC<sup>d</sup></b>	-	-	0.29 vol.%	3.3×10 <sup>2</sup> S/cm	5519.9 MPa	-	[143]
<b>AgNW- PEDOT:PSS</b>	L: 10-30 μm D: 90 nm	222	2.5% Areal fraction	10 <sup>4</sup> S/cm	-	-	[144]
<b>AgNW- PEDOT:PSS</b>	L: 50-100 μm D: 10 nm L: 10-100 μm	7500	-	0.73×10 <sup>3</sup> S/cm	-	120%	[145]
<b>AgNW-PEKK<sup>e</sup></b>	D: 120- 400 nm	211	0.59 vol.%	1 S/cm	-	-	[146]
<b>AgNW-PC<sup>f</sup></b>	L: 10 μm D: 117 nm	85	0.005 vol.%	2.3×10 <sup>-2</sup> S/cm	-	-	[129]
<b>AgNW-PA11<sup>g</sup></b>	L: 30-60 μm D: 200- 300 nm L: 10-60 μm	180	0.59 vol.%	2.7 S/cm	-	-	[147]
<b>AgNW-PS</b>	D: 70-140 nm	333	0.489 vol.%	10 S/cm	-	-	[148]
<b>AgNW-SBS<sup>h</sup></b>	L: 30 μm D: 150 nm	200	9 vol.%	1.2×10 <sup>4</sup> S/cm	-	100%	[149]
<b>CuNW-PVA<sup>i</sup>- PDMS</b>	L: 20 μm D: 60 nm	333	-	8.1 S/cm	37.5 kPa	60%	[150]
<b>CuNW- GFRHybrimer<sup>j</sup></b>	L: 35 μm D: 50 nm	700	-	4.8 S/cm	-	-	[151]
<b>CuNW-PS</b>	L: 3 μm D: 25 nm	120	0.25- 0.75 vol.%	10 <sup>-6</sup> S/cm	-	-	[152]
<b>CuZr-PDMS</b>	-	-	-	1.32×10 <sup>4</sup> S/cm	-	70%	[153]
<b>NiNW-P(VDF- TrFE)<sup>k</sup></b>	L: 50 μm D: 200 nm	250	0.75 vol.%	1 S/cm	-	-	[154]
<b>AuNW-P(VDF- TrFE)</b>	L: 45 μm D: 200 nm	225	2.2 vol.%	1 S/cm	-	-	[155]

<sup>a</sup>PUA: Polyurethane acrylate, <sup>b</sup>Poly(TBA-co-AA): Poly(tert-butylacrylate-co-acrylic acid), <sup>c</sup>PLA: Polylactide, <sup>d</sup>MC: Methylcellulose, <sup>e</sup>PEKK: Poly(ether ketone ketone), <sup>f</sup>PC: Polycarbonate, <sup>g</sup>PA11: Polyamide 11, <sup>h</sup>SBS: Styrene butadiene styrene, <sup>i</sup>PVA: Poly(vinyl alcohol), <sup>j</sup>GFRHybrimer: Glass-fabric reinforced plastic film, <sup>k</sup>P(VDF-TrFE): Poly(vinylidene difluoride)- trifluoroethylene.

### 2.2.3. Geometry

Aside from improving the intrinsic properties of conductors, geometry selection also plays an important role. **Figure 2.5** summarises the reported work on stretchable interconnects with different geometries, obtained the ultimate strain (which can also be referred to stretchability) and the structure size fabricated through different patterning technologies.

The engineered geometries such as helical wires have been widely used for stretchable interconnects for a long time. The idea of a helical conductive wire is straightforward, which resembles the structure of a spring or wire connecting a telephone receiver to its base in the recent past [46], [47]. As illustrated in **Figure 2.5**, the helical-shaped wires are capable of storing a significant length in wire depending on its spool radius and pitch distance. While the wire is pulled from one side, the radius of the helix is reduced and the pitch is enlarged. This spring tension leads to helical wire under torsion and bending, but the wire does not need to be stretchable. Based on the principle of helical wires, twisted wires, knitted network, and hybrid geometries were developed. For example, the expandable spiral electrodes, which is obtained by winding the copper wires around an elastic nylon line, have been used to obtain large-area tactile skin [158]. Conductive twisted threads based clothing has been used in stretchable wearable electronics [159], [160]. Likewise, the stretchable fabrics with

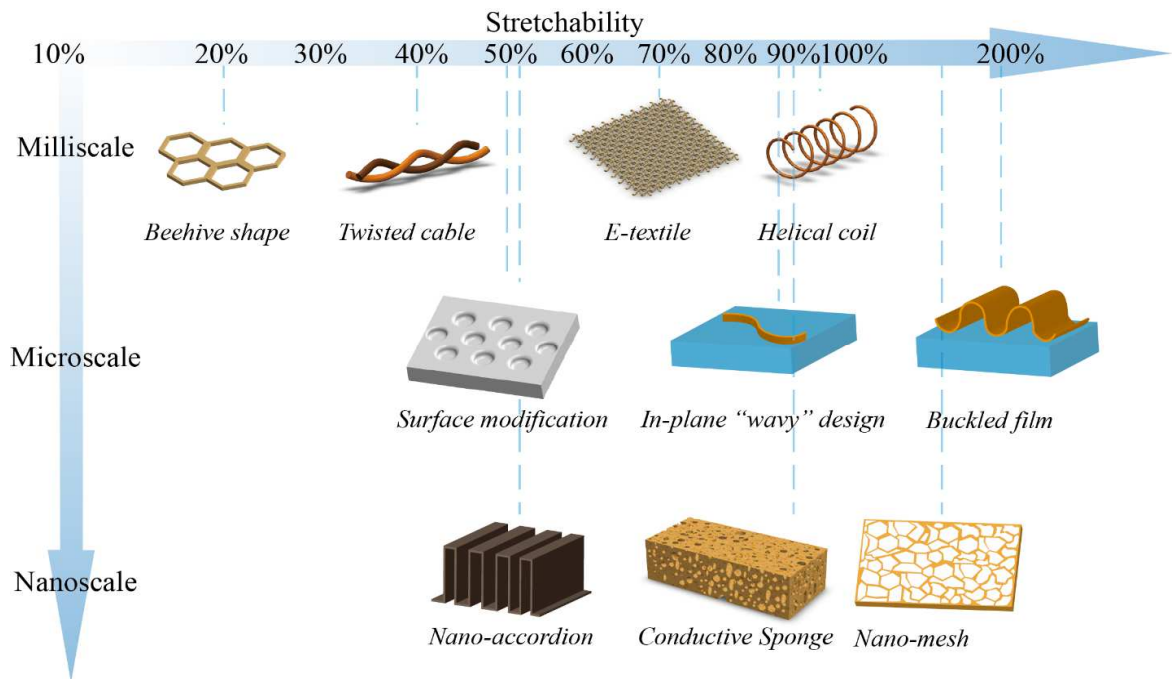


Figure 2.5: Various engineered geometries of stretchable interconnects which are sorted according to their maximum elongation ratio (stretchability) with respect to the scale of structure size achieved by different patterning technologies [238].

knitted tactile sensing materials have been reported for stretchable tactile sensing [32], [161]. Such a stretchable fabric system often requires a core to guide the pathway of helical wire's movement. It can be chosen as an elastic thread and the conductive wire is wound around the core. The winding is under a precise control in pitch and winding speed to build the helical shape. As explained previously, the wire can either be rigid commercial copper wires [157] or elastic polymeric wires coated with a highly conductive material (e.g. AgNWs [156]). Depending on the winding pitch, helical diameter, and wiring material, the elongation ratio (stretchability) of such designs can reach up to 100% with an increased resistance by 70% [156]. However, the interconnects with helical and twisted geometries are commonly restricted in the millimetre scale dimensions and narrowed scalability.

Another engineering technique for obtaining stretchable interconnects involves realising interconnecting layers in “wavy” or serpentine shapes [162]–[165]. Compared to the limited scalability possible in the helical coil and twisted threads, the geometry of in-plane “wavy” design can be easily scaled down into microscale by microfabrication technology as compared in **Figure 2.5**. Serpentine shape geometry can be regarded as an extended version of helical wires. It stores the length of interconnect into a planar direction. Similarly, it does not require the material of interconnects to be stretchable. Bending and distorting at the curved section in interconnects can lead to a stretching movement in overall interconnect geometry. In order to study the working mechanism of serpentine shaped interconnects and further optimise the serpentine geometry design, many mechanical and mathematical models have been developed. One analytical model is based on the space-fill principle [166]. It indicates that the longer interconnects that can be patterned within a certain space; the higher degree of stretchability can be achieved. In this model, stretchable interconnects are not considered to bond to substrate and the interaction between interconnects and substrate is neglected. The boundary condition at the two ends of interconnects is modelled as clamped terminals. The model can give an estimation of the trend in stretchability when the number of turns in serpentine-shaped interconnects increases. However, the simulation condition may not be suitable for all situations. To be closer to the real situation in experiments, another model which includes plastic deformation in interconnects was proposed to analyse the serpentine-shaped interconnects [167]. In this model, the serpentine-shaped interconnect is modelled as an Euler-Bernoulli beam and it is clamped from both ends. Through considering the stress-strain relationship of interconnect in plastic region, the total stretchability estimation of interconnects is more accurate. A simplified model on serpentine geometry was also proposed by H. Hocheng *et.al.* [168]. There are four parameters defined as illustrated in **Figure 2.6(a)** in coplanar serpentine routing,  $R$  (radius of arc),  $\theta$  (arc angle),  $L$

(straight section of routing) and  $W$  (width of routing). The geometric function can be described by **Equation 2.5** with two boundary conditions,  $L=0$  and  $L \neq 0$ . The equation was conducted under the restriction of avoiding overlapping adjacent serpentine curves.

$$R \cos\left(\theta - \frac{\pi}{2}\right) - \frac{L}{2} \cos(\pi - \theta) \geq \frac{1}{2}\left(R + \frac{W}{2}\right) \quad (2.5)$$

$$\text{Boundary condition 1 (if } L=0\text{): } \theta \leq \pi - \arcsin\left(\frac{1}{2} + \frac{1}{4} \frac{W}{R}\right) \quad (2.5a)$$

$$\text{Boundary condition 2 (if } L \neq 0\text{): } \frac{L}{R} \leq 2 \sec \theta \left(\frac{1}{2} + \frac{1}{4} \frac{W}{R} - \sin \theta\right) \quad (2.5b)$$

The theoretical strain of a fully stretched coplanar serpentine routing is expressed in **Equation 2.6**. The relationship between the ratio of the straight section length and radius of arc ( $L/R$ ), arc angle and the theoretical strain is concluded in **Figure 2.6(b)**. The arc angle has a limit of  $150^\circ$  when boundary condition 1 (**Equation 2.5b**) is met in **Equation 2.5** and  $W$  is zero. Here to note, this model does not include the conditions of material's failure and the failure at the interface between the substrate and the conductor.

$$\varepsilon_{\text{coplanar type}}\left(\theta, \frac{L}{R}\right) = \frac{2\theta + \frac{L}{R}}{2 \sin \theta + \frac{L}{R} \cos \theta} - 1 \quad (2.6)$$

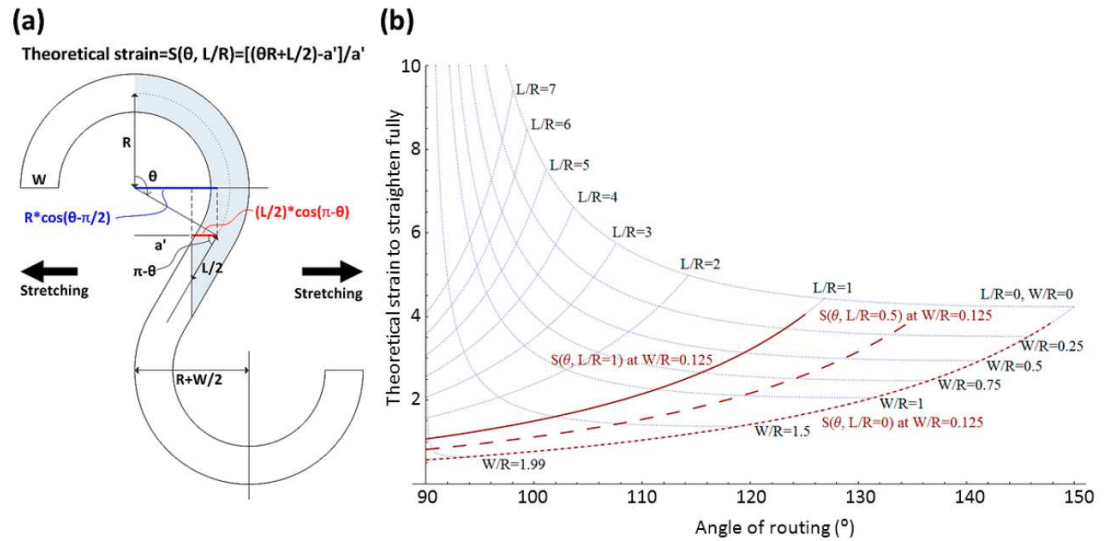


Figure 2.6: (a) Schematic representation of the geometric variation of serpentine-shaped conductor under stretching and (b) the theoretical strain after fully straightening of serpentine routing designs [168].

In order to achieve a more realistic estimation of how the shape of serpentine routing helps to reduce the maximum stress and strain to the conductor, analytic models and numerical simulations, such as Finite Element Method (FEM), are performed. The optimised serpentine interconnects can be applied up to 90% strain with a negligible influence on electrical response [165]. With the serpentine-shaped design, the concentrated plastic strains are found at the crest and trough area in conductor routings. The out-of-the-plane “wavy” structure or the buckled film can either be deposited along with buckled substrate [37] or partial-free standing on the substrate [169], [170]. The stretchability of wavy structures on buckled substrates mainly relies on the degree of pre-straining of the substrate, which depends on the substrate’s softness. On the other hand, the interconnects that are partial-free standing on the substrate have a higher degree of stretchability, which benefits from the releasing from interfacial stress and strain between interconnects and substrate. Both in-planar and out-of-planar serpentine shaped interconnects can be connected by rigid sensor islands into a network. Such network increases the sensing resolution by defining each sensor island as a pixel/node. The connected sensors are able to conformably attach to an unconventional surface such as elbows. A popular method to realise such interconnect network is to deposit conductive materials on a prestrained elastic substrate and release or transfer print pre-defined interconnect structures to the elastic substrate [79].

Engineering the topography of the substrate can also enhance the stretchability of interconnects. One such example is incorporating mini-valleys on the surface of the soft substrate and followed by the conductive materials’ coating. The valley-shaped topography helps stress/strain re-distributes over the surface under stretching, which leads to a stable electrical performance over a cyclic stretching [171]. Other than implementing mini-valleys on the surface of the substrate, structures such as the honeycomb lattice architecture or sponge shape are designed for stretchable interconnects. The introduced vias or air pores to the substrate give the structure space in deformation, resulting in nearly 90% stretchability (**Figure 2.5**). The conductive sponge can either be achieved by electrodeless-plating on commercial available PU sponge [172] or drop-casting carbon nanotube on the sponge [173]. Recent research on multilayered graphene sponge has also attracted great interest [174]. However, the idea of using a conductive sponge as stretchable interconnects has several limitations, including the trade-off between pore size in the sponge and the stretchability of the sponge. Finer pore size in the sponge is favourable in order to scale the overall sponge size down, but it may compromise the stretchability. Further, there are challenges related to the sensors’ integration and assembly of such structures, as the pores in the structure do not allow seamless integration as in conventional electronics. Some technologies can realise a

very fine pore structure of interconnects. For example, the nano-mesh structure fabricated by grain boundary lithography. This nanoscale structure can withstand the strain up to 160%. However, after a 1000 cycles' test, the structure fails as its resistance increases significantly [175]. Another example is the nano-accordion structure which is made of atomic layer deposition (ALD) deposited Al-doped ZnO. This structure can be elongated up to around 53%, but in the meantime with unstable electrical performance [176].

## 2.4. Fabrication process

The fabrication of stretchable interconnects and sensors' integration on stretchable and conformable substrates includes the material process, patterning, sensors' integration, and their packaging. The material process is vital for unconventional materials to optimise their electrical performance. Unconventional materials, as reviewed in previous section, often refers to an organic material and nanocomposites, which involves 1D/2D materials. By modifying the material's chemical structure, hydrophobicity, morphology, and rheology, an optimised electrical/mechanical property of the resultant material can be obtained. This material process also benefits subsequent steps such as coating and patterning which are closely linked to reproducibility and scalability. Various technologies have been developed to pattern conventional/unconventional materials. These include microfabrication method, moulding, roll-to-roll printing, micro-contact printing, transfer printing, inkjet printing, screen printing, and spray coating. Based on the processed material, the required resolution and material of the substrate, the different patterning method can be chosen.

### 2.4.1. Microfabrication

Microfabrication process is a well-developed industrial-level process. It comprises several steps including aqueous cleaning, spin-coating, baking, ion-implantation, deposition (i.e. chemical vapour deposition, E-beam evaporator), photolithography, etching (dry etch/wet etch), lift off. The major steps that are often used for stretchable interconnect fabrication are spin coating, photolithography, and etching, which are illustrated in **Figure 2.7(a)**. By using this technology, researchers have realised the silicon-based stretchable ribbons, metal interconnects and metal-polyimide based stretchable interconnects [177], [178]. The advantage of such a technology is its scalability and compatibility with standard silicon devices fabrication. However, the restriction of this technology can be found in the limited choice of material, available only to planar substrates and unavoidable to solvent, acid and

base solutions. Due to these restrictions, many researchers combine this microfabrication method with other printing technology to develop the stretchable electronic system.

### 2.4.2. Contact printing

Contact printing is a printing technique to describe the process when the donor substrate and foreign receiver substrate come in touch with each other. One of the major applications of contact printing is to transfer and align the nano-structures (e.g. nanowires, nanoribbons etc.) from a donor substrate to various receiver substrate (e.g. polymeric substrate). This transfer process, as shown in **Figure 2.7(b)** can avoid incompatible issues of polymeric substrate to some fabrication process. For example, the silicon nanowires which are fabricated through either bottom-up or top-down methods have critical steps such as ion-implantation, oxidation, patterning, and etching. During these processes, high temperature ( $\sim 1000^{\circ}\text{C}$ ), strong acid (HF) and organic solvent conditions are commonly involved. In this case, the nanowires are often fabricated on a silicon substrate and then transfer printed on the desired flexible substrate/devices [179]. The assistive transfer medium can be a PDMS block or tape. The contact printing can also assist to highly align the nanowires in one direction to the receiver substrate [180], [181].

Another type of contact printing involves the pre-fabricated stamp contacting with conductive ink first and this is followed by contacting with the target substrate under specific pressure, as described in **Figure 2.7(c)**. It is also called stamp printing. The resolution of printed film highly depends on the resolution of the pre-fabricated stamp. Various fabrication technologies have been reported to realise the stamp including photolithography [182], E-beam lithography [183], micromachining [184] and nano-imprinting [185]. The resolution of final printed structure also depends on the contact pressure, the viscosity of the ink and the surface energy of the target substrate. More surface energy on the target substrate will help the ink to bond more strongly with the substrate and then lead to a higher resolution printing. The reported resolution ranges from nano-meter to micro-meter.

### 2.4.3. Spray coating

The spray coating technology, as one of the popular printing technologies (**Figure 2.7(c)**) attracts attention due to its high efficiency to deposit materials on various substrates. This technology utilises the air pressure/electric field to drive a fine nozzle to spray the solution-based materials on the substrate. The substrates vary from cloth, polymer substrate to a conventional silicon substrate. The spray coating has the advantage of efficient material



usage and the technique suffers from poor resolution. It is often used for an entire substrate coating and with the combination of other printing technologies such as contact printing or transfer printing [186]–[189].

#### 2.4.4. Inkjet printing

Compared to spray coating, the inkjet printing can realise a versatile pattern directly from graphical designs in software (**Figure 2.7(d)**). This technology is a revolutionary of the traditional ink printer. However, it is still a dot-matrix based printer, in which all the patterns are composed of tiny dots. Those dots are driven by piezoelectrical crystals which are activated by an electronic circuit. The achievable resolution by inkjet printing is hugely dependent on the parameters such as the solution in the printing ink, the diameter of the nozzle and the distance between the targeting substrate. The inkjet printing technology has been widely used in fabricating organic thin-film transistors, solar cells and light emitting devices [190].

#### 2.4.5. Screen printing

The concept of screen printing is to spread and pattern the ink/paste directly on the substrate by the squeegee as categorised in additive manufacturing. The pre-defined pattern on the stencil will allow the ink/paste to only pass through a certain area. It is a mature technology which is often used for printing thick electrode or a printed circuit board. The printing qualities are decided by various factors, such as solution viscosity, printing speed, angle, pressure, the material of the squeegee, the space between screen and substrate, mesh size and substrate's property [102]. Screen printing has been demonstrated not only for printing on a flexible substrate, but also on a stretchable substrate. The drawback of this fabrication process is the limited resolution.

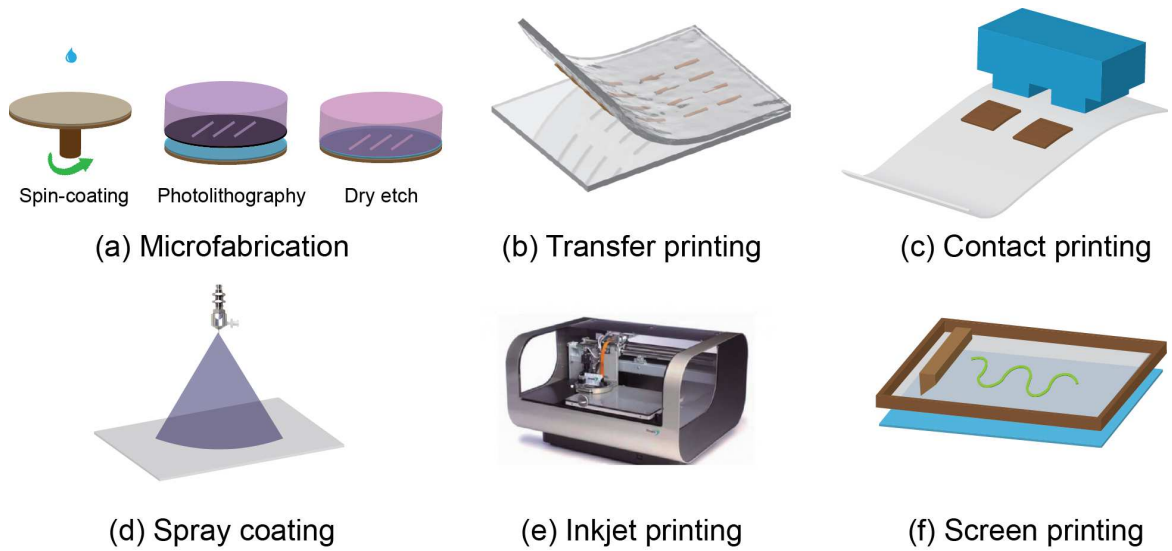


Figure 2.7: Graphical illustration of common fabrication technologies for realising stretchable interconnects including (a) Microfabrication, (b) Transfer printing, (c) Contact printing, (d) Spray coating, (e) inkjet printing and (f) Screen printing [238].

#### 2.4.6. Comparison between different printing technologies

The printing technologies of spray coating, inkjet printing and screen printing are compared in **Table 2.4**. In terms of the ink/paste for printing, different printing technologies require different rheological properties. In general, screen printing utilise more viscous ink or paste compared to the other printing technologies. The viscosity of the paste also influences the thickness of the final printed film. In industry, the thickness of the printed film is larger than  $0.5\ \mu\text{m}$  [191]. However, the screen-printed film with a thickness around  $100\ \text{nm}$  has been reported by a research group by using a diluted ink ( $10\ \text{mPa}\cdot\text{s}$  viscosity) [192]. Inkjet printing requires lower viscous ink, but the challenge is the clogging issue from the ink at the nozzle. It is a versatile printing process with an accurate alignment ( $\pm 0.5\text{--}25\ \mu\text{m}$ ) and fine resolution (down to  $20\ \mu\text{m}$ ) [190], [191], [193]. Spray coating is an effective material deposition process. This technique can accommodate the viscosity of ink ranging from  $5$  to  $440\ \text{mPa}\cdot\text{s}$  [194]. However, the patterning of spray-coated film requires the assistance of additional process such as photolithography or contact printing [194]–[196]. Based on the concluded ink requirement of these printing techniques and the reported results in **Table 2.4**, an efficient printing technique can be employed for different applications. In this thesis, the spray coating technique in combination with photolithography patterning was adopted to fabricate the PEDOT:PSS-based stretchable interconnects.

Table 2.4: Comparison in inks' viscosity, thickness of printed film, resolution of printing and accuracy among spray coating, screen printing and inkjet printing technologies.

	<b>Spray coating</b>	<b>Screen printing</b>	<b>Inkjet printing</b>
<b>Viscosity of inks (mPa·s)</b>	5-440 [194]	500-50000 [197]	1-40 [197]
<b>Thickness of printed film (μm)</b>	0.012-50 [194]– [196]	> 0.5 (industry) [191] 0.109±0.004 has reached with 10 mPa·s viscosity ink [192]	5-10 [190]
<b>Resolution (μm)</b>	NA	50-500 [192]	20-50 [190], [191]
<b>Accuracy (μm)</b>	NA	± 25 [191]	± 0.5-25 [193]

## 2.5. Approaches adopted in this thesis

In the framework of this thesis, stretchable interconnects combined between smart geometry designs with soft conductive materials are mainly investigated. Novel materials that exhibit high electrical conductivity and mechanical softness are still facing challenges in terms of the chemical stability, degradability, and process compatibility with established MEMS/CMOS technology. This thesis presents the solution for some of the challenges through various approaches.

- Polyimide (PI) film is adopted in this thesis to be used as a supporter of the metallic thin film. PI has Young's modulus of 2.34 GPa, which is between the metal (~90 GPa) and soft substrate (~ MPa). It has advantages including higher process temperature (300°C), stable under most of the solvents, acid and base solutions and can be patterned through photolithography technology. Hence, the Au-PI dual layer was patterned in a serpentine shape through multiple microfabrication steps including the photolithography, wet etching, and dry etching. The electrical response of fabricated Au-PI interconnects was characterised in both DC and AC ranges.
- Conductive polymers, such as PEDOT:PSS, have been pursued due to their dual property of being electrically conductive and mechanically soft. However, this

type of polymer is sensitive to the environment (i.e. humidity, solvent, temperature) and easily biodegradable. In addition, as it is mostly in solution, the process and patterning technologies are restricted to spray coating and inkjet printing, which have a limitation in resolution. In the approach adopted in this thesis, the Au-PEDOT:PSS hybrid film was investigated as stretchable interconnects. The Au metal layer serves not only as an electrical conductor, but also a protection of PEDOT film to avoid direct contact with water, acid and base solutions in the following photolithography step.

- Composites, as the popular candidates for stretchable interconnects, exhibit the high stretchable and high electrical conductivity due to the soft polymer matrix and high aspect ratio of conductive fillers, respectively. One of the drawbacks is their high contact resistance from the dielectric polymer matrix. The achieved composite has graphite flakes as conductive filler and PEDOT:PSS as a polymer matrix, which results in a low contact resistance ( $35\ \Omega$ ) and low sheet resistance ( $695.7\ \Omega/\square$ ). The stretchability of such composite can reach 80%, which is higher than the reported carbon-based composite.
- To demonstrate the applications of stretchable interconnects, the interconnects with the optimised design were integrated with a flexible electrochemical pH sensor and a stretchable RFID antenna. The overall stretchable electronic system allows a real-time sweat pH monitoring. Another application for stretchable interconnects was the movement monitoring of soft robotic fingers. The interconnects were integrated with CNT-based strain sensor through dielectrophoresis (DEP) method.

## Chapter 3 Design, modelling and simulation

The state-of-the-art technology on stretchable electronics, and particularly the stretchable interconnects discussed in the previous chapter, unveils the dilemma between material's electrical performance and mechanical softness. In order to optimise the thickness of the conductor and its coupled substrate, it is important to understand the mechanical interaction between them under the strain. In addition, these mechanical analysis help to determine the geometrical designs of interconnects as it plays an important role in optimising interconnects' stretchability without compromising their electrical performance. In this chapter, an in-depth mechanical analysis of various geometries with the assistance of Finite Element Method (FEM) simulation of stretchable interconnects is discussed.

### 3.1 Bendability and stretchability

In the view of classical mechanics, the stretchability refers to the maximum possible external strain that an elastic structure can withstand before breaking. The strain  $\varepsilon$  is expressed as the ratio between the elongation and original length  $\Delta L/L_0$ . When a bar is under uniaxial force from both ends, as illustrated in **Figure 3.1(b)**, the normal stress at the cross-section area  $A$  is generated, as represented by  $\sigma = \frac{F}{A}$ . Thus, the strain under that normal force can be expressed as  $\varepsilon = \frac{\sigma}{E} = \frac{F}{E \cdot A}$ , where  $E$  is the Young's modulus of the subject. The  $E \cdot A$  is also defined as axial rigidity and can be used as an index to estimate the stretchability of a subject. In the case of bending movement, the mechanical principle is different. The subject experiences a bending moment in order to obtain a bending movement. Such moment is

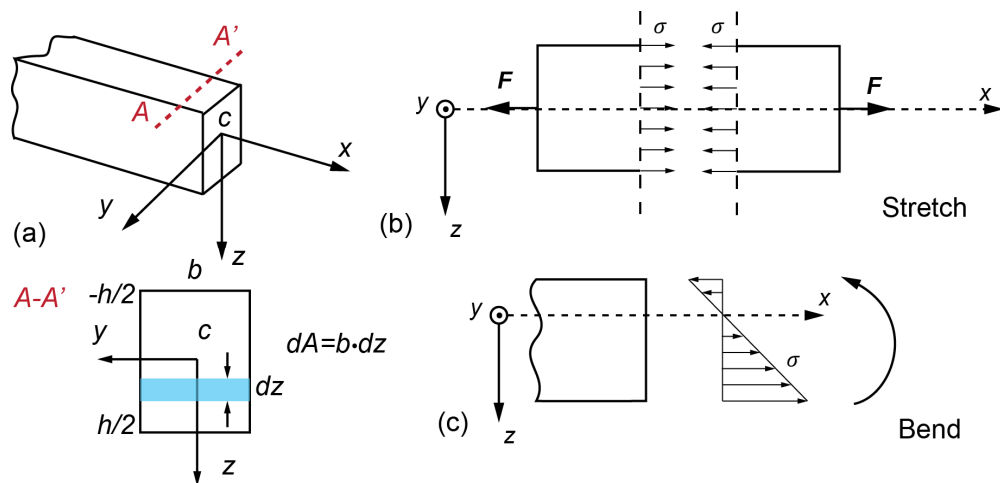


Figure 3.1: (a) Schematic illustration for the mechanics in a bar when it is subjected to (b) stretching and (c) bending movements [198].

equivalent to the sum of distributed normal stress, as illustrated in Figure 3.1(c), with respect to  $y$ -direction. If we integrate all the infinitesimal moments, the resultant moment can be referred to the moments of inertia:  $I = \int z^2 dA$ . If the cross-section is in rectangular as described in **Figure 3.1(a)**, the inertia can then be transferred into  $I = \int z^2 dA = \int_{-h/2}^{h/2} z^2 (bdz) = \frac{bh^3}{12}$  where  $b$  and  $h$  are the width and thickness of the bending structure. Similar to stretching, here the  $E \cdot I$  is defined as bending rigidity [198]. The term “bendability” usually refers to the minimum bending radius of certain structures. Unlike in axial rigidity, which only considers a cross-section’s area, the geometry in a cross-section, particularly the thickness of bending bar, plays an important role in its bendability. In general, the moving of a structure may involve stretching, bending and even twisting, which makes the mechanical analysis rigorous. Hence, the tool of Finite Element Method (FEM) simulation, such as ANSYS, COMSOL and Abaqus, has been widely used for mechanical, and even electrical analysis.

### 3.2 Thin film conductor on stretchable substrate

One of the methods to realise the stretchable interconnect is to deposit and pattern the noble metal (Au, Pt etc. ) directly on stretchable substrate (PDMS, Ecoflex etc.). The main issue with stretchable interconnects coupled with stretchable substrate is their large difference in mechanical property parameters such as Young’s modulus  $E$  and Poisson’s ratio  $\nu$ . Stretchable substrates, which are usually made of polymer elastomers, have a low Young’s modulus ( $\sim$ kPa to MPa) and a Poisson’s ratio of nearly 0.5. Hence, they can be easily stretched more than 100% and re-shaped after removing the stress. On the contrary, metallic thin film interconnects are limited in extension under stretching. When these two layers (metal-substrate) are stretched simultaneously, the metallic layer undergoes the stress generated from normal force from stretching, as well as an additional stress generated at

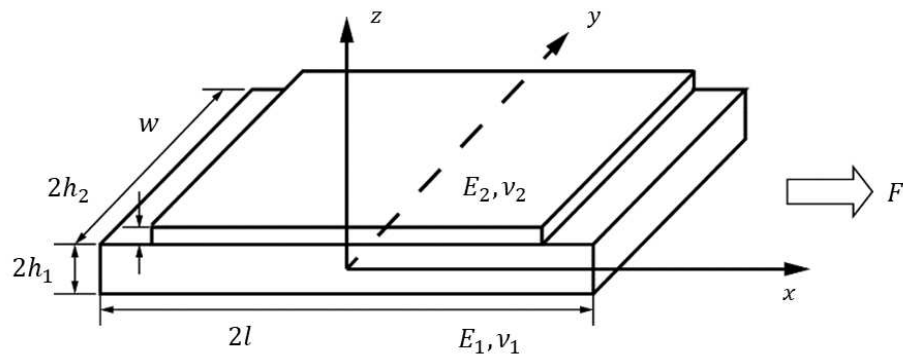


Figure 3.2: Mechanical analysis model for metallic thin film deposited on soft substrate.

metal/substrate interface which leads to cracks and delamination. Inspired by the work done by X. Chen *et.al.* [199], a model composed of a soft substrate (e.g. PDMS) and a rigid metallic thin film (e.g. gold) was built. As illustrated in **Figure 3.2**, a conducting film with the thickness of  $2h_2$  is bonded to the substrate which is  $2h_1$  thick. The dual-layer structure is clamped from one end and pulled from the other. The  $E_{1,2}, \nu_{1,2}$  represent the Young's modulus and Poisson's ratio of conducting film and soft substrate respectively. Under the equilibrium condition, the stress state for each layer can be written as below (**Equation 3.1 to 3.10**).

$$\frac{\partial \sigma_x}{\partial x} + \frac{\partial \tau_{yx}}{\partial y} + \frac{\partial \tau_{zx}}{\partial z} + f_x = 0 \quad (3.1)$$

$$\frac{\partial \tau_{xy}}{\partial x} + \frac{\partial \sigma_y}{\partial y} + \frac{\partial \tau_{zy}}{\partial z} + f_y = 0 \quad (3.2)$$

$$\frac{\partial \tau_{xz}}{\partial x} + \frac{\partial \tau_{yz}}{\partial y} + \frac{\partial \sigma_z}{\partial z} + f_z = 0 \quad (3.3)$$

$$\varepsilon_x = \frac{1}{E} [\sigma_x - \nu(\sigma_y + \sigma_z)] \quad (3.4)$$

$$\varepsilon_y = \frac{1}{E} [\sigma_y - \nu(\sigma_x + \sigma_z)] \quad (3.5)$$

$$\varepsilon_z = \frac{1}{E} [\sigma_z - \nu(\sigma_x + \sigma_y)] \quad (3.6)$$

$$\varepsilon_x = \frac{\partial u}{\partial x} \quad (3.7)$$

$$\varepsilon_y = \frac{\partial v}{\partial y} \quad (3.8)$$

$$\varepsilon_z = \frac{\partial w}{\partial z} \quad (3.9)$$

$$\gamma_{xy} = \frac{1}{2} \left( \frac{\partial u}{\partial y} + \frac{\partial v}{\partial x} \right) \quad (3.10)$$

To simplify the equation, the volume force (e.g. gravity) in three directions ( $f_{x,y,z} = 0$ ) and the stress in  $z$  direction ( $\sigma_z = 0$ ) are not considered. Because the applied normal force is in  $x$  direction, we have  $\varepsilon_y = 0, \gamma_{xy} = 0, \gamma_{yz} = 0$ . By rearranging the above equations, we can express the stress by the following equations:

$$\left(\frac{2-\nu}{1-\nu}\frac{\partial^2}{\partial x^2} + \frac{\partial^2}{\partial z^2}\right)\sigma_x = 0 \quad (3.11)$$

$$\frac{\partial\sigma_x}{\partial x} + \frac{\partial\sigma_{xz}}{\partial z} = 0 \quad (3.12)$$

By solving the **Equation 3.11&3.12**, the normal stress  $\sigma_{xx}$  and shear stress  $\sigma_{xz}$  can be represented as shown in **Equation 3.13&3.14**.

$$\sigma_{xx}^{(i)}(x, z) = \sigma_0^{(j)}\delta_{ji} + \alpha_i \sum_n^\infty [A_{ni} \sinh(\alpha_i p_n z) + B_{ni} \cosh(\alpha_i p_n z)] \cos(p_n x) \quad (3.13)$$

$$\sigma_{xz}^{(i)}(x, z) = \sum_n^\infty [A_{ni} \cosh(\alpha_i p_n z) + B_{ni} \sinh(\alpha_i p_n z) + C_{ni} p_n] \sin(p_n x) \quad (3.14)$$

The superscripts  $i, j$  indicate the layer, while the parameter  $\alpha$  and  $p$  are  $\alpha_i^2 = \frac{2-\nu_i}{1-\nu_i}$  and  $p_n = \frac{(n+1/2)\pi}{l}$ . The constants  $A, B, C$  in the equations are determined by boundary conditions.

First, we have the free rolling surface:  $\sigma_{xz}^{(1)}(x, -h_1) = \sigma_{xz}^{(2)}(x, h_2) = 0$ . Then it is assumed that there is a perfect bonding between the conducting film and the substrate, which indicates that there is no relative movement between the two layers:  $\sigma_{xz}^{(1)}(x, h_1) = \sigma_{xz}^{(2)}(x, -h_2) = 0$ ;  $u^{(1)}(x, h_1) = u^{(2)}(x, -h_2)$ . Moreover, there is no force on  $z$  direction:  $\sum_{i=1}^2 \int_{-h_i}^{h_i} \sigma_{xz}^{(1)}(x, z) dz = 0$ . Considering the dual layers that are composed of PDMS ( $E_1 \sim \text{MPa}$ ,  $\nu_1 = 0.49$ ) and gold ( $E_2 \sim \text{GPa}$ ,  $\nu_2 = 0.4$ ), with the thickness  $h_1 = 200 \mu\text{m}$  and  $h_2 = 0.1 \mu\text{m}$ , the normal stress and shear stress are calculated by a Matlab code. From the results in **Figure 3.3**, it can be concluded that the stress in  $xx$  direction (normal direction) is much higher than the stress in  $xz$  direction (shear direction). However, for stress both in normal direction and shear direction, the stress is concentrated at the boundary area between the substrate and conductor, which contributes to the failure of the conductor.



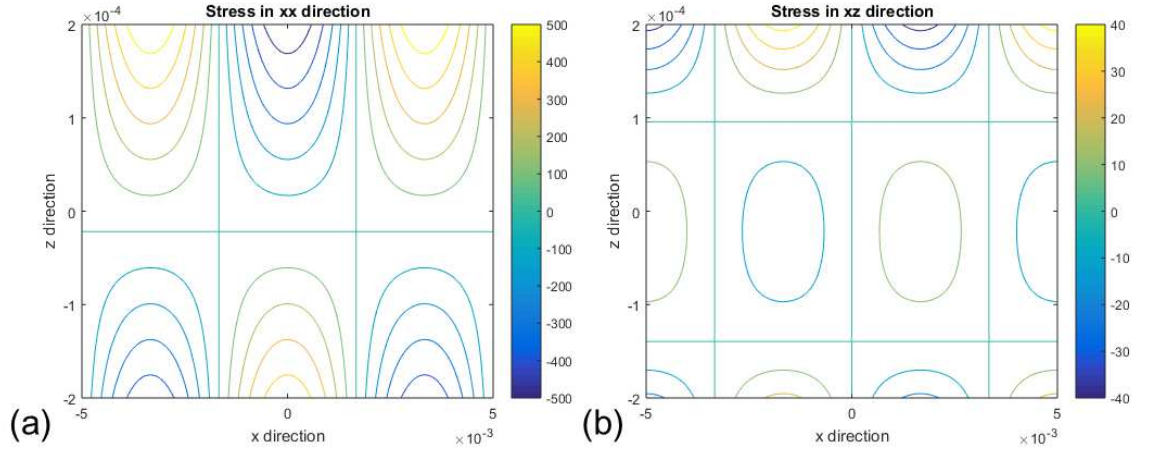


Figure 3.3: Calculation results from Matlab regarding the normal stress and shear stress that substrate and conductor experienced while stretching.

To further investigate the effect of materials' property ( $E_{1,2}, \nu_{1,2}$ ) and thickness ( $h_{1,2}$ ) on resultant normal stress in the film and the shear stress at the boundary more accurately, the Finite Element Method (FEM) simulation (COMSOL Multiphysics<sup>®</sup>) tool was adopted. In the FEM simulation model, the substrate PDMS has a thickness of 0.16 mm and the conductor Au has a thickness of 100 nm. These parameters are chosen to allow the simulation model to be in consistence with experimental data. The length and width of both substrate and conductor are 10 mm and 7 mm respectively. The conductor is perfectly bonded to substrate and the dual-layered film has one fixed-end and the other end pulled. The external force elongates the dual-layered film to a prescribed distance. Under different

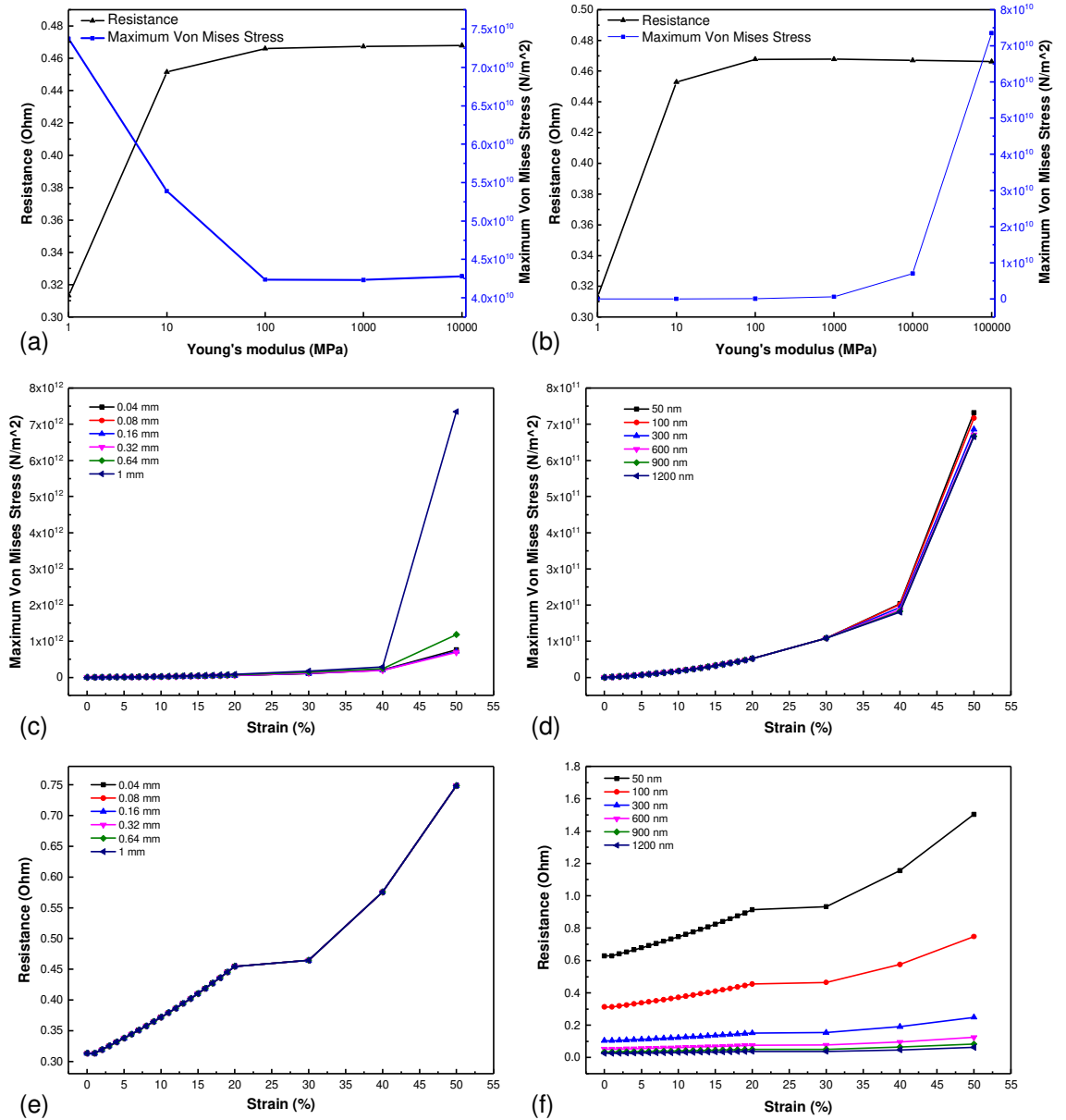


Figure 3.4: FEM simulation results: comparison between the resistance and maximum von Mises stress within the conductor when the Young's Modulus of (a) substrate was swept between 1 MPa to 10 GPa and (b) conductor was swept between 1 MPa and 100 GPa; Maximum von Mises stress in conductor with (c) the thickness of substrate varies from 0.04 mm to 1mm and (d) the thickness of conductor varies from 50 nm to 1200 nm when the dual-layered film is stretched up to 50%; Variation of resistance when the film is stretched up to 50% with a change in (e) substrate (f) conductor's thickness.

degree of stretching, the maximum von Mises stress and overall resistance in the conductor are monitored. The von Mises stress is a strength hypothesis, which can also be called as Maximum-distortion-energy hypothesis. It predicts whether the material becomes critical

when energy needed for distortion reaches a critical value [198]. The resistance can reflect the deformation in the conductor.

The first simulation study is to investigate the influence of substrate and conductor's Young's modulus ( $E$ ) on conductor's resistance variation and the maximum experienced stress. As depicted in **Figure 3.4(a-b)**, an increase in substrate's Young's modulus, from 1 MPa to 10 GPa, can reduce the von Mises stress when the film is under 2% strain. This is because the increase in substrate's Young's modulus reduces the difference between the conductor and the substrate's modulus and thus reduces the shear stress between the two materials under strain. On the other hand, the increase in conductor's Young's modulus leads to a larger difference with the substrate and dramatically increases the von Mises stress within the conductor. Then the influence of each layer's thickness is discussed. When the substrate's thickness increases from 0.04 mm to 1 mm, the von Mises stress in conductor does not show much difference before the strain reaches 40%. Afterwards, thicker substrate (0.64 mm, 1 mm) show a significant increase in stress. However, the resistance of conductor doesn't indicate much change as shown in **Figure 3.4(c,e)**. If the mechanical property of substrate is fixed, the change in conductor's thickness leads to a different trend compared with previous results. The variation in conductor's thickness won't change much in its von Mises stress as this is more influential by the interface between two different materials. However, the thickness of the conducting film is vital to the change in resistance. From the results in **Figure 3.4(d,f)**, it can be concluded that the thicker the conductor is, the less influence the external strain can have on its resistance. However in reality, the thicker conductor means higher cost and the conductor's thickness is also limited by process technologies.

In conclusion, the thickness of substrate will not influence the overall resistance of conducting film but stress. It is not recommended to use thick substrate that is above 0.64 mm for a high degree of stretching. Moreover, the thickness of conducting film above 300 nm will help to reduce the change in resistance under stretching. The effective method to reduce the von Mises stress in the conductor is to select the conductive material with its Young's modulus in the range of 1-1000 MPa and thickness above 300 nm.

### 3.3 Serpentine-shaped interconnects

The previous section focuses on the coupling effect between conductive thin film and soft substrate. Such coupling effect is influenced by the mechanical properties of substrate and conductor and their thickness. In this section, the influence of the conductor's geometry will be discussed. A common strategy to design stretchable interconnects is to utilise the serpentine shape, as illustrated in **Figure 3.5**. The curved design within the interconnect will help to redistribute the normal stress which is caused by stretching. This can be explained by the Saint-Venant's principle. Considering the cross-sections along the serpentine-shaped interconnects, as pointed out in A-A', B-B' and C-C' in **Figure 3.5**,  $L_3$  exhibits longer than  $L_1$  and  $L_2$ , which leads to a higher cross-section area. Hence, the stress generated at this area turns out to be lower, as  $\sigma = \frac{F}{A}$ . The crest area (B-B') with the narrowest width is expected to concentrate higher stress than other locations in interconnects. In this way, compared with the straight line as interconnects, the serpentine-shaped interconnects are expected to have much higher stretchability.

With the assistance of FEM simulation software (COMSOL), a further investigation has been made for an optimised stretchable interconnect design. A collection of different stretchable interconnects are compared, as shown in **Table 3.1**. The name of the design, such as "Serp XX", depends on the degree of arc curvature in the serpentine-shaped interconnect. The geometrical elongation ratio is the variation between the lengths in perimeter of the curved interconnect and the shortest distance between two electrodes for clamps. This distance is kept constant to be 10 mm for all the interconnects designs and the width of interconnects is 0.5 mm. The model in the simulation is composed of a 100 nm-thick metallic interconnect and 0.16 mm-thick elastic PDMS substrate. The thickness values are chosen to be consistent with experimental results. The material parameters are listed in **Table 3.2**. In the material's parameter, the PDMS is modelled as hyper-elastic polymer (Neo-Hookean model). This model can predict non-linear stress-strain behaviours of materials. The Lamé

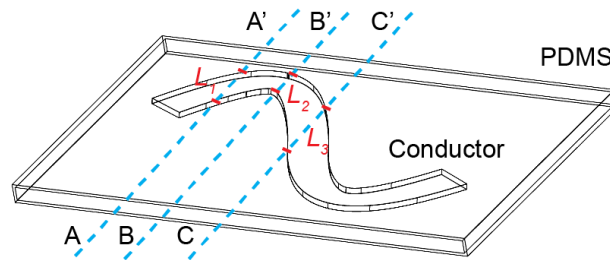


Figure 3.5: Schematic illustration for the mechanics in the serpentine-shaped conductor.

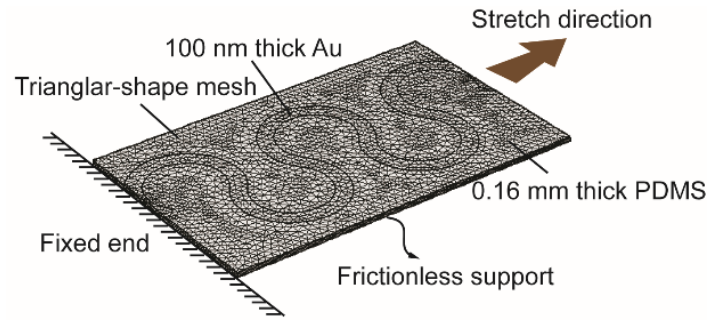


Figure 3.6: Boundary condition of the FEM model.

parameters are the material-dependent quantities to describe the elasticity and shear modulus of a material [200]. The FEM meshed model with boundary conditions are illustrated in **Figure 3.6**. The interconnect is modelled as perfectly bonded to a PDMS substrate, which means that no relative dislocations are expected between two layers. Both layers are fixed at one end and stretched with a step distance of 1 mm from the other end. The substrate is modelled to have a frictionless support. In COMSOL simulation, a Solid Mechanics module is used to define mechanical movement and boundaries, AC/DC module is used to monitor the resistance of interconnects along with the stretching movement. As compared in **Figure 3.7**, the concentrated von Mises stress can be found at the crest in the serpentine-shaped interconnects and the apex in triangular-shaped interconnects. However, for the interconnect with straight line design, the highest stress is found at the fixed end. The resistance of interconnects increases along with the increase in strain due to the extension in its length and shrinkage in the cross-section area. After reaching 80% strain, the simulation results show a non-linear behaviour which will be considered as the plastic region of materials. The variation in resistance of different designs against strain is shown in **Figure 3.8**. The design with  $260^\circ$  in arc curvature reveals the most stable resistance against strain. Since the resistance variation is strongly linked with the strain, which will be discussed in the next section, the sequence of stretchability with respect to different designs can be summarised as follows: Serp260 > Serp45 > Triangle > Serp180 > Serp60 > Straight line. From the point of view of geometrical elongation ratio in **Table 3.1**, “Serp180” design supposes to have larger stretchability than “Triangle” and “Serp45” designs, since it has longer length in perimeter. The maximum von Mises stress indicated in **Figure 3.7** also indicates the higher value in the “Serp 180” design. This result indicates that the geometrical deformation ratio is not the only factor for stretchability.

Table 3.1: Geometry design of stretchable interconnects.

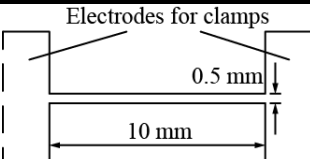
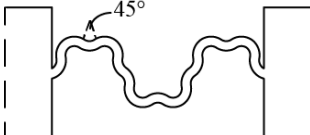
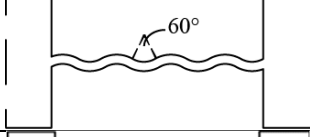
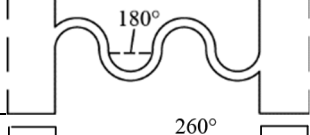
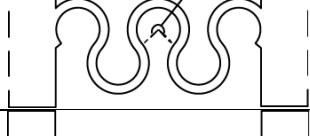

Name	Schematic	Geometrical elongation ratio
<b>Straight line</b>		0
<b>Serp 45</b>		33.4%
<b>Serp 60</b>		3.7%
<b>Serp 180</b>		55.6%
<b>Serp 260</b>		180%
<b>Triangle</b>		34.5%

Table 3.2: Material parameters used in COMSOL simulation.

Material	Young's Modulus	Poisson's ratio	Electrical conductivity
<b>PDMS</b> (Neo-Hookean model)	Lamé parameter $\lambda$ : 6.93 GPa Lamé parameter $\mu$ : 0.77 GPa	0.49	$2.5 \times 10^{-14}$ S/m
<b>Au</b>	70 GPa	0.4	$4.56 \times 10^6$ S/m

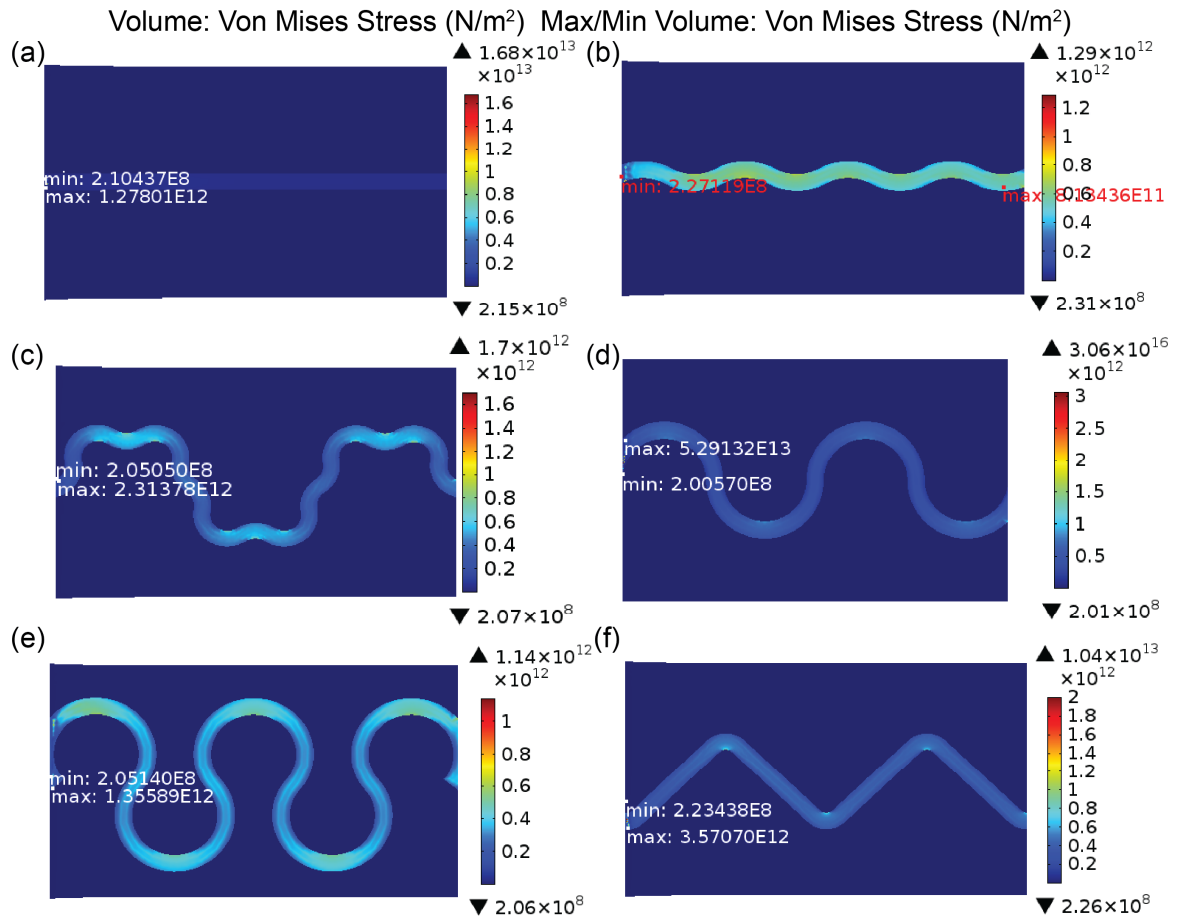


Figure 3.7: The concentrated von Mises stress and the location of maximum von Mises stress within different interconnects under 70% stretching.

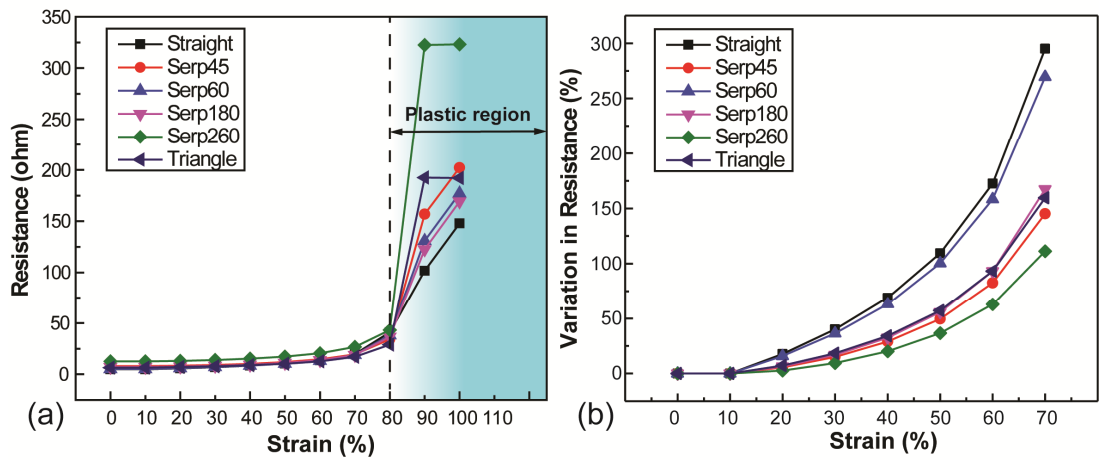


Figure 3.8: (a) Resistance of stretchable interconnects with different geometry design during stretching, (b) The variation in resistance of stretchable interconnects with different geometry design up to 70% stretching.

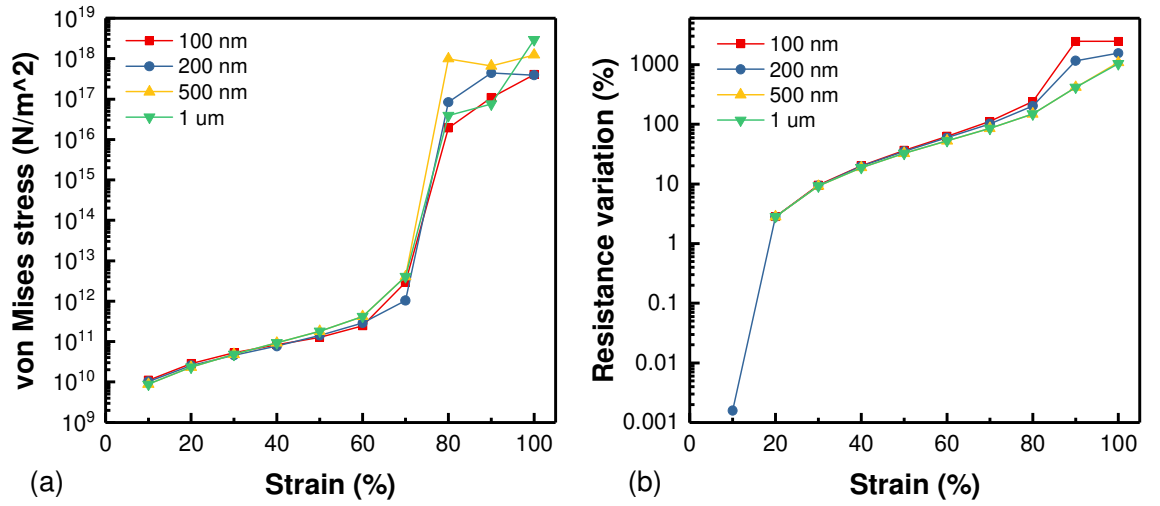


Figure 3.9: Von Mises stress and resistance variation in serpentine-shaped interconnect under strain up to 100% when the thickness of interconnects vary from 100 nm to 1 μm.

In particular for the interconnect design with arc degree of 260°, the variation in the thickness of interconnect shows negligible influence on von Mises stress, as shown in **Figure 3.9(a)**. For the resistance variation (**Figure 3.9(b)**), no significant change by the thickness was found within 60% strain. Above 60% strain, the thicker (1 μm) interconnects show a lower resistance variation.

### 3.4 Electro-mechanical behaviour of interconnects

The interconnects are conductors as well as inductors. In low frequencies, the resistance variation in interconnects are the results of their deformation under stretching. In general, the length increases and the cross-section reduces when the interconnect is under tensile strain. The resistance of interconnect can be expressed as follows:

$$R = \rho \cdot \frac{L}{A} \quad (3.15)$$

If the natural logarithm is taken from both sides, the formula can be modified into:

$$\ln R = \ln \rho + \ln L - \ln A$$

If the conductor is assumed to have a circular cross-section, where  $A = \pi r^2$ .



Then the formula can be transferred into  $\frac{dR}{R} = \frac{d\rho}{\rho} + \frac{dL}{L} - 2\frac{dr}{r}$

Since the strain in radius direction can be transferred in longitudinal direction

$$\varepsilon_r = \frac{dr}{r} = -\nu \frac{dL}{L}$$

The formula can then be changed into  $\frac{dR}{R} = \frac{d\rho}{\rho} + (1 + 2\nu)\frac{dL}{L}$  where  $\frac{dL}{L} = \varepsilon$

Finally, it can be obtained into  $\frac{\Delta R}{R} = \varepsilon * (1 + 2 * \nu) + \frac{\Delta\rho}{\rho}$ .

If the piezoresistive effect change in resistance is omitted:  $\frac{\Delta\rho}{\rho} = 0$ , the resistance variation of interconnect with a round cross-section is decided by the applied strain  $\varepsilon$  and twice of its Poisson's ratio  $\nu$ .

In the AC range, the interconnects are regarded as inductor. The inductance is a property of conductor when the electrical current flows within the conductor changes, a voltage can be induced as expressed in the following equation:  $V = L \frac{di}{dt}$ . At low frequency ( $<1$  MHz), the skin effect is not considered in the conductor. In addition, in the study of this thesis, the thickness of conductor is in the order of nanometer, where the length of the conductor is in millimeter range. Hence, the model can be analysed as a thin tape model, of which the inductance can be simplified into **Equation 3.16** [201].

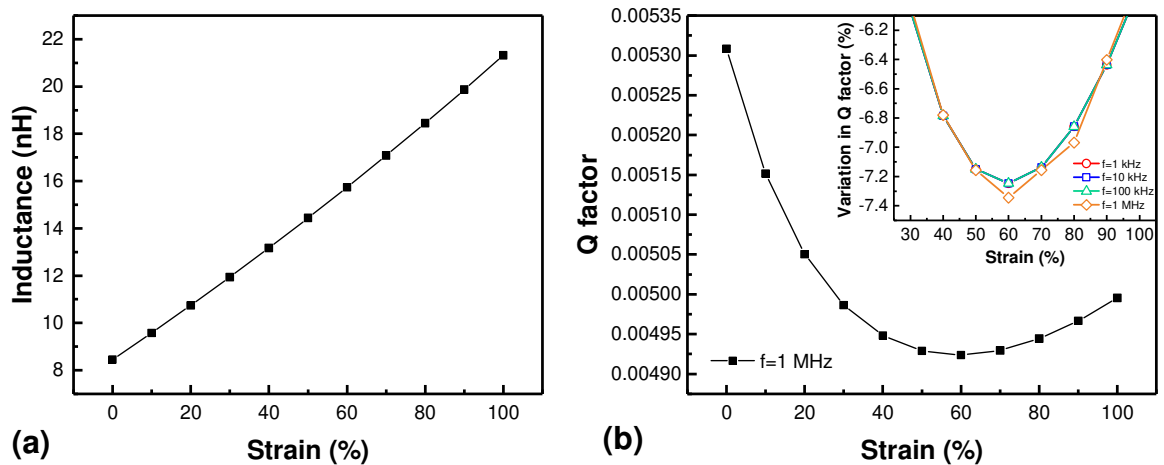


Figure 3.10: Calculation results of inductance and Q factor's variation of a straight conductor under external strain.

$$L = \frac{\mu_0}{6\pi a^2} \left[ 3a^2 l \ln \frac{l + \sqrt{l^2 + a^2}}{a} - (l^2 + a^2)^{\frac{3}{2}} + 3al^2 \ln \frac{a + \sqrt{l^2 + a^2}}{l} + l^3 + a^3 \right] \quad (3.16)$$

Where  $a$  and  $l$  are the width and length of the conductor. When the conductor is under external strain  $\varepsilon$ , the length will be stretched to  $l_0(1 + \varepsilon)$  and the width will reduce to  $a_0(1 - \varepsilon \cdot \nu)$ . Then the inductance will change with respect to the variable  $\varepsilon$ . If the original length of conductor is assumed to be 10 mm, the original width to be 0.5 mm and the Poisson's ratio to be 0.34, the trend of inductance with respect to the strain can be plotted in **Figure 3.10(a)**. Low inductance ( $\sim$ nH) is expected from a thin film metallic conductor. The inductance value is observed to have a monotonic growth along with the increase in strain. The Q factor, which defines the bandwidth of the circuit, is formulated as  $Q = \frac{\omega L}{R}$ . The influence of strain on Q factor come from both resistance  $R$  as discussed in the previous section and inductance, the variation trend of Q can be plotted in **Figure 3.10(b)**. As can be noticed from the asymmetric dipping trend curve, the decrease of Q factor saturates when the strain reaches 60% and then recovers. This reveals that in low strain range ( $<60\%$ ), the variation in resistance of the conductor dominates the Q factor trend, while at larger strain, the inductance shows a more significant change compared to resistance. In the inset of **Figure 3.10(b)**, the variations of Q factor are compared under different signal frequencies. In the range between 1 kHz and 1 MHz frequencies, the trend of Q factor exhibits the same. Minor variation of Q factor is observed at the 60 % strain region. This may result from the nonlinearity of the conductor's dimension under stretching.

## Summary

This chapter briefly reviewed the classical mechanics and extensively studied the mechanism for conductor-substrate dual layer through mechanical analysis. The mechanical analysis reveals that under the strain, the bonding region between the conductor and substrate experiences a concentrated stress, which leads to the failure of conductor. Further studies indicate that the stress can be reduced if the difference in Young's modulus between conductor and substrate is less. The stress value will not have significant influence by the variation in thickness of either conductor or substrate. However, the resistance variation with a thinner conductor is larger than the thicker one. Aside from the planar conductor, various shapes of conductor/interconnect were discussed. The general solution for stretchable interconnects is to adopt a serpentine shape, which is based on the principle of increasing

the conductor's cross-section to reduce stress. With the assistance of FEM simulation software, a comparison has been carried out between different designs of interconnects regarding their maximum von Mises stress and the resistance variation against external strain. Simulation results show that the interconnects' resistance variation with higher degree in arc curvature is less influential by the strain. In addition, the stress will be concentrated at the crest area within the serpentine-shaped conductor. Unlike the planar conductor, the serpentine-shape design varies less in resistance with different thicknesses. The correlation between electrical performance and mechanical deformation was investigated in both DC and AC regions. In DC region, the resistance variation exhibits a linear relationship with the applied strain. The slope is the Poisson's ratio  $\nu$  of the conductor. In AC region ( $f=1$  MHz), the inductance variation has a higher degree of complexity in equation. The Matlab calculation indicates a linear trend with inductance with respect to strain. The Q factor, on the other hand, can be plotted in an asymmetric dipping curve. The Q factor falls in the strain range between 0 to 60% and then increases from 60% to 100%. Guided by the result from simulation and analysis, the thickness of substrate is designed to keep below 0.64 mm, while the thicker conductor ( $> 100$  nm) is preferable. In addition, the geometry design of stretchable interconnects is optimised with "Serp 260" design.

## Chapter 4 Fabrication of stretchable interconnects

This chapter elaborates the fabrication process of stretchable interconnects. In all, three types of stretchable interconnects were developed comprising metallic thin film based interconnects, metal-conductive polymer hybrid interconnects and metal-polyimide dual layered interconnects. The geometries of fabricated interconnects are the same as the FEM simulated designs discussed in Chapter 3. For all the interconnects, the soft elastomer PDMS was chosen as stretchable substrate. However, as mentioned in **Chapter 2**, there are challenges for PDMS substrate, as it is sensitive to temperature variations, which restricts the process temperature. The PDMS surface is super-hydrophobic, which leads to poor adhesion with metals and poses difficulties for depositing the materials that contain water. Methodologies have been investigated to resolve these issues and the protocols for processing conductive materials on the PDMS substrate have been developed.

### 4.1 PDMS substrate and metallic thin film interconnects

PDMS, as a stretchable substrate, is a polymer composed of repeating siloxane,  $\text{SiO}(\text{CH}_3)_2$  units as shown in **Figure 4.1(a)**. It has a strong adhesion with silica because of the hydrogen bond formed between oxygen in PDMS and silanol group on silica surface [202]. Hence, before depositing the PDMS solution, the silicon carrier wafer (with native oxide) was first silanised in chlorotrimethylsilane vapour for 30 minutes at room temperature. The chlorotrimethylsilane vapour introduces the silane group and replaces the  $-\text{OH}$  group with  $-\text{Si}-\text{CH}_3$  bond to help PDMS film to be easily removed, as illustrated in **Figure 4.1(b)**. The main process for fabricating metallic interconnects on PDMS substrate is illustrated in **Figure 4.2**. The PDMS solution (base: crosslink=10:1) (Dow Corning, USA) was spun-coated on top of silanised silicon carrier wafer at the rate of 500 rpm for 60 seconds to attain a thickness of 160  $\mu\text{m}$ . The PDMS substrate was then cured under 90°C for 2 hours. A short period of oxygen plasma treatment was performed before the e-beam evaporation of metal. Here the metallic film was chosen as gold (Au) as it is highly conductive, inert to oxidation and ductile. An additional thin layer of Ti or Cr (~5 nm) can be evaporated prior to the Au to further enhance the adhesion. The metallic thin film was then patterned through photolithography and wet etching.

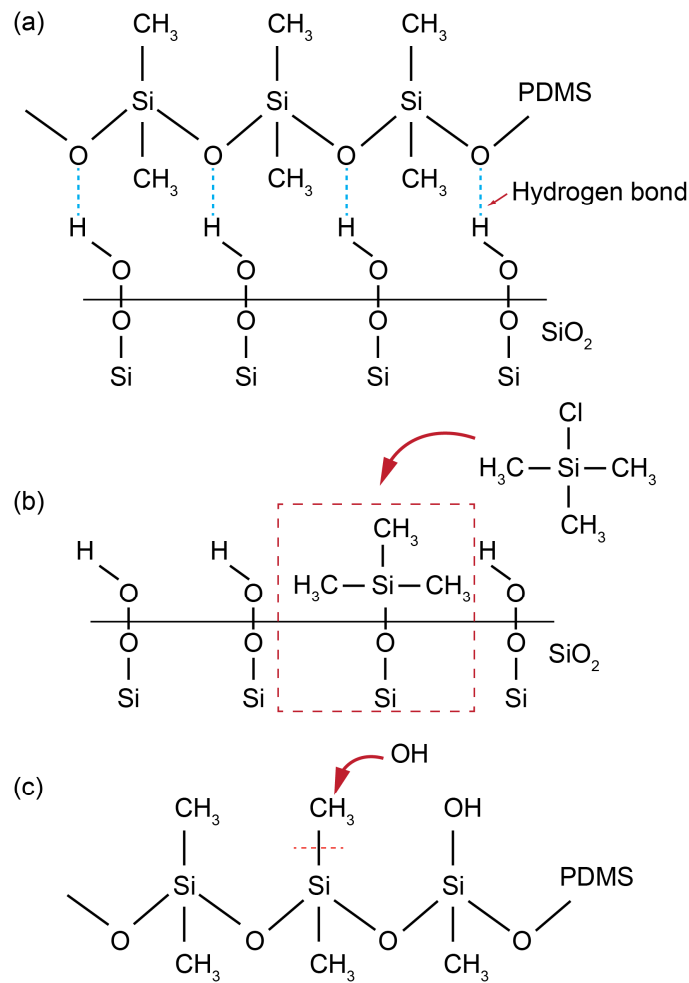


Figure 4.1: The binding mechanism between PDMS and silica (a) without surface modification, the hydrogen bond is formed and leads to strong adhesion between PDMS and silica surface, (b) the chlorotrimethylsilane  $(\text{CH}_3)_3\text{SiCl}$  replaces the  $-\text{OH}$  bond with  $-\text{SiCH}_3$  to reduce the adhesion and (c) the effect of oxygen plasma on PDMS surface with the introduce of  $-\text{OH}$  bond to convert hydrophobic PDMS surface into hydrophilic.

One of the challenges during the fabrication process is the hydrophobic nature of PDMS substrate. This feature from PDMS results a poor adhesion to the deposited conductor. The oxygen plasma modifies the surface of PDMS substrate, as explained in **Figure 4.1(c)** enriching the PDMS surfaces with siloxyl groups ( $\text{Si}-\text{OH}$ ) by oxidation of the methyls in the exposed polymer chains, which can convert the surface of PDMS from hydrophobic into hydrophilic [203].

Another challenge comes from the large interfacial stress generated between the deposited metallic film and PDMS substrate. During the metal depositing process, an intrinsic stress is developed in the metallic film. After the film was deposited, this internal

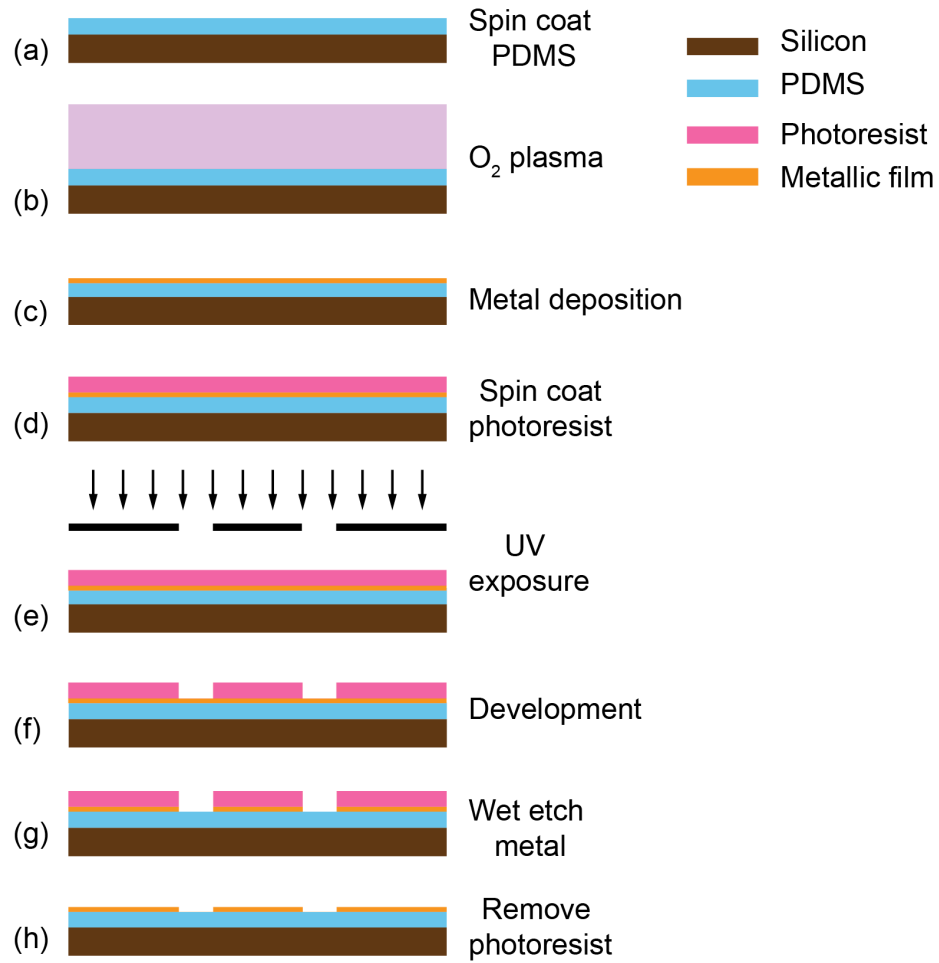


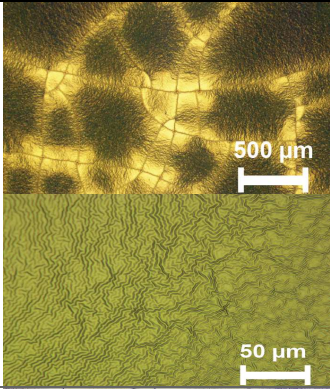
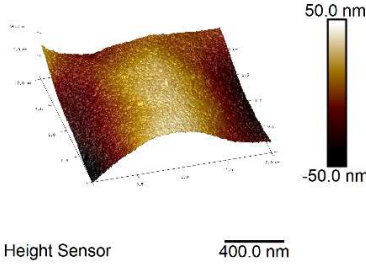
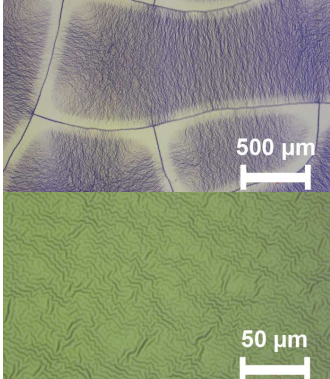
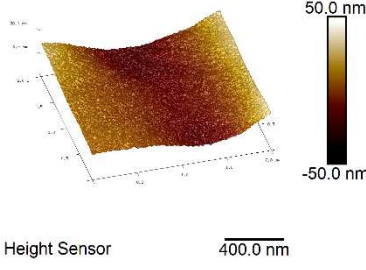
Figure 4.2: Fabrication process for depositing and patterning gold directly on PDMS substrate.

stress tends to release. Since PDMS is a soft substrate, the metallic film releases the stress, which leads to cracks. As reported, a low metal deposition rate can reduce the internal stress level to a certain extent [204]. Hence, the deposition rate was kept down to 0.04 nm/s. The thickness of deposited Au film is 100 nm. The density of cracks generated within the deposited film significantly reduced observed through a microscope. To further improve the process, an oxygen plasma treatment on PDMS was investigated under varied durations. A comparison between the plasma condition and substrate surface morphology has been investigated, as listed in **Table 4.1**. Confirmed by Atomic Force Microscopy (AFM) (Nanoscope, ScanAsist Mode, Brucker IconAFM, U.S) measurement, the surface roughness reduced from 17.3 nm to 10.7 nm after increasing the duration of oxygen plasma from 10 seconds to 30 seconds. After 60 seconds exposure, the surface becomes smooth, with a roughness of 2.21 nm. However, the cracks in the resulting film can still be noticed. Observed from an optical microscope, the density of cracks was reduced. A further study was conducted to investigate the effect of depositing pure Au layer on top of PDMS substrate. The deposited Au film was first inspected through an optical microscope, as shown

in **Table 4.2**. No cracks have been observed on all the samples of which the metal was deposited under different plasma conditions. However, under the AFM scanning, the nano-scale cracks can be found. As shown in **Table 4.2**, a short time (10 seconds and 30 seconds) plasma do not benefit the Au film to significantly reduce the cracks. 60 seconds oxygen plasma resulted in a crack-free metallic film on PDMS substrate.

As shown in **Figure 4.2**, after depositing a crack-free metal film (Au) on PDMS substrate, the photolithography step was carried out to define the pattern of stretchable interconnects. The photoresist was used as a protection layer for the wet etch of Au layer. The wet etch of Au was realised through 15 seconds bath in Potassium Iodide (KI) solution. The patterned interconnects were inspected through the Scanning Electron Microscopy (SEM) image (**Figure 4.3**). In the high magnified SEM image, significant wrinkles present on the deposited Au film as well as PDMS substrate. This surface morphology may be due to the elasticity of PDMS substrate, of which the surface experienced an expansion and reduction during the process of metal deposition [205]. The oxygen plasma treatment can reduce the effect of wrinkles, as compared in AFM images (**Table 4.1**).

Table 4.1: Comparison of change in morphology of Ti-Au film under different oxygen plasma conditions.

Metal	Process	Microscopic Image	AFM	Surface Roughness
Ti-Au (10-50 nm)	O <sub>2</sub> plasma 10s @80W			R <sub>q</sub> : 17.3 nm R <sub>a</sub> : 14.4 nm
				R <sub>q</sub> : 10.7 nm R <sub>a</sub> : 8.79 nm

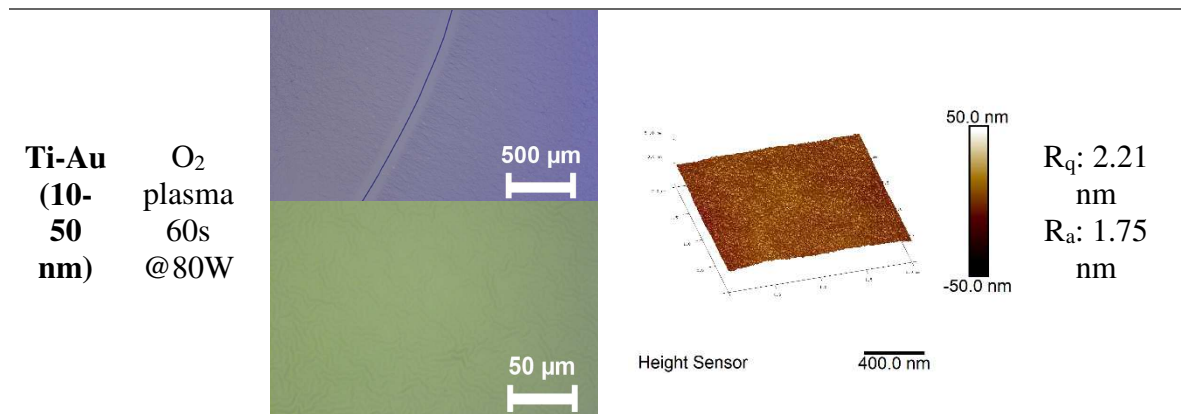
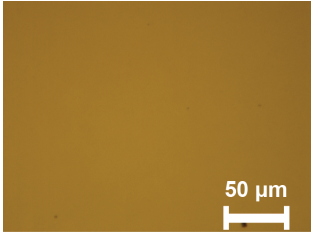
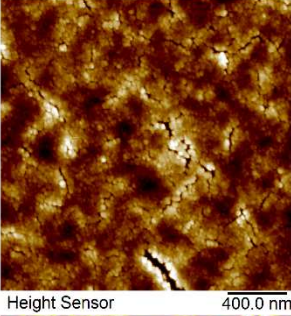
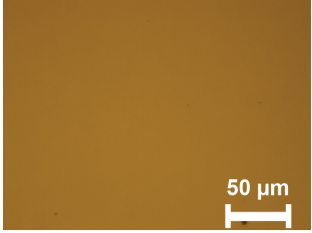
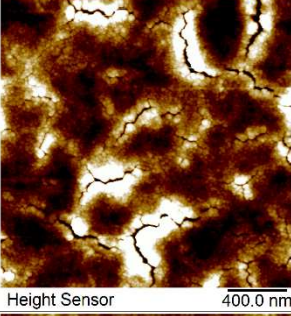
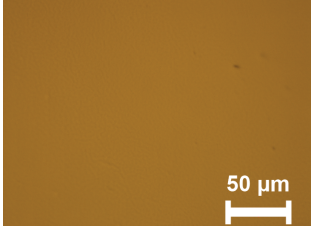
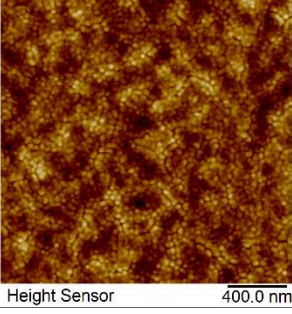


Table 4.2: Comparison of change in morphology of Au film under different oxygen plasma conditions.

Metal	Process	Microscopic Image	AFM	Surface Roughness
Au (50 nm)	No plasma			R <sub>q</sub> : 6.47 nm R <sub>a</sub> : 5.03 nm
	O <sub>2</sub> plasma 10s @80W			R <sub>q</sub> : 11.8 nm R <sub>a</sub> : 9.11 nm
	O <sub>2</sub> plasma 30s @80W			R <sub>q</sub> : 4.18 nm R <sub>a</sub> : 3.34 nm



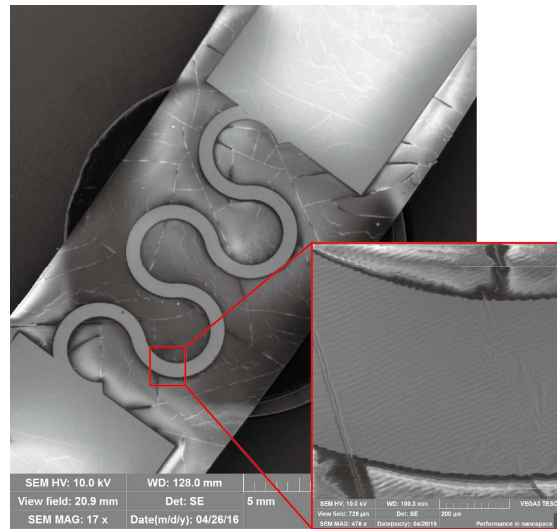
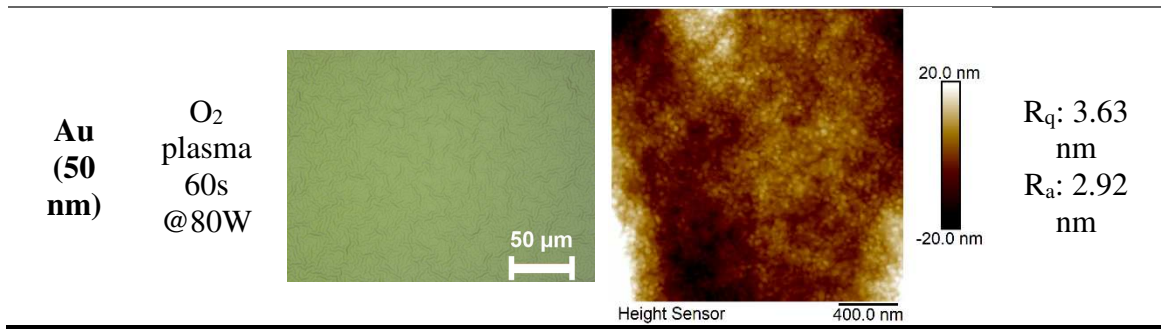


Figure 4.3: SEM image of patterned gold interconnect on PDMS substrate.

## 4.2 Metal-conductive polymer hybrid film interconnects

To overcome the presence of cracks in the metallic conductor under stretching, soft conductors have been studied. The conductive polymer Poly (3,4-ethylenedioxythiophene)-Poly (styrenesulfonate) (PEDOT:PSS) is widely used due to its ability to maintain electrical properties while being mechanically soft. However, the electrical conductivity of PEDOT:PSS film is moderate compared with metallic conductors. In addition, such conductive polymer is sensitive to moisture, which brings the challenge for a long-term stability. To address these issues, a hybrid structure with metal-conductive polymer interconnects was proposed. The deposited metal on top of the PEDOT: PSS film serves not

only as a protective layer from water and chemicals, but also highly enhances the electrical conductivity of the hybrid structure. In addition, the PEDOT:PSS film can be served as a stress release buffer between the brittle metallic film and soft elastic substrate. As described in **Figure 4.4 & 4.5**, the cracks generated in the top metallic film due to the external strain will not immediately lead to a break in electrical connection. The metallic islands still partially connect and build the electrical conducting path. Even up to a certain strain level, the electrical conducting path will not disconnect. Compared to the structure with metallic conductor on the PDMS, the underlying PEDOT:PSS film in the hybrid structure will keep the separated metal islands electrically connected.

Effect of Au and PEDOT:PSS film work in combination

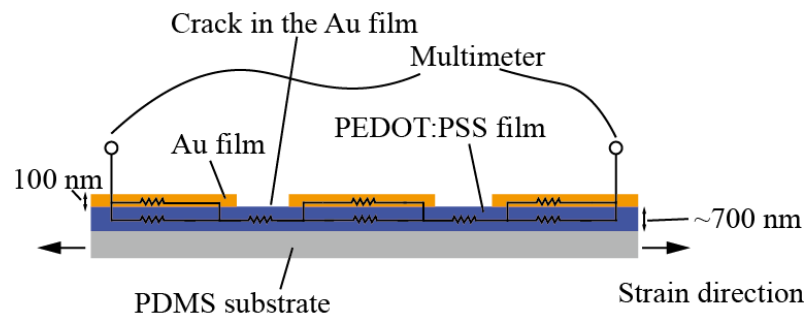


Figure 4.4: Schematic diagram of the cross-section view when Au-PEDOT:PSS dual-layer is under applied strain. The PEDOT:PSS underlying layer provides the electrical path in the cracks area.

The PEDOT: PSS is a conductive polyelectrolyte complex. The conductive part is the positive charged PEDOT, while the PSS part is to balance the doping charges and makes PEDOT easier to be dispersed in water [93]. Although PSS contributes to a better dispersion of PEDOT in water, it blocks the connection of conductive PEDOT molecules and lowers the resulting electrical conductivity in the film. In order to enhance the conductivity of

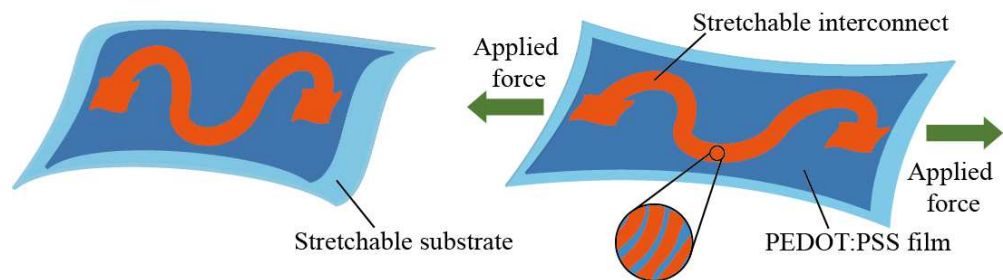
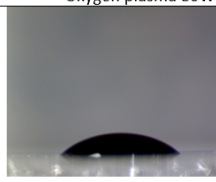
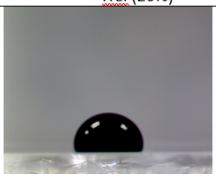
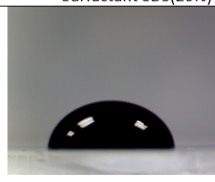
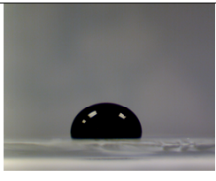

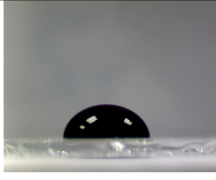
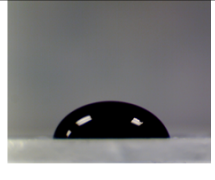


Figure 4.5: Schematic representing the effect under an applied strain in interconnect with underlying layer of PEDOT:PSS.

Table 4.3: Comparison in contact angle with different methods of surface treatment on PDMS substrate.

	Oxygen plasma 80W			HCl (20%)			Surfactant SDS(20%)	
	10s	136.90°	5%		64.52°	10%		86.89°
								
	30s	172.16°	10%		64.51°	50%		59.64°
	60s	172.36°	15%		94.83°	100%		111.52°

PEDOT: PSS film, the pristine PEDOT:PSS solution is often mixed with polar solvent such as isopropanol (IPA), methanol and ethylene glycol etc. [92], [206], [207]. The PEDOT:PSS used in this work was purchased from Ossila (UK) with 1-1.3 wt.% dispersion in water. Since the PEDOT:PSS solution is water dominated, it is difficult to obtain a continuous film on the hydrophobic surface such as PDMS. In order to convert the hydrophobic surface into hydrophilic, three major reported methods including oxygen plasma exposure, hydrochloric acid treatment and surfactant immersion were investigated [40]. The effects of these methods were analysed through a custom-made contact angle measurement setup. Compared in **Table 4.3**, the oxygen plasma treatment is the most efficient method among the three. The maximum observed contact angle from oxygen plasma exposure was 172.36°. On the other side, the higher concentrated acid and surfactant sodium dodecyl sulfate (SDS) contribute to a larger contact angle. However, the effect is not significant compared to the observed effect from oxygen plasma exposure. After modifying the surface of PDMS, the PEDOT:PSS film can either be deposited through spray-coating or spin-coating method. Similar to the fabrication process of metallic interconnects on the PDMS, the metal stack (Ti-Au: 10 nm-100 nm) was deposited on top of the PEDOT:PSS film as illustrated in **Figure 4.6(b)**. Following this, the photolithography process was carried out to define the pattern. Then the metal stack was wet-etched (Au: 15 s in KI solution; Ti: 5 s in 10% Hydrogen Fluoride (HF)

solution) and PEDOT:PSS film was dry-etched in Reactive Ion Etching (RIE) system (5 minutes in  $O_2$  plasma under 50 sccm, 100W and 50 mTorr). The interconnects were fabricated after removing the protection layer of photoresist in acetone.

#### 4.2.1. PEDOT:PSS Spray-coating

Spray coating of PEDOT:PSS solution on PDMS substrate was developed utilising a fine pressure-driven nozzle with a 0.4 mm inner diameter (NanoNC, Korea) as shown in **Figure 4.6(c)**. The compressed nitrogen ( $N_2$ ) gas was used to drive the spraying of PEDOT:PSS solution. To help the water-dispersed PEDOT:PSS solution to easily coat on PDMS substrate, 5% IPA was mixed with PEDOT:PSS solution. As discussed in the previous section, the contact angle between the PEDOT:PSS solution and the surface of PDMS can be effectively increased through a short period of oxygen plasma (10 seconds) treatment. In

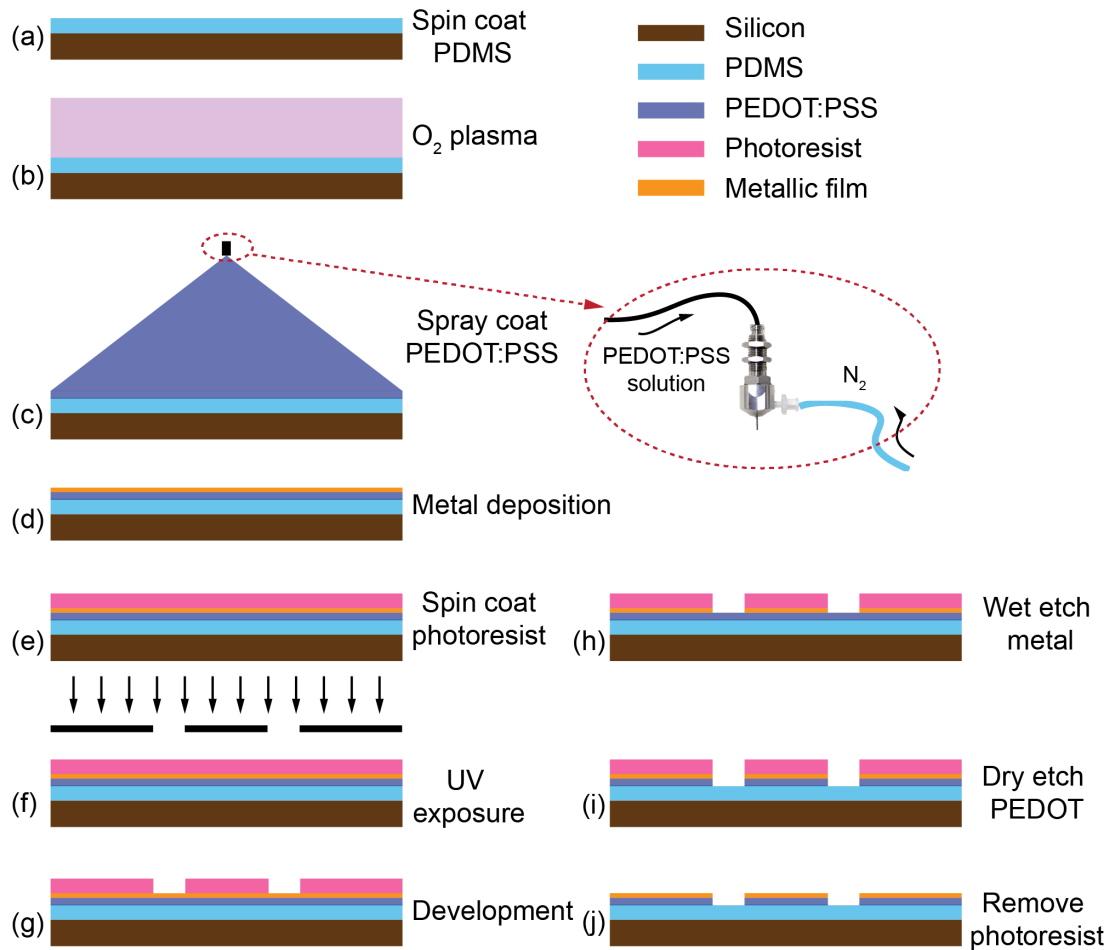


Figure 4.6: Fabrication process flow by incorporating spray-coated PEDOT:PSS between gold conducting film with PDMS substrate.

this way, the PEDOT:PSS can be easier spread over PDMS substrate. Multiple runs of spray-coating can be carried out to adjust the thickness of the PEDOT:PSS film. In order to optimise the spray coating process, an investigation into the relationship between the thickness variation in spray-coated PEDOT:PSS film, number of spray runs and the sheet resistance of the film has been conducted. Each run of spray coating results in a 200-300 nm-thick PEDOT:PSS film based on the measurement taken by the interferometer (Leitz Ergolux). However, the thickness becomes saturated after further increasing of the spray runs, from 3 runs to 5 runs as presented in **Figure 4.7(a)**. However, for all the samples, the deviation in thickness is evident. The sheet resistance of PEDOT:PSS film was measured by a sheet resistance measurement machine (Napson, Japan). The measurement detects a slight drop of sheet resistance by increasing the runs of spray. Considering the measured results of the thickness and the sheet resistance, three runs of PEDOT:PSS spray coating on PDMS substrate was chosen. The resultant PEDOT:PSS film exhibits a low sheet resistance with low standard deviation. An approximate 700 nm-thick PEDOT:PSS film which was deposited on PDMS substrate by spray coating, as shown in **Figure 4.7(b)**. The spray-coated PEDOT:PSS film exhibits a resistivity around  $0.0072 \Omega \cdot \text{m}$ . Following this step, a metal stack (10 nm Ti and 100 nm Au) was deposited by e-beam evaporation. The metal pattern was achieved through photolithography and etching, as discussed in **Figure 4.6(e-j)**.

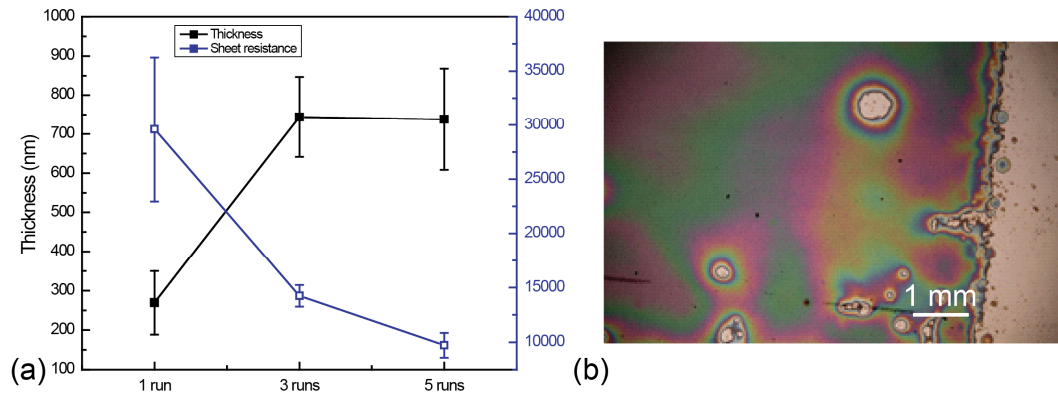


Figure 4.7: (a) Measurement results in sheet resistance and thickness of spray-coated PEDOT:PSS layer and (b) optical image of spray-coated PEDOT:PSS film on PDMS substrate [242].

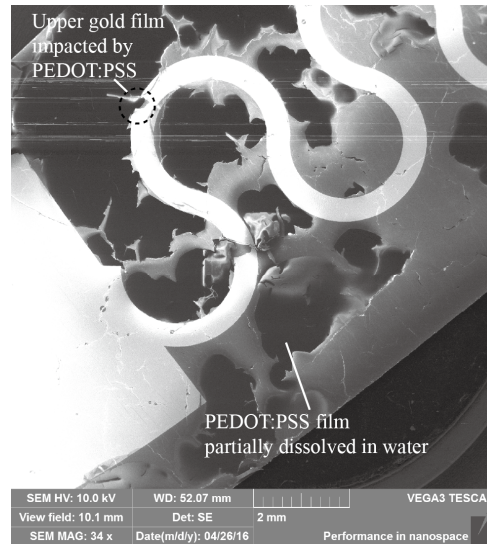


Figure 4.8: SEM image of fabricated interconnects with part of gold film cracked and delaminated due to the peeling of underlying PEDOT:PSS film.

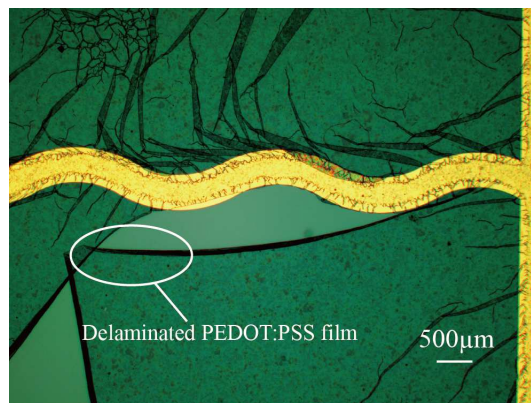


Figure 4.9: Microscopic image of fabricated interconnects with the delamination of PEDOT:PSS film.

Some issues were noticed during the process. As PDMS substrate is sensitive to temperature, the curing process of PEDOT:PSS has to be performed at a lower temperature ( $\sim 70^{\circ}\text{C}$ ), which could degrade the electrical conductivity of the resulting film. Another issue is that the presence of PEDOT:PSS beneath the Ti-Au film, which get affected during wet etching of Ti-Au. This leads to a delamination and dissolution of PEDOT:PSS film afterwards, as shown in **Figure 4.8&4.9**. The delamination of the PEDOT:PSS film will further drag the upper Ti-Au stack layer off from the substrate. One of the method to resolve this issue is to replace the wet etching process of metal with dry etching, which depends on the facility in the clean room. Another method is to restrict the duration of aqueous process.



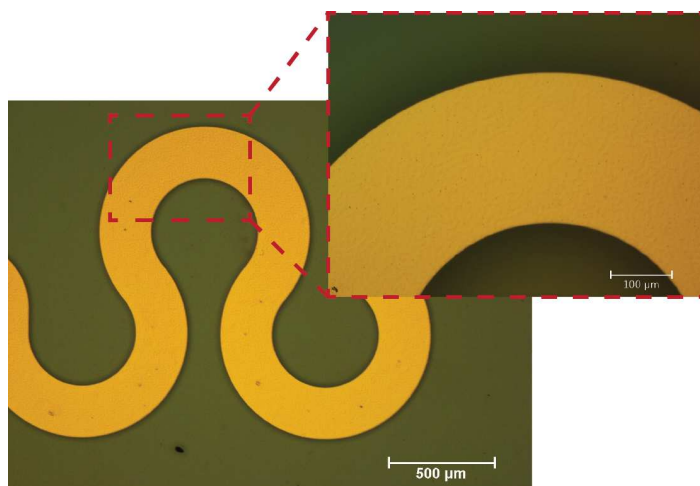


Figure 4.10: Optical microscopic image of fabricated Au-PEDOT:PSS interconnects.

The wet etching process duration can be significantly reduced if the Ti-Au metal stack was replaced with Au metal. In this way, no delamination or dissolution phenomena was observed after wet etching of Au film. The PEDOT:PSS film was then dry-etched in O<sub>2</sub> plasma (50 sccm, 100 W, 50 mTorr) with RIE system. The achieved interconnect is shown in **Figure 4.10** with no delamination of PEDOT:PSS film observed.

#### 4.2.2. PEDOT:PSS Spin-coating

As one of the drawbacks of spray-coating PEDOT:PSS film on PDMS substrate is the non-uniform thickness, the spin-coating technique was developed to overcome this issue. The purchased pristine PEDOT:PSS is dispersed in water, which makes it challenging for directly depositing on the PDMS substrate due to its hydrophobicity. Despite enough oxygen plasma treatment was given to the PDMS substrate, the solution tends to detach from the substrate during spinning. In order to assist the uniform spreading of the PEDOT:PSS solution and enhance the electrical conductivity in the resulting film, three low-boiling-point solutions (IPA, Methanol and DMSO) were mixed with the PEDOT:PSS pristine solution separately. The PDMS substrates were first deposited on the square-shape glass slides with the dimension of 1.5 cm×2 cm. Then the PDMS substrates were exposed to oxygen plasma for 60 seconds at the power of 80 W, as optimised in **Table 4.3**. The PEDOT:PSS solution was prepared through mixing the solvent in different volumetric ratios. Afterwards, the

Table 4.4: Comparison of the optical microscope images of the spin-coated PEDOT:PSS on PDMS and their two-terminal resistance with different ratio of solvents.

	PEDOT:PSS +IPA		PEDOT:PSS + Methanol		PEDOT:PSS + DMSO	
33.3 vol. %		-		-		-
50 vol. %		114.6 k $\Omega$ 116.1 k $\Omega$ 111.9 k $\Omega$		663 k $\Omega$ 672 k $\Omega$ 682 k $\Omega$		3.6 k $\Omega$ 3.8 k $\Omega$ 3.2 k $\Omega$
54.5 vol. %		377 k $\Omega$ 374 k $\Omega$ 392 k $\Omega$		455 k $\Omega$ 442 k $\Omega$ 436 k $\Omega$		1.9 k $\Omega$ 1.8 k $\Omega$ 2.0 k $\Omega$

mixed solution was spun on the PDMS for 30 seconds with a rate of 1000 rpm. Soon after the spinning, samples were heated in the oven for 30 minutes at the temperature of 70°C. The results were inspected through microscope and multimeter. To make a fair comparison, the microscopic images were captured at two diagonal corners from the square substrate. The electrical conductivities of the deposited films were measured at three locations with multimeter. It is noted that the thickness of PEDOT:PSS film varies with different solvent ratio. However, for the PEDOT:PSS solutions with the same amount of solvent, the resultant films were assumed to have the same thickness. In this way, the resistance of the resultant film used by different solvent can be compared. As summarised in **Table 4.4**, the continuous conductive film can be obtained when the mixed solvent is above 50 vol. % in general. In the case of IPA, the extra volume of solvent that was added to the mixture diluted the conductive PEDOT and led to a decrease in the resultant resistance. On the contrary, the solvents such as Methanol and DMSO enhanced the electrical conductivity. This effect can be explained that the extra solvent helps to separate the conductive part of PEDOT with the non-conductive part of PSS. This separation process allows a rearrangement of PEDOT



molecules and gives more pathways for building up a PEDOT conductive network in the film.

The spin-coated PEDOT:PSS film on PDMS substrate was characterised through Transfer Line Measurement (TLM) and electro-mechanical measurement. The samples with different lengths of 10 mm, 20 mm and 30 mm have the same width of 5 mm. The contact electrodes that are composed of a stack metal (Ti-Au) was e-beam evaporated through a shadow mask. Measurements of two-wired resistance with respect to the length was concluded in **Figure 4.11** with a linear fitting. The estimated sheet resistance of PEDOT:PSS film is  $524.4 \pm 94.75 \text{ } \Omega/\square$  and the contact resistance is  $190.645 \pm 59.825 \text{ } \Omega$ . However, the values of fitted curve have a high variation (standard error). This may be due to the unstable contact between the probe and the sample surface. Since the surface of the sample is soft, the metallic probes easily pierced into the film. Another possible explanation is that the conductivity of PEDOT:PSS is anisotropic that the conductivity directional dependent [92]. The interface between PEDOT:PSS and the deposited electrode may vary from sample to sample. The high deviation in resistance measurement may also be attributed from the variated thickness of the film. Confirmed by AFM scanning at the edge of etched PEDOT:PSS film, as indicated in **Figure 4.12**, the thickness of spin-coated PEDOT is around 30 nm.

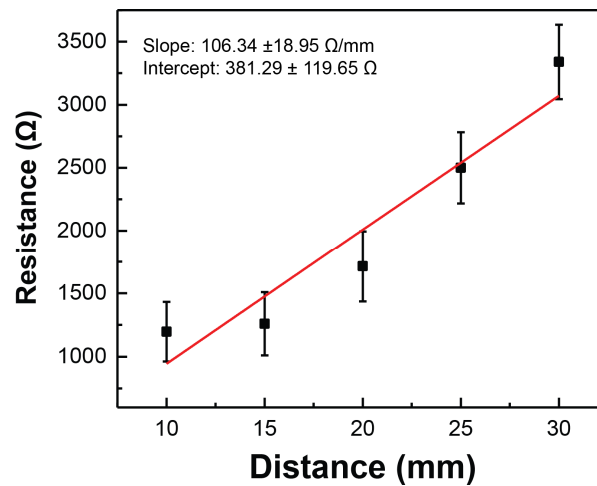


Figure 4.11: TLM measurement for spin-coated PEDOT:PSS film on PDMS.

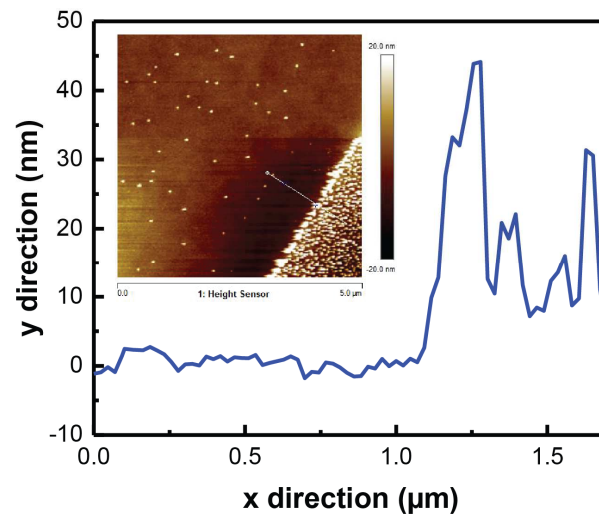


Figure 4.12: AFM scan at the edge of PEDOT:PSS film to estimate the thickness of the film.

In this section, an optimised process to deposit crack-free metal (gold) on PDMS substrate is realised. In addition, two methods including spray coating and spin coating techniques for depositing PEDOT:PSS on PDMS substrate were discussed. The spray coating technique can realise an around 700 nm-thick PEDOT:PSS film on PDMS while the spin coating method results in an around 30 nm-thick PEDOT:PSS film. Afterwards, the stretchable interconnects based on hybrid structure with PEDOT as under-layer and metal (gold) as upper-layer were fabricated. The electro-mechanical response of fabricated interconnects will be discussed in **Chapter 5.3**.

### 4.3 Graphite-conductive polymer composite based interconnects

As explained in the previous section, the electrical behaviour of PEDOT:PSS film can be significantly improved by incorporating the solvent DMSO. In order to further increase the conductivity of the resulting PEDOT:PSS film, the highly conductive graphite powders are introduced to dope PEDOT, in order to obtain a better conductive composite. The graphite powders were purchased from Sigma Aldrich with an average size below 45  $\mu\text{m}$ . Initially the graphite powder was dispersed into DMSO with a ratio of 0.1 g/ml. To help graphite powders disperse homogeneously in the solution, the graphite dispersion was probe sonicated (Ultrasonic disintegrator 500W, Fisherbrand, UK) for 30 seconds and then bath sonicated for 15 minutes. Afterwards, the composite was spun-coated on top of the PDMS substrate. In order to reduce the contact resistance, the contact electrode that is composed of a stack metal (Ti-Au) was deposited through a shadow mask. As shown in **Figure 4.13(a)**, the PDMS deposited with graphite-PEDOT:PSS composite was diced into different lengths (10 mm, 20 mm and 30 mm) and with the same width of 5 mm. The thickness of the composite is  $0.81 \pm 0.35 \mu\text{m}$ , which was measured by surface profilometer (Dektak, Bruker, US). The dispersed graphite powders within PEDOT:PSS film were examined through various studies. The image from the optical microscope (**Figure 4.13(b)**) indicates that the graphite powders are agglomerated. However, with the conductive polymer as matrix, the electrical network between agglomerated graphite can be built. To investigate the chemical doping effect from graphite powder to the PEDOT:PSS film, the Raman spectroscopic measurement was performed with a 532 nm excitation wavelength (Ventus 532 laser system). Symmetric  $C_{\alpha} = C_{\beta}$  stretching vibration consisting of two components, which are

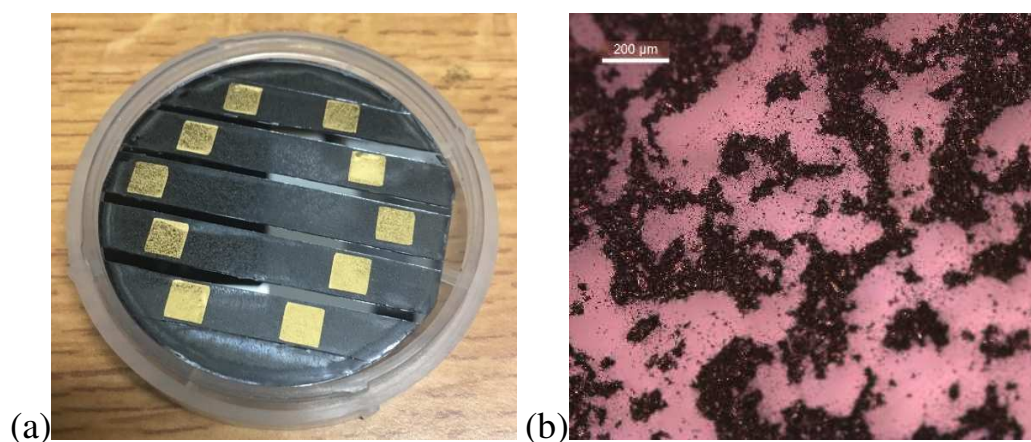


Figure 4.13: (a) Image of Graphite-PEDOT:PSS composite that was spun-coated on 2-inch PDMS substrate and (b) Optical microscopic image of dispersed graphite powder within PEDOT:PSS film.

contributed by the neutral and oxidised structure of polymer [208]. Neutral component at  $1410.27\text{ cm}^{-1}$  in pristine PEDOT:PSS is observed to shift to  $1432.55\text{ cm}^{-1}$ . The oxidised structure is vibrated at around  $1450\text{ cm}^{-1}$  in pristine PEDOT:PSS has been shifted to  $1507.57\text{ cm}^{-1}$ . In the meantime, the G peak at  $1584.77\text{ cm}^{-1}$  and D peak at around  $1360\text{ cm}^{-1}$  from graphite becomes prominent, as indicated from **Figure 4.14(a-b)** [200]. In the meantime, the morphology of thin films was investigated using the AFM measurement. As illustrated in **Figure 4.15(a-b)**, the surface roughness increased due to the doped-graphite powder effect. The powder introduced pothole structure to the surface. The measured depth is around  $8.4\text{ nm}$ . Therefore, the overall roughness is increased from  $2.94\text{ nm}$  to  $5.11\text{ nm}$ .

The electrical characterisation of graphite-PEDOT:PSS composite was performed using IV-characterisation probe station (B1500A, Keysight). The sheet resistance and contact resistance was measured through the TLM method. Compared with un-doped PEDOT:PSS film, the graphite-PEDOT:PSS composite shows more stable results by linear fitting for resistance respecting the variated distance, as recorded in **Figure 4.16**.

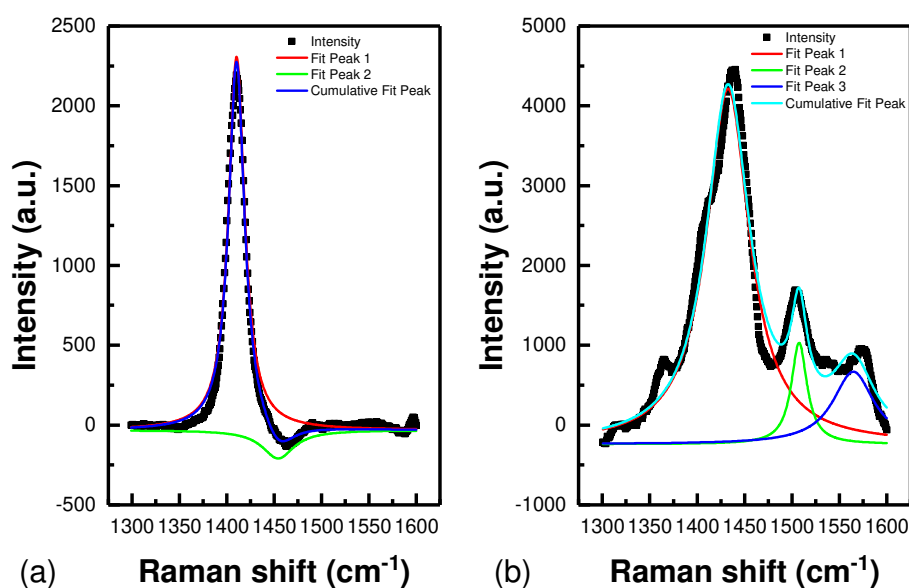


Figure 4.14: (a) Raman spectra of PEDOT:PSS film with Lorentz fitting curve, (b) Raman spectra of Graphite-PEDOT:PSS composite film with Lorentz fitting curve

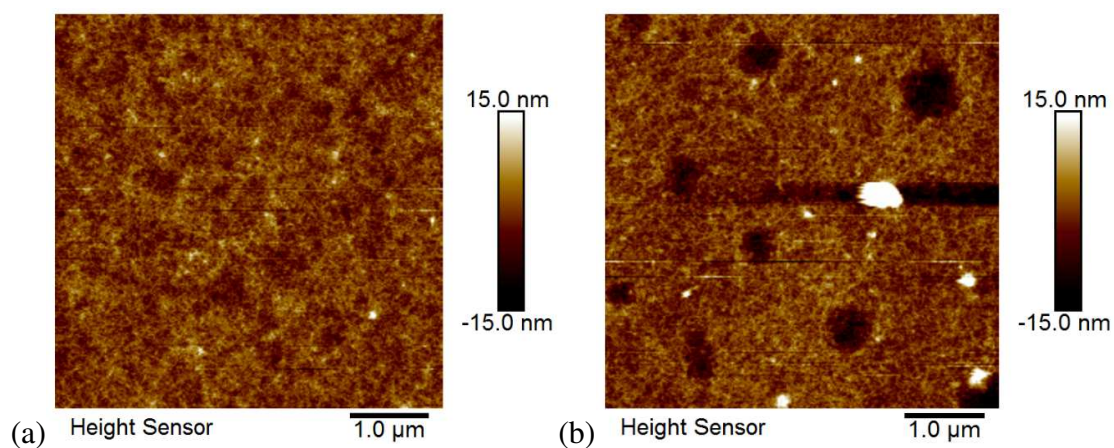


Figure 4.15: (a) AFM images of PEDOT:PSS film on PDMS substrate and (b) AFM images of Graphite-PEDOT:PSS composite film on PDMS substrate.

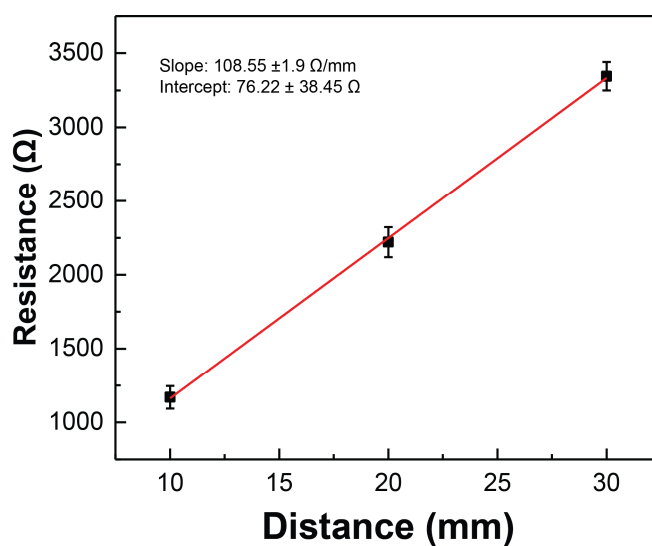


Figure 4.16: Linear curve fitting of the measurement results during TLM measurement.

## 4.4 Metal-Polyimide dual layer transferable interconnects

The previous methods, Au deposited on top of PDMS substrate and Au with PEDOT:PSS film on top of PDMS, both have the same drawback of requiring a releasing step after fabrication. The peeling process gives a large strain on both Au and PEDOT:PSS film which develops some cracks in the film even before the film is under test. Hence, it is necessary to investigate a feasible process to transfer the patterned interconnects to release-free PDMS substrate. In this method, the Polyimide (PI) film is chosen as a mechanically supportive layer for the transfer printing along with a thin PMMA layer is used as a sacrificial layer for releasing the PI layer.

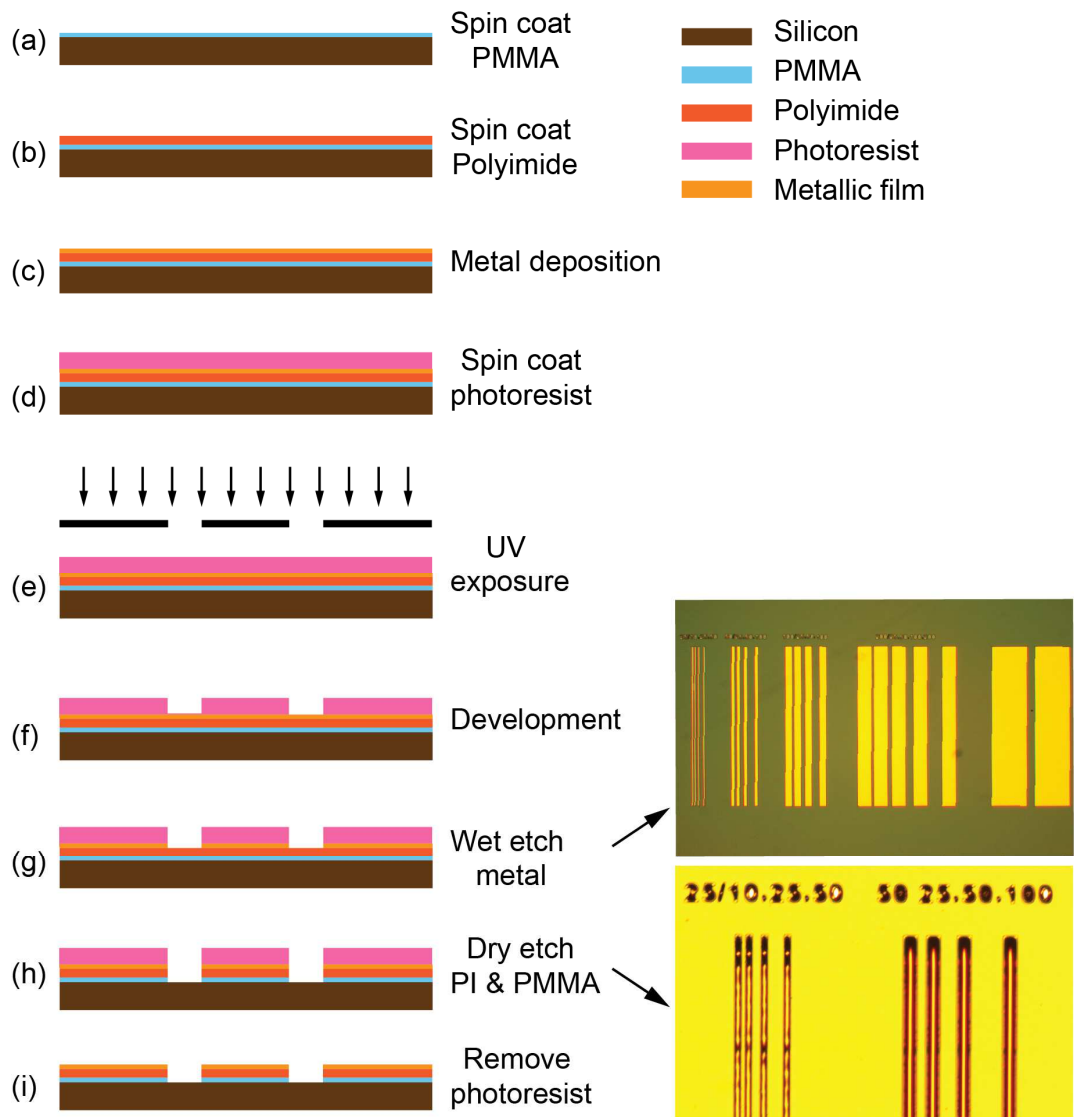


Figure 4.17: Fabrication process flow which adopts polyimide as transfer support layer.



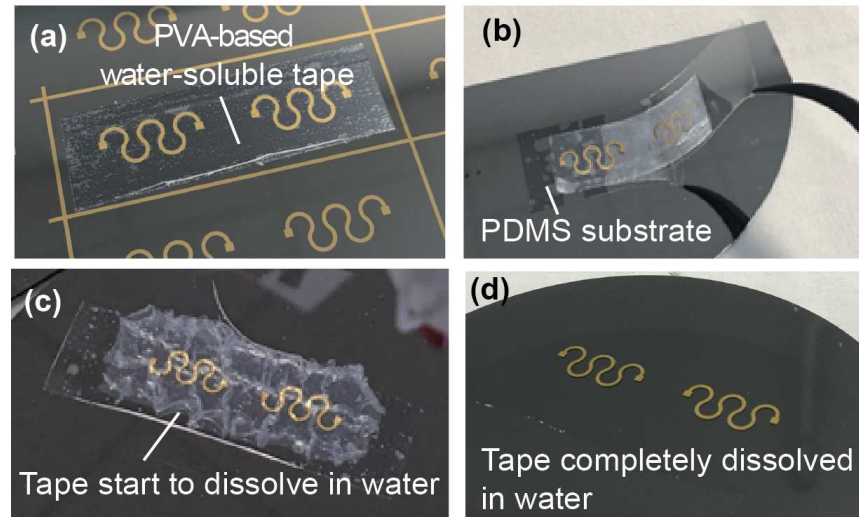


Figure 4.18: Transfer patterned interconnect from Si wafer to PDMS substrate with the assistance of water-soluble tape.

The detailed fabrication process of stretchable interconnects is illustrated in **Figure 4.17**. Initially, a polyimide (PI) (DuPont) layer was spun on 100 nm-thick poly(methyl methacrylate) (PMMA) (Sigma Aldrich) coated silicon wafer at the spin rate of 3000 rpm for 30s. Curing for three hours at 200°C in nitrogen ambient resulted in the PI film with 7  $\mu\text{m}$  thickness, which was confirmed by interferometer (Leitz Ergolux) measurement. Then, a stack of Cr/Au (5/150 nm) metal film stack was e-beam evaporated and this was followed by a mild (15 seconds at 200W) oxygen plasma treatment on PI film. In the next step, a 10- $\mu\text{m}$ -thick positive photoresist (AZ 4562) was used with a bright field mask. During UV exposure and development processes, the designed pattern protects the metal stack from wet etching, where Au was etched in KI solution for 30s and Cr was etched in a mixture solution of perchloric acid ( $\text{HClO}_4$ ) and ceric ammonium nitrate  $(\text{NH}_4)_2[\text{Ce}(\text{NO}_3)_6]$  (MicroChemicals) for 5 seconds. The PI film was dry-etched in the  $\text{O}_2$  plasma through the RIE system (30 minutes at 100 W, 50 sccm, 50 mTorr). The finest structure tested is the electrode with a 25  $\mu\text{m}$ -width with 10  $\mu\text{m}$ -space as shown in **Figure 4.17**. The optical microscopic images compare the test structures for determining fabrication's resolution before and after the dry-etching of the PI film. The interconnects fabricated on silicon wafer were then transferred to PDMS substrate by using water-soluble tape (3M, US), as shown in **Figure 4.18**. The tape dissolved in water within 5 minutes and removed residues after 3 hours. The PDMS substrate (180  $\mu\text{m}$  thick) was obtained separately by spin coating a 10:1 (base polymer: crosslink) PDMS solution on silanised silicon wafer at 300 rpm for 60 seconds and curing in the oven for 2 hours at 90°C.

## Summary

This chapter described the fabrication process of stretchable interconnects based on different conductive materials. In this thesis, the elastomeric polymer PDMS was used as substrate for all kinds of the interconnects. **Table 4.5** compared the materials used for the interconnects with respect to their fabrication process technologies, the process complexity, scalability and reproducibility. Metallic thin film, such as Au, Ti-Au and Cr-Au as the conventional conductors for traditional electronic devices, has been widely exploited. The optimised fabrication process was developed to deposit the metallic thin film on soft substrates. The processes are based on microfabrication technology. Hence, these processes show the advantages of high resolution (up to 5  $\mu\text{m}$ ), scalability and reproducibility. Solution processed organic polymers like PEDOT:PSS have been developed for stretchable interconnects through spray coating as discussed in **Section 4.2.1**. This method exhibits a non-uniform thickness of the resulting PEDOT:PSS film. To overcome this drawback, the spin coating process was developed for PEDOT:PSS solution on PDMS substrate. In addition, an additional metallic layer was designed to deposit on the PEDOT:PSS film to form a hybrid conductive film. This method ensures that the chemical and water sensitive PEDOT film is protected by the addition of metal through the following photolithography and etching process steps. On the other hand, the pattern process for graphite-PEDOT:PSS composite is still under development. The composite film can be acquired through spin-coating and dicing manually. In this way, the resolution of fabricated interconnects is poor compared with the microfabrication process. To further increase the resolution and scalability for fabricating composite based interconnects, the screen printing process is under development. Interconnects based on metal-polyimide dual layer can be fabricated in a similar method as metallic thin film interconnects. In addition to the wet etch process step to the pattern metal layer, the polyimide is required to be dry-etched in oxygen plasma environment. Afterwards, the interconnects have to be transferred from a carrier wafer to the PDMS substrate, which brings more complexity into the fabrication process. However, this method reveals a high resolution, high scalability and high reproducibility process that can be concluded as the most reliable process among all the processes in **Table 4.5**.



Table 4.5: Comparison between each fabrication process for different materials to realise stretchable interconnects.

<b>Material</b>	<b>Process</b>	<b>Process Complexity</b>	<b>Scalability</b>	<b>Resolution</b>	<b>Reproducibility</b>
<b>Metal (Au)</b>	E-beam evaporation	Complex (high vacuum, high voltage)  Number of process steps: >6	High (Pattern through photolithography)	~ $\mu\text{m}$	High
<b>PEDOT: PSS</b>	Spray coat	Moderate (nozzle, control system required)  Number of process steps: >2	Poor	NA	Poor (thickness deviation)
	Spin coat	Straightforward  Number of process steps: >2	Poor	NA	Moderate
<b>Au-PEDOT: PSS hybrid film</b>	Spray coat and E-beam evaporation	Complex  Number of process steps: >10	High (Pattern through photolithography)	~ $\mu\text{m}$	Moderate
	Spin coat and E-beam evaporation	Complex  Number of process steps: >10	High (Pattern through photolithography)	~ $\mu\text{m}$	Moderate
<b>Graphite-PEDOT:</b>	Probe sonication	Moderate	Poor	~mm	High

<b>PSS composite</b>	and spin coat	Number of process steps: >2			
<b>Au-Polyimide dual layer</b>	Spin coat and E beam evaporation	Complex  Number of process steps: >12	High	~ $\mu\text{m}$	High

## Chapter 5 Characterisation of stretchable interconnects

This chapter describes the in-house developed experimental setup for characterising the stretchable interconnects. The setup utilised two stepper motors with high precision movement and the electrical measurement machine. Motor and electrical measurement systems have to be synchronised for a simultaneous movement and measurement in parallel with adjusted speed (data recording/motor moving) to collect adequate data points. The electro-mechanical results from fabricated interconnects described in **Chapter 4** will be further elaborated in this chapter.

### 5.1 Characterisation setup

The custom-developed uniaxial stretching setup was developed for stretchable interconnects characterisation. A pair of stepper motors (Micronix, U.S) can stretch the interconnects from two sides simultaneously. In the meanwhile, the electrical measurement tools including a Multimeter (34461A, Agilent, U.S) and a LCR meter (E4980AL, Keysight, U.S) will start to record the resistance/inductance of the interconnects. In addition, the high precision microscope can help to observe and record the *in-situ* response of interconnects under tension. All of the different parts from setup are controlled by the Labview programme. **Figure 5.1** illustrates the flowchart of the Labview programme that was

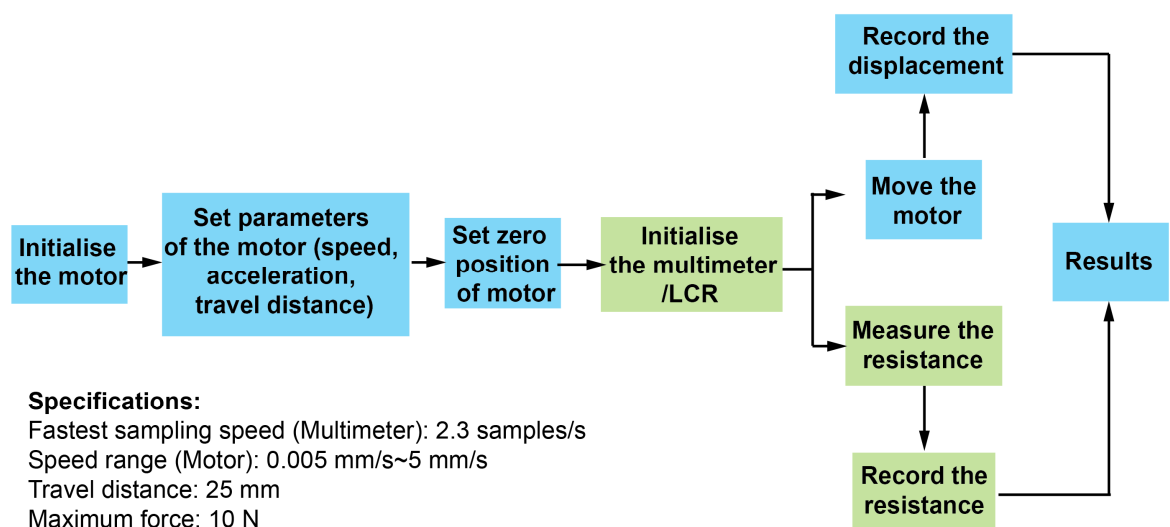


Figure 5.1: Flowchart of Labview programme to synchronise the stepper motor and electrical measurement machines (Multimeter/LCR meter).

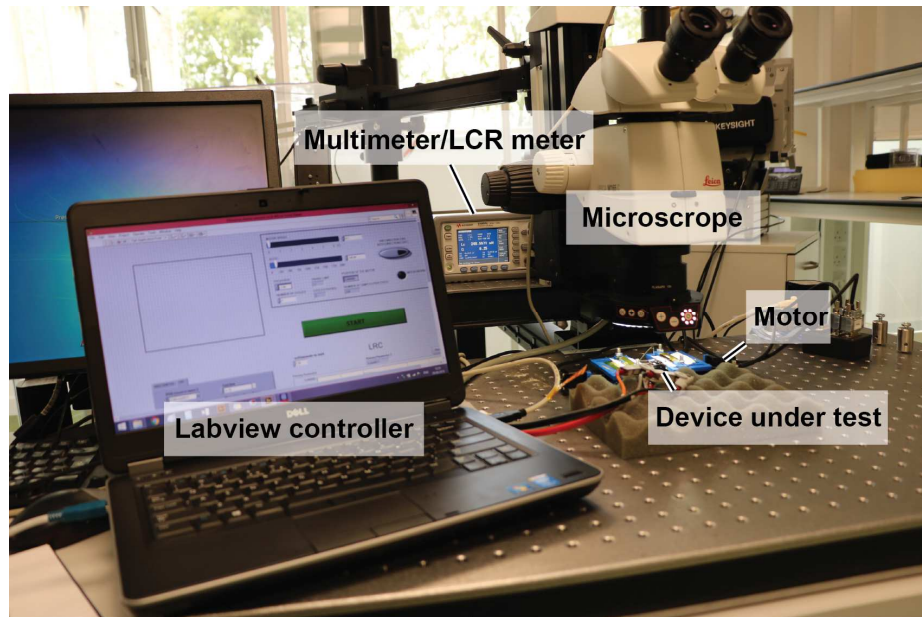


Figure 5.2: Electro-mechanical measurement setup for stretchable interconnects.

developed to synchronise the stepper motors and electrical measurement tools. The motors were first initialised with set parameters, such as speed, acceleration and travel distance. Then, the motor is set with a zero position. After the multimeter is initialised, the motor starts to move while the multimeter starts to measure the resistance of interconnects. The total displacement was set as initial input parameter. As the motor is moving with a constant speed, the location where interconnects fail can be calculated through the point where the measurement signal is discontinued. The operating programme also has the option of cyclic stretching and single-time stretching. The maximum force that the motor can withstand is 10 N and its speed is between 0.005 mm/s and 5 mm/s. The fastest sampling rate of multimeter is  $2.3 \text{ s}^{-1}$ . Hence, the motor's speed for characterising interconnects is chosen between 0.1 mm/s and 0.5 mm/s to ensure sufficient data points. The developed uniaxial stretching setup system is shown in **Figure 5.2**.

## 5.2 Metallic thin film interconnects

Metallic thin film deposited and patterned on PDMS substrate as stretchable interconnects are measured with a custom-developed stretching setup, as described in **Section 5.1**. To investigate the electro-mechanical response of the metallic thin film interconnects, strips of 100-nm-thick gold deposited on PDMS substrate with the dimensions of 10 mm width and 50 mm long are tested, as shown in **Figure 5.3(a)**. Under the stretching,

significant cracks can be observed through a microscope (**Figure 5.3(b-c)**). The direction of cracks is perpendicular to the transverse stretching direction. The cracks are generated immediately at the fixation area when the stretching movement starts, then the cracks spread to the complete film and the cracks becomes wider, as compared in **Figure 5.3(b-c)**). The resistance variation is calculated as  $\left(\frac{\Delta R}{R_0}\right) * 100\%$ . The ultimate strain that the gold film can remain electrical conductive varies, as illustrated in **Figure 5.3(d)**. Three samples of Au-PDMS strips with identical dimension were tested. The maximum strain that the gold film can withstand is 7.8%. At the small strain range of stretching, the gold film can remain electrically conductive because the film is not completely discontinued by cracks. However, with the increase of strain, the resistance variation of gold film can reach as high as 4000%. This is due to the dramatic increase of crack density in the gold film and finally leads to a complete break of gold film.

The electro-mechanical response from serpentine-shaped gold interconnects are shown in **Figure 5.4**. The results show that the different geometry designs are not improving the interconnects' stretchability. All the designs of interconnects cannot withstand a strain above 1%. Analysed from the images of tested samples as presented in **Figure 5.5**, minor cracks are generated even at an early stage of stretching. Compared with the gold strip with 10 mm width, the patterned gold interconnects has 500  $\mu\text{m}$  width. Hence, the electrical path is easily disconnected with minor cracks at low strain range. The results shown in Figure 5.4 is not following the simulation results from Chapter 3. This is due to the different mechanism in

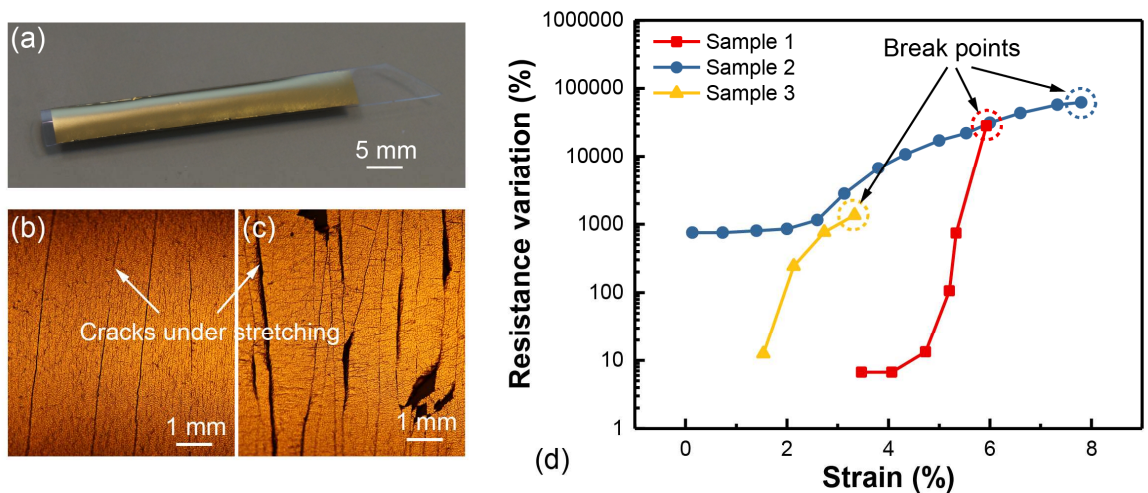


Figure 5.3: (a) Photograph shows the strip of PDMS deposited with gold thin film, (b) microscopic image of gold thin film at the beginning of stretching (c) microscopic image of gold thin film while breaking and (d) resistance variation of gold film under stretching.

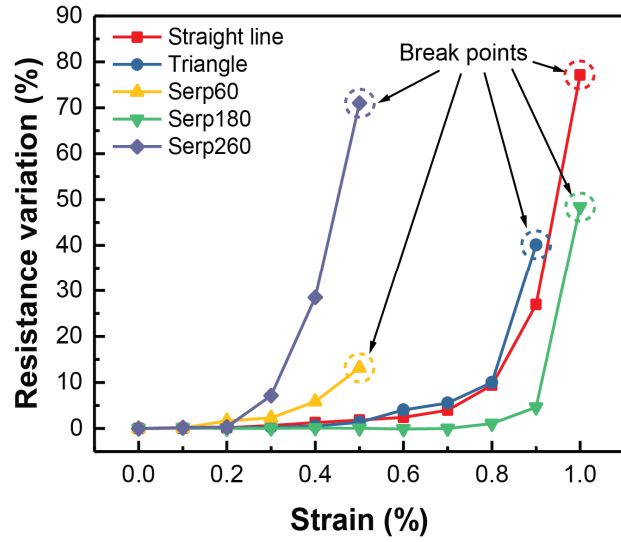


Figure 5.4: Resistance variation of patterned gold interconnects while stretched to failure.

resistance's variation in two cases. In the case of Au-PDMS, the resistance's variation of interconnects is attributed from the cracks' density. However, in the simulation, the variation of resistance is due to the conductor's deformation. Conductor cracks easily even at small deformation, but this cannot be reflected through FEM simulation.

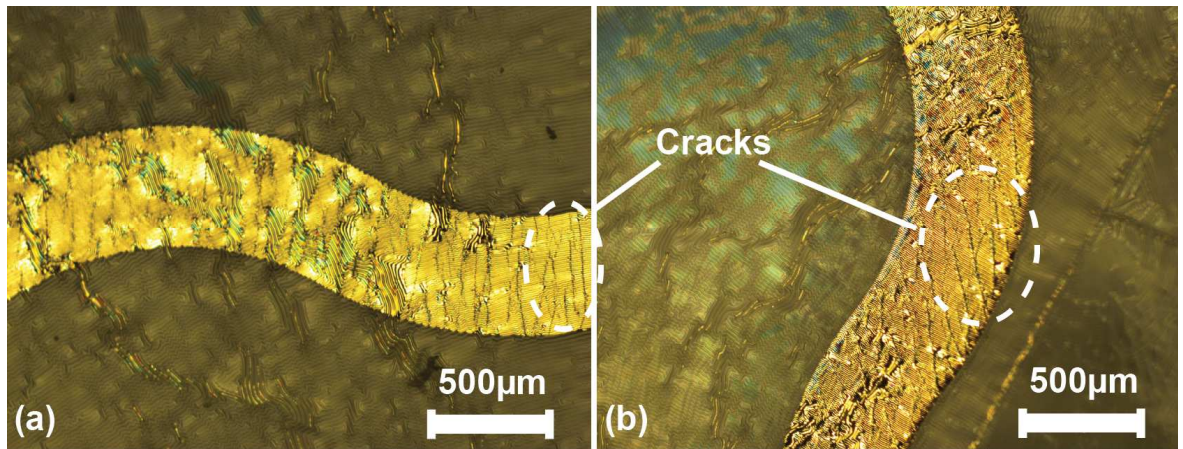


Figure 5.5: Microscopic images of patterned Au interconnects (a) serp60 (b) serp260 on PDMS after stretching test.

### 5.3 Metal-conductive polymer hybrid film interconnects

The gold-PEDOT:PSS hybrid film was first investigated to identify its sheet and contact resistance as they are the fundamental parameters in electrical performance. The Transfer-Line Measurement (TLM) test structure was fabricated in order to measure these parameters. As depicted in **Figure 5.6(a)**, the total resistance between two measurement points is the sum of two times of contact resistance and sheet resistance multiplied by the conductor's width. The trend of the resistance with respect to the distance intervals can be linearly fitted. The slope of the fitted line represents the division between sheet resistance and width of conductor and intercept equals to the value of twice of the contact resistance.

The TLM measurement results concluded in **Figure 5.6(b)** indicate that the sheet resistance of pure gold film is only around 30% of Au-PEDOT:PSS hybrid film. Also, the contact resistance of pure gold film is lower. These results are not aligned with the fact that two conductive layers (gold and PEDOT:PSS) in parallel results in a lower resistance compared to either of the individual layers, as illustrated in **Figure 4.6**. One possible explanation is the incompatibility of the gold etching solution with PEDOT:PSS film. The underlying PEDOT:PSS film is sensitive to water which the gold etching solution contains. When the underlying PEDOT:PSS film starts to degrade, it turns to be softer, decomposing and delaminating from PDMS. This provides pathways for the gold film to also crack and delaminate. Another possibility is due to the unevenness of the wafer after PEDOT:PSS was spray-coated. The uneven wafer results in the next layer of spin-coated photoresist to be

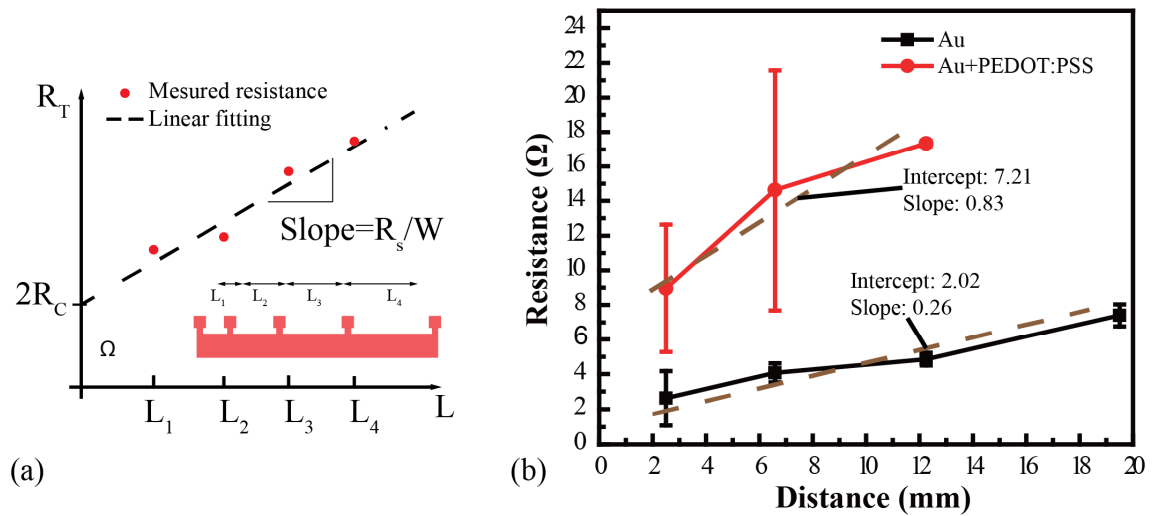


Figure 5.6: (a) Schematic diagram of TLM measurement and (b) the comparison of TLM results between gold and gold-PEDOT:PSS hybrid film on PDMS substrate.



uneven throughout the wafer as well. This leads to an insufficient protection on the gold film for wet etching, which is affected by the etching solution and influences the resulting sheet resistance. The inhomogeneous thickness of PEDOT:PSS film can also contribute to the large deviation in resistance in **Figure 5.6(b)**.

Although TLM measurement results do not show significant improvements in lowering the hybrid film's sheet resistance, the gold-PEDOT:PSS hybrid film exhibits promising results in terms of electro-mechanical performance. The electrical response shown in **Figure 5.7(d)** indicates that the interconnects with “Serp60” design can withstand up to 60% strain. Compared with the pure gold interconnects, the stretchability of the gold-PEDOT:PSS hybrid film has increased more than 40 times, as summarised in **Table 5.1**. With further analysis in combination with hybrid film morphologic images recorded by microscope (**Figure 5.7(a-c)**), the electrical behaviour curve can be separated into three regions. In strain region A (0-2.5%), the increased density of cracks in the Au film is the primary reason for the change in resistivity. This variation in resistivity is significantly lower than the interconnects without PEDOT:PSS because the underlying PEDOT:PSS film has not yet started to crack. In the following strain region B (~10%), as the cracks on the gold film become wider, the gold film separates into “islands” but is still connected by the

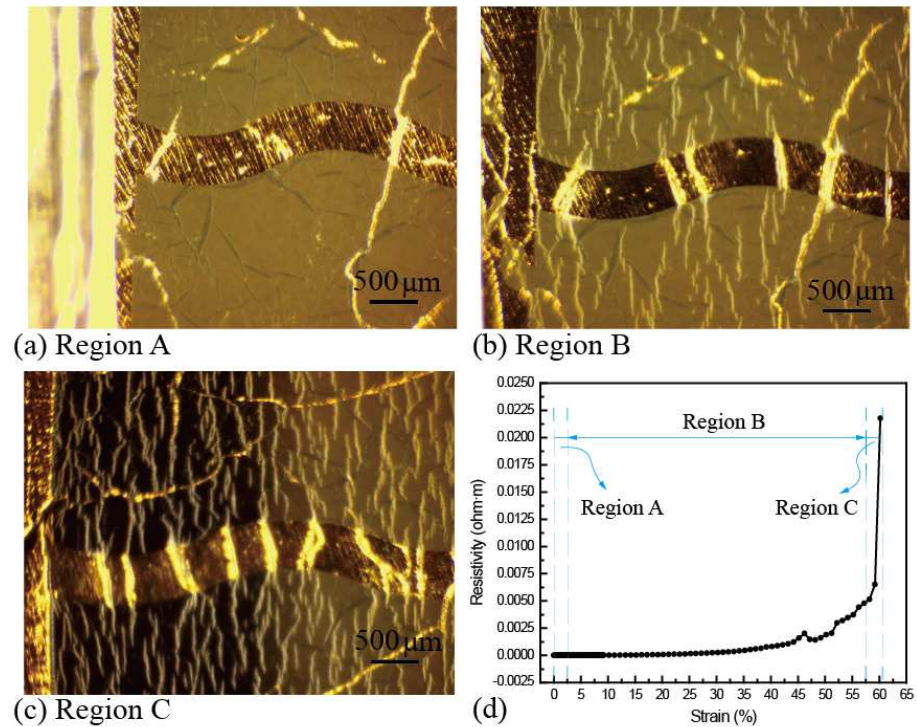


Figure 5.7: (a-c) Optical images on the trend in crack propagation with an increasing of external strain, (d) the electrical response respects to the regions with different crack density [242].



PEDOT:PSS film beneath to remain electrical continuity. In this region, the PEDOT:PSS film with a moderate electrical conductivity dominates the hybrid film's conductivity, hence the hybrid film's resistivity is 10-50 times higher compared to the film's resistivity in region A. When the PEDOT:PSS film starts to break (region C), the resistivity rises to around  $0.022 \Omega \cdot \text{m}$ .

Table 5.1: Comparison of the stretchability and resistivity variation between three different designs of interconnects with/without PEDOT:PSS underlying layer [209].

Design	Material	Stretchability	$\Delta\rho/\rho_0$ @ 1% applied strain	$\Delta\rho/\rho_0$ @ 10% applied strain
<b>Straight line</b>	Au film	1%	77.2%	-
	Au+PEDOT:PSS hybrid-film	1.2%	33.6%	-
<b>Serpentine (60°)</b>	Au film	0.5%	13.2%	-
	Au+PEDOT:PSS hybrid-film	60.2%	2.1%	43.91
<b>Serpentine (180°)</b>	Au film	1.5%	48.4%	-
	Au+PEDOT:PSS hybrid-film	71.9%	0.9%	64.93

As discussed in **Chapter 3**, the serpentine-shaped design in interconnect routings not only re-distributes the concentrated stress while the interconnect is under deformation, but also provides longer overall length which allows more freedom for movements. For example, the serpentine-shaped design with the arc curvature of  $180^\circ$  has a stretchability up to 71.9%, compared to the straight-line design that only has a limited stretchability of 1.2%. **Figure 5.8** compared three interconnect designs with arc curvatures of  $60^\circ$  and  $180^\circ$  while being stretched until they fail (or failure strain). As expected, larger arc curvature gives longer arc length. Thus, it can withstand higher deformation and provide higher stretchability.

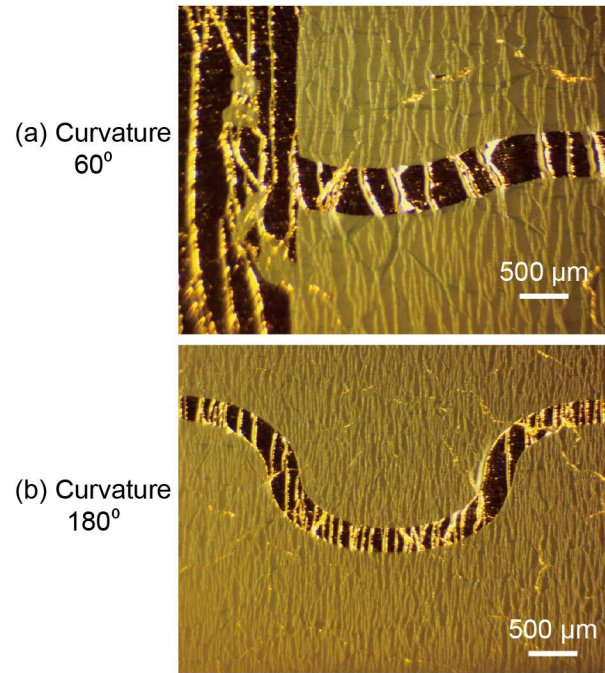


Figure 5.8: Microscopic images of interconnects under failure strain with different design in curvature (a) 60° (b) 180° [242].

## 5.4 Graphite-conductive polymer composite based interconnects

The sheet resistance of graphite-PEDOT:PSS composite was tested with three different lengths (10 mm, 20 mm and 30 mm). The width of the test structures are identical to be 5 mm. As shown in **Figure 5.9(a)**, the sheet resistance of graphite-PEDOT:PSS composite exhibits to be  $542.75 \pm 9.5 \Omega/\square$  and the contact resistance is around  $38.11 \pm 19.23 \Omega$ . Compared with the gold-PEDOT:PSS hybrid film, the composite shows a much higher sheet resistance.

However, the stretchability of composite can reach up to 85%, as presented in **Figure 5.9(b)**. For all the three samples, the resistance increases in the order of 2-3 along with the increasing strain. Samples no. 2 and no. 3 fail at around 50%, while sample no. 1 fails at 85%. The inconsistency for each sample may be due to the varying thickness of the resultant composite film, which is attributed to the agglomeration of graphite fillers.

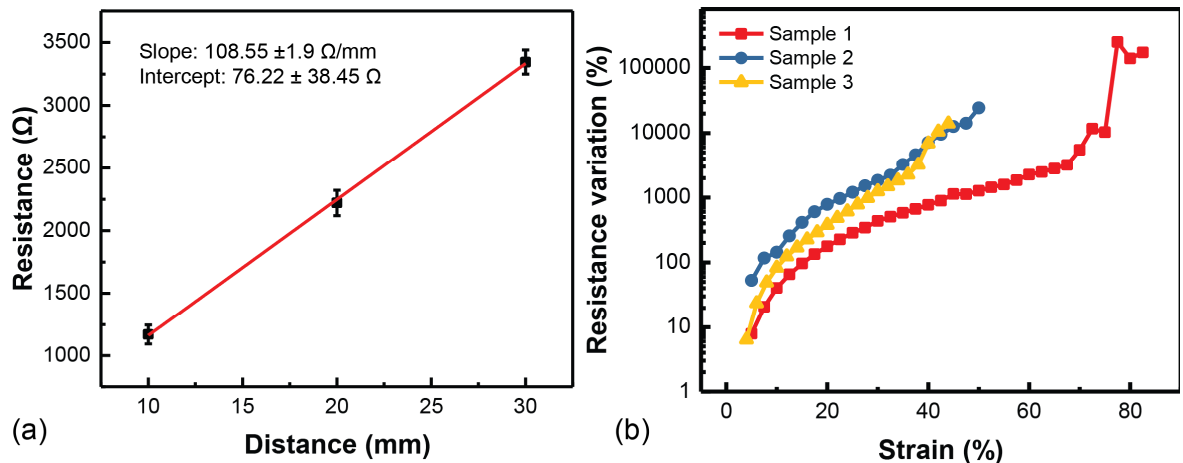


Figure 5.9: (a) Linear curve fitting of the measurement results during TLM measurement, (b) Recorded resistance of Graphite-PEDOT:PSS composite film under external strain.

## 5.5 Metal-Polyimide dual layer transferrable interconnects

### DC range characterisation

The electro-mechanical response from the Au-PI based stretchable interconnects can be reflected through their changes in resistance. Two-terminal resistance of interconnects was monitored through multimeter under stretching. The first study aims to investigate the maximum strain (stretchability) that the interconnects can withstand with respect to different designs. **Figure 5.10(a)** provides a general comparison between different designs of interconnects' trend in resistance variation under stretching. To further investigate the morphological changes while the interconnects are under stretching, the *in-situ* microscopic images were recorded and shown in **Figure 5.11**. For the "straight-line" shaped

interconnects, the resistance linearly increases with the increasing strain applied. The maximum strain of such design is limited to around 5.7%. Compared with pure metal (Au) on PDMS substrate as interconnects with less than 1% stretchability (section 5.2), the dual-layered Au-PI exhibits a higher stretchability. This is due to the intrinsic stretchability of the PI. The maximum elongation ratio of bulk PI sheet, as suggested by datasheet, is around 10% [210]. After patterning the PI sheet with 500  $\mu\text{m}$  straight line, the stretchability of PI is

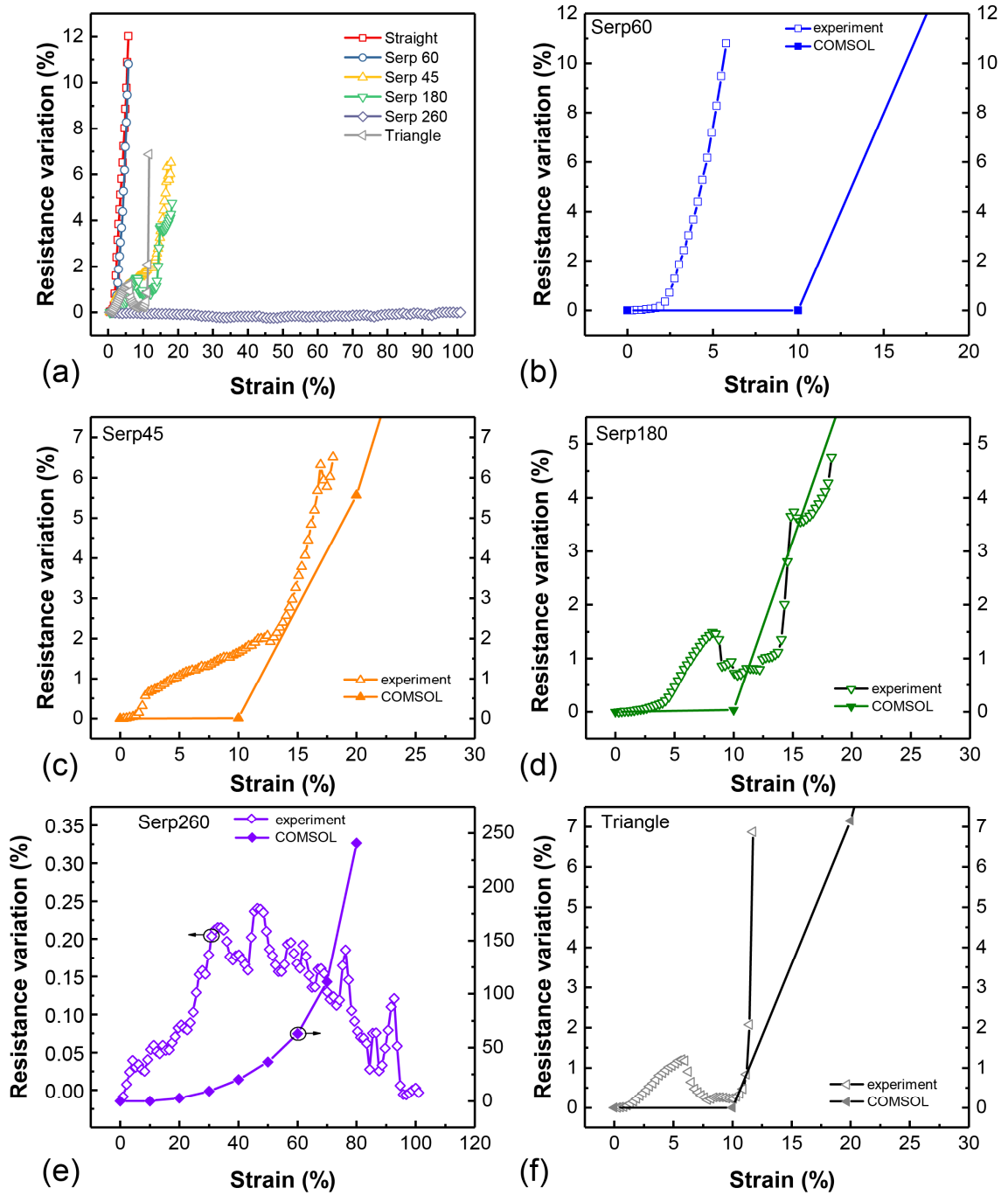


Figure 5.10: (a) Resistance variation of stretchable interconnects with different designs and (b-f) the comparison between the experimental results and COMSOL simulation results.

limited. The dramatic variation in interconnects' resistance results from the deformation of Au film (at the early level of strain) and the increased density of cracks within the Au film (at nearly broken level). With a moderate curved design (Serp 60), the maximum strain of interconnects does not have significant improvement. The experimentally observed resistance variation is lower, compared to the COMSOL simulation results. The reason

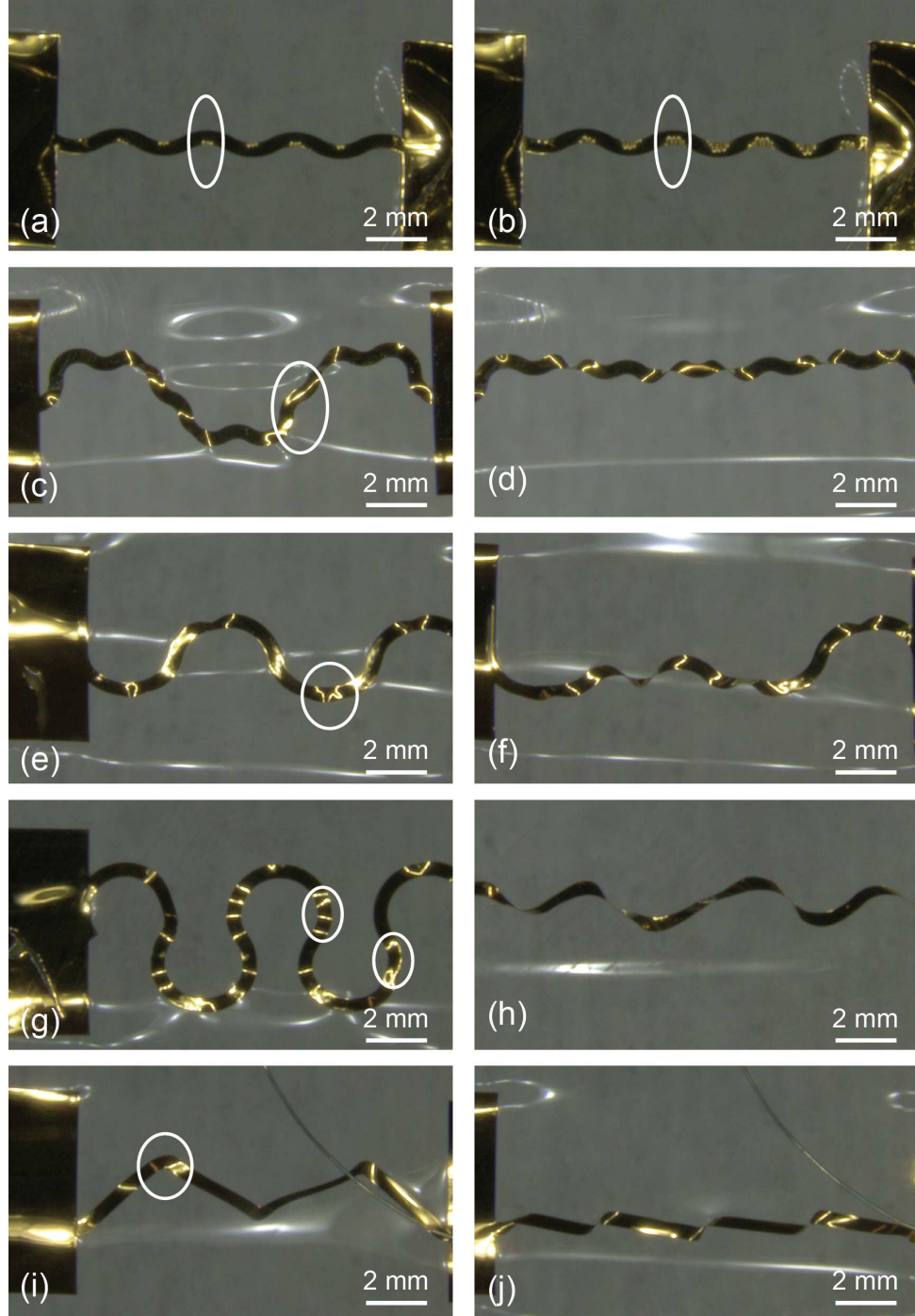


Figure 5.11: Optical images of various interconnect geometries comparing the beginning stage under stretching and nearly breaking stage in stretching: (a-b) serp60; (c-d) serp45; (e-f) serp180; (g-h) serp260 and (i-j) triangle.

behind is the difference in boundary conditions between the experiment and simulation. For example, under the simulation, the interconnects are perfectly bonded to PDMS substrate. In this case, the deformation of conductor under stretching is much higher, which leads to wider variation in resistance. In reality, the bonding between the Au-PI interconnects and PDMS substrate is weaker than the pulling force. As shown in **Figure 5.11(a-b)**, under mild stretching, small wrinkles can be found at the crest area and those wrinkles become more significant when more stretching strain is applied. The wrinkles are formed due to the concentrated stress at crest area in the interconnects. Because the interconnects bond weakly to the PDMS substrate, the stress causes partially delaminating and subsequently leads to wrinkles. Since most of the deformation from stretching strain has transferred to wrinkles generation, which is a general geometrical modification, the local deformations within the conductor, such as cross-section area reduction and length elongation, are not much influenced. For all the interconnect designs, similar distinct trend between experimental and COMSOL simulation results can be noticed. Different degrees in arc curvature from serpentine-shaped interconnect can result in different characteristics under large degrees of stretching, as compared in **Figure 5.11**. Since the substrate is stretching in a transverse direction and shrinking from the bilateral side, the movement gives a twisting momentum to the interconnect and leads to the rolling of curved structures. Thus, the resistance variation along the increasing strain does not follow linear trend as the straight line shaped interconnect. With a closer observation of the resistance's variation of the interconnects, one or two kinks in the trend can be noticed. For example, for the design "Serp 45", the resistance first increases as the strain increases due to the deformation of the Au film as shown in **Figure 5.11(c)**. When the strain reaches a threshold value, the interconnect structure starts to delaminate from PDMS substrate, this delamination provides an extra degree of freedom to interconnects which attributes to a slightly reduce in resistance. Hence, a kink in the trend line of resistance's variation can be found. In the case of interconnects with "Serp 260" design, several kinks were recorded. In the design of "Serp260" interconnects, five arcs with high degree in curvature are connected in sequence. During stretching movement, those arcs are under stretching in translational direction and shrinking in lateral direction, which lead them to delaminate from PDMS substrate. However, they are not delaminating simultaneously. Depends on the location of arc, the strain that the arc experiences exhibits different. Each time when an arc section delaminates from the substrate, the variation trend of resistance is disturbed and a kink is observed. While comparing the interconnects between the moderate stretching and nearly breaking stage, it can be noticed that the concentrated stress within the interconnects, which are reflected through wrinkles, are aligned with the

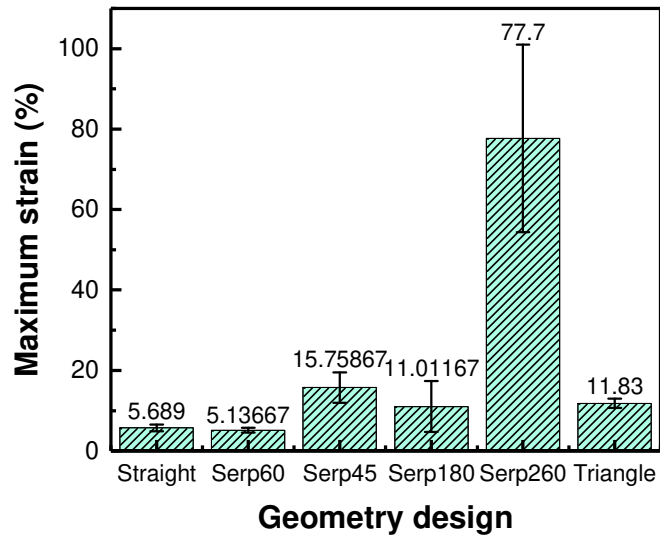


Figure 5.12: Comparison of stretchable interconnects with different geometry design in terms of their maximum strain (stretchability).

location of concentrated Von Mises stress in COMSOL simulation (**Chapter 3**). In addition, it can be observed that with all the interconnect designs, the shapes are rolled and straightened at the final stage before breaking. For each design, at least three samples were tested. The resistance variation trend curves of all the samples are not identical. The average and standard deviation of maximum strain of each interconnect design are summarised in **Figure 5.12**. Amongst all the designs of interconnects, “Serp 260” is observed to be the optimised design due to several reasons: its resistance variation is the lowest and most stable (within 0.3%) and the highest stretchability of this design can attain 101%.

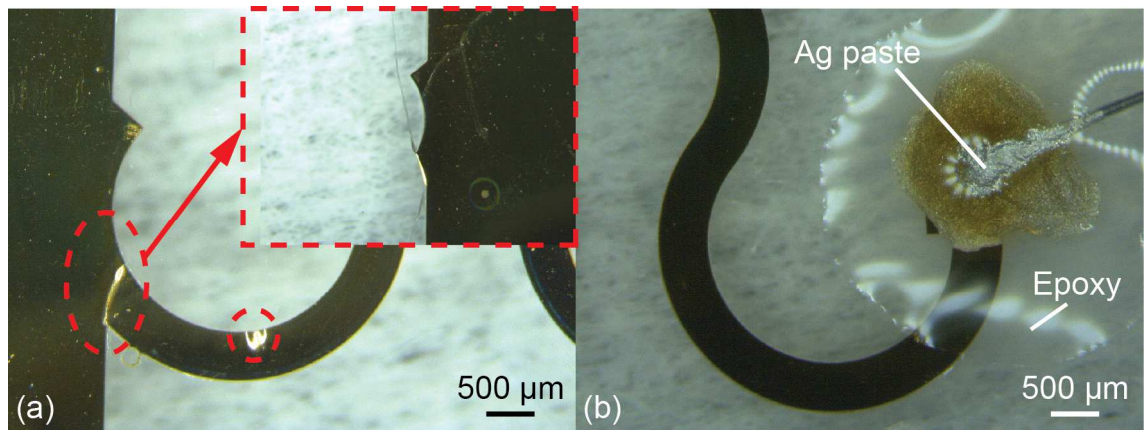


Figure 5.13: Optical microscopic images of connection area of fabricated interconnects including (a) the interconnect made with the pad size of  $7 \times 14 \text{ mm}^2$ , the inset image shows the broken connection when the interconnect failed under stretching, (b) the interconnect bonded with the pad size of  $1 \times 1 \text{ mm}^2$ .



These studies verify that the overall length of curved interconnects decides the stretchability, as discussed in **Chapter 3**. However, the experimental results also indicate that the stretchability of interconnects are much lower than the calculated overall length variation ratio. Aside from the variation of material's intrinsic elastic properties during processing, there are other factors that influence interconnects' stretchability. For example, the connection design of interconnects to the external measuring tool is critical. For all the stretchable interconnects, their connection to the measuring instrument is realised through attaching one thread from the ribbon cable with silver paste to the contact pad from the interconnects. After the silver paste is completely cured, an epoxy layer is deposited and cured as the encapsulation. Two designs of contact pads are implemented in the experiments, as shown in **Figure 5.13**. In the design in **Figure 5.13(a)**, the contact pad has a size of  $7 \times 14 \text{ mm}^2$ , which is not fixed to PDMS substrate with epoxy glue. The second design in **Figure 5.13(b)** has a pad size of  $1 \times 1 \text{ mm}^2$  and it is completely covered with epoxy glue and adhered to PDMS substrate. Repeated tests have revealed that the interconnect with unfixed contact pad exhibits much lower stretchability. The stretchability of **Figure 5.13(a)** design is  $10.36 \pm 2.5\%$  ( $n=4$ ) and the stretchability of **Figure 5.13(b)** design is  $77.7 \pm 23.3\%$  ( $n=3$ ). For all the samples with unfixed electrical connections, the breaking point is at the junction between the contact pad and the interconnect, as pointed out in **Figure 5.13(a)**. However, the interconnects with fixed electrical connections fail at the middle of the interconnects, where the maximum strain is expected, as verified through COMSOL simulation. It is observed that the contact pad with unfixed electrical connection is dragging the curved interconnect under stretching. With an additional factor that the angle between the contact pad and the interconnect is narrow, that sharp angle junction is the most fragile part within the interconnect.

Another factor that influences the interconnects' stretchability is the encapsulation. To investigate the effect of encapsulation, the two "Serp45" shaped interconnects, with one of



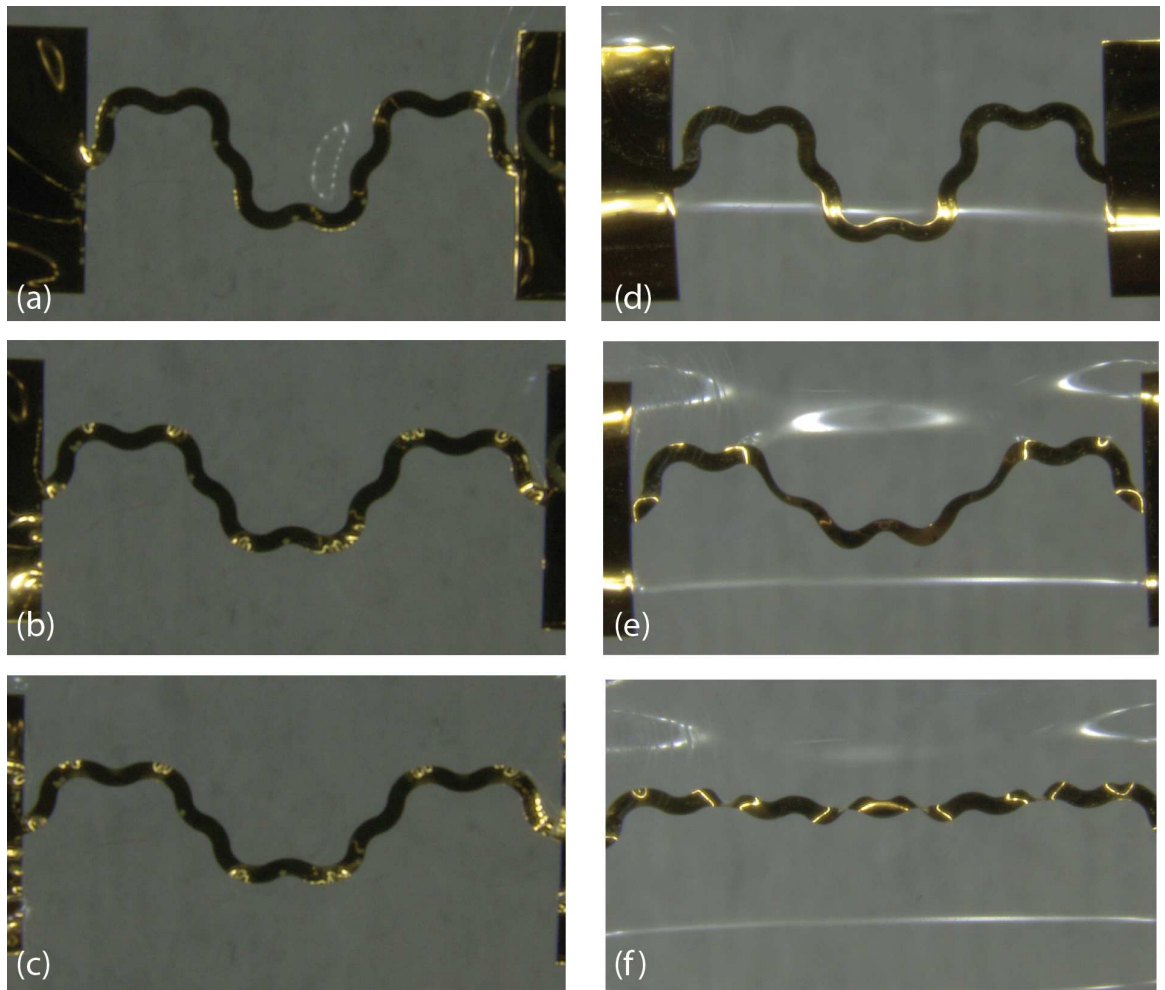


Figure 5.14: Sequence of optical images of (a-c) encapsulated interconnects and (d-f) without encapsulated interconnects under increasing stretching strain.

them encapsulated, are compared. The encapsulation was done through spin-coating another layer of PDMS with the same spinning rate as for substrate. Compared between the interconnects with encapsulation (**Figure 5.14(a-c)**) and without the encapsulation (**Figure 5.14(d-f)**), the additional top layer restricts the interconnects from twisting and rolling under the stretching. The movement of the interconnects is confined within planar direction. Furthermore, the encapsulation attributes to a lower stretchability and higher variation in resistance, as illustrated in **Figure 5.15**. Without the encapsulation, the interconnect is able to reach a stretchability of 23% but reliability in life-cycle is only limited to 2 cycles. After encapsulating the interconnects, the stretchability reduces to 15% but the life-cycle can increase to 7. Similar effect of encapsulation can also be found with the design “Triangle” as illustrated in **Figure 5.16(b)**. However, the effect of encapsulation in design “Serp60” is not significant as shown in **Figure 5.16(a)**. The stretchability of interconnects between the samples with encapsulation and samples without one are similar in design “Serp60”. However, the variation in resistance is higher for the samples with encapsulation. The

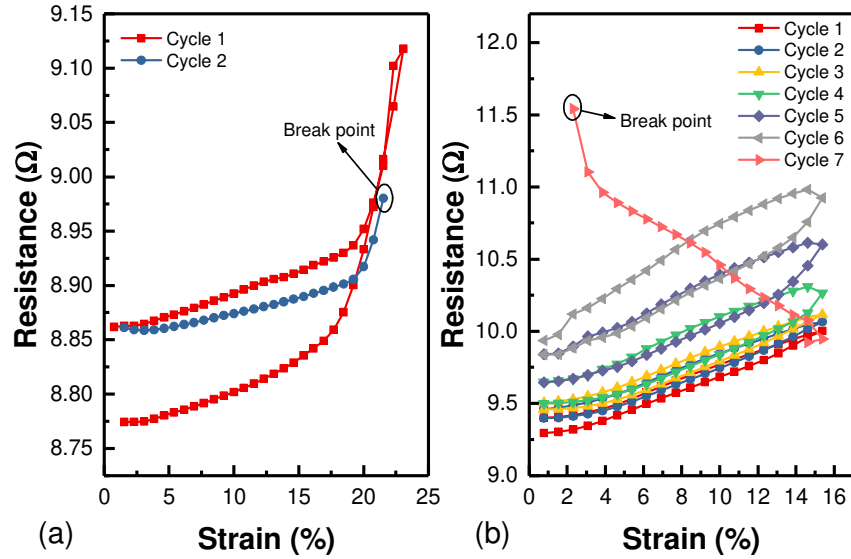


Figure 5.15: Results in cyclic stretching of stretchable interconnects (a) without encapsulation and (b) with encapsulation.

encapsulation can be regarded as an additional constrain to the interconnects and results in a higher strain within the interconnects. Same observation can be found in design “Triangle” as well. Aside from the higher resistance’s variation, the kink in the trend, which is due to the delamination of interconnects from substrate, is not observed in the sample with encapsulation. This comparison can also prove the explanation for the non-monotonic trend in resistance’s variation of interconnects.

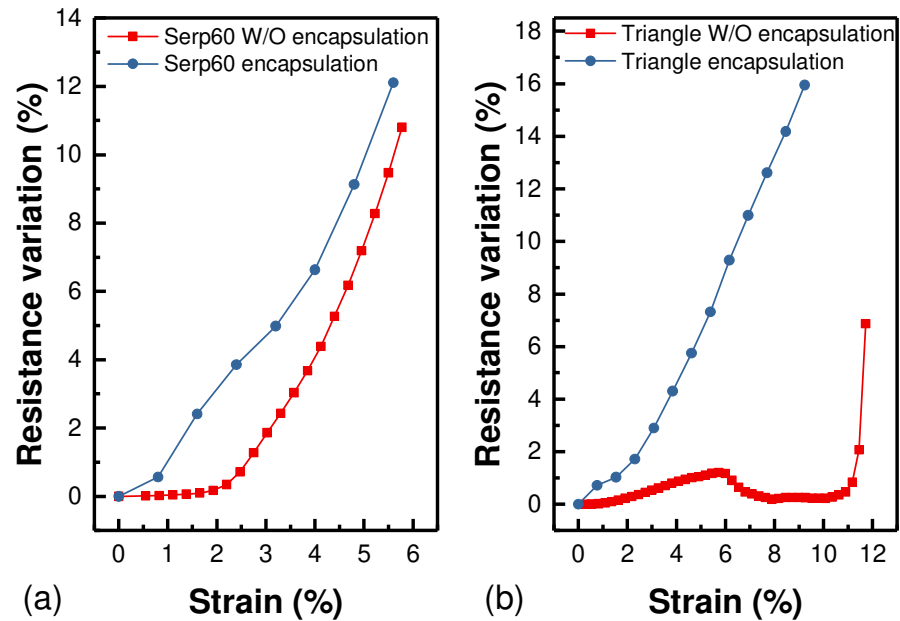


Figure 5.16: Results in (a) inductance variation and (b) Q factor variation and their comparison with simulation results.

## AC range characterisation

The electro-mechanical response from Au-PI based stretchable interconnects were also characterised in AC range through monitoring the change of their inductance and the Q factor. The AC range characterisation for interconnects is essential considering the possibility of integrating with sensors that operate in AC range.

In section 3.4 (**Chapter 3**), the relationship between the inductance and Q factor of a straight conductor with a rectangular cross-section and the strain was derived at low frequency (1 MHz). Compared with the experimental results as shown in **Figure 5.17(a)**, the simulated variation in inductance exhibits a steeper slope with respect to the strain. The reason behind this is due to the intrinsic stretchability of fabricated interconnect, which is reflected from the Poisson's ratio, being lower than theoretical value. In the simulation, the model does not include the PI as under-layer. Regarding Q factor's variation in **Figure 5.17(b)**, the experimental result indicates a much higher reduction than a theoretical one. This phenomenon could be explained by the dramatic increase in resistance from straight line under stretching. The Q factor reflects both the inductance and the resistance of a conductor. When the resistance increases much more than the inductance, the Q factor will drop in consequence. Q factor is an important parameter for inductors as a lower Q factor represents a lower influence is expected from the resistive part in the inductor. This can reflect a lower energy loss and better performance of the inductor.

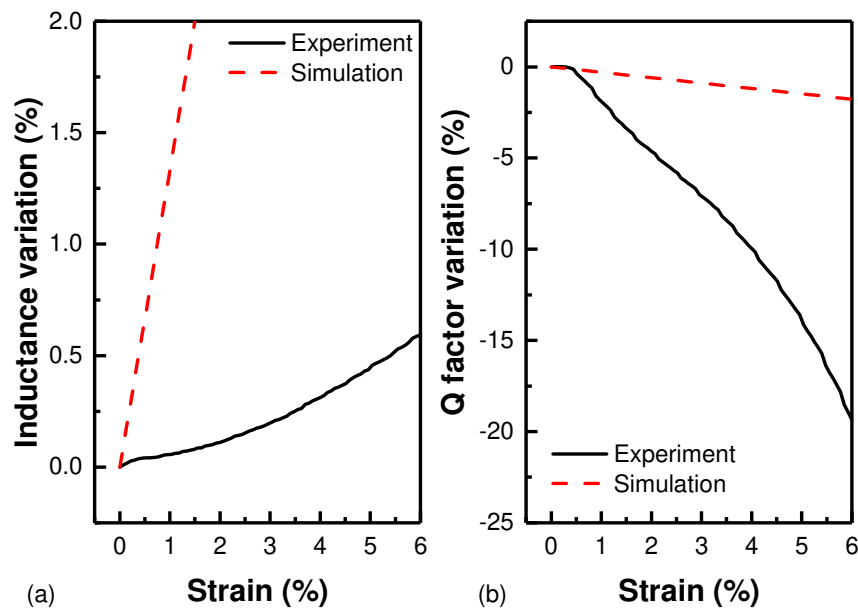


Figure 5.17: Results in (a) inductance variation and (b) Q factor variation and their comparison with simulation results.

The AC response from stretchable interconnects vary with different designs, as concluded in **Figure 5.18**. “Serp 260” design interconnects prove a much higher stretchability, but their inductance shows a higher variation against strain as indicated in magnified trends from each design **Figure 5.18(b)**. The interconnect with design “Serp 45” exhibits the lowest variation in inductance. However, the interconnects with “Serp 260” design still reveals to be the optimised design due to its stable Q factor under strain, as displayed in **Figure 5.18(c)**. The more the Q factor drops, the better inductive behaviour from the conductor can be observed.

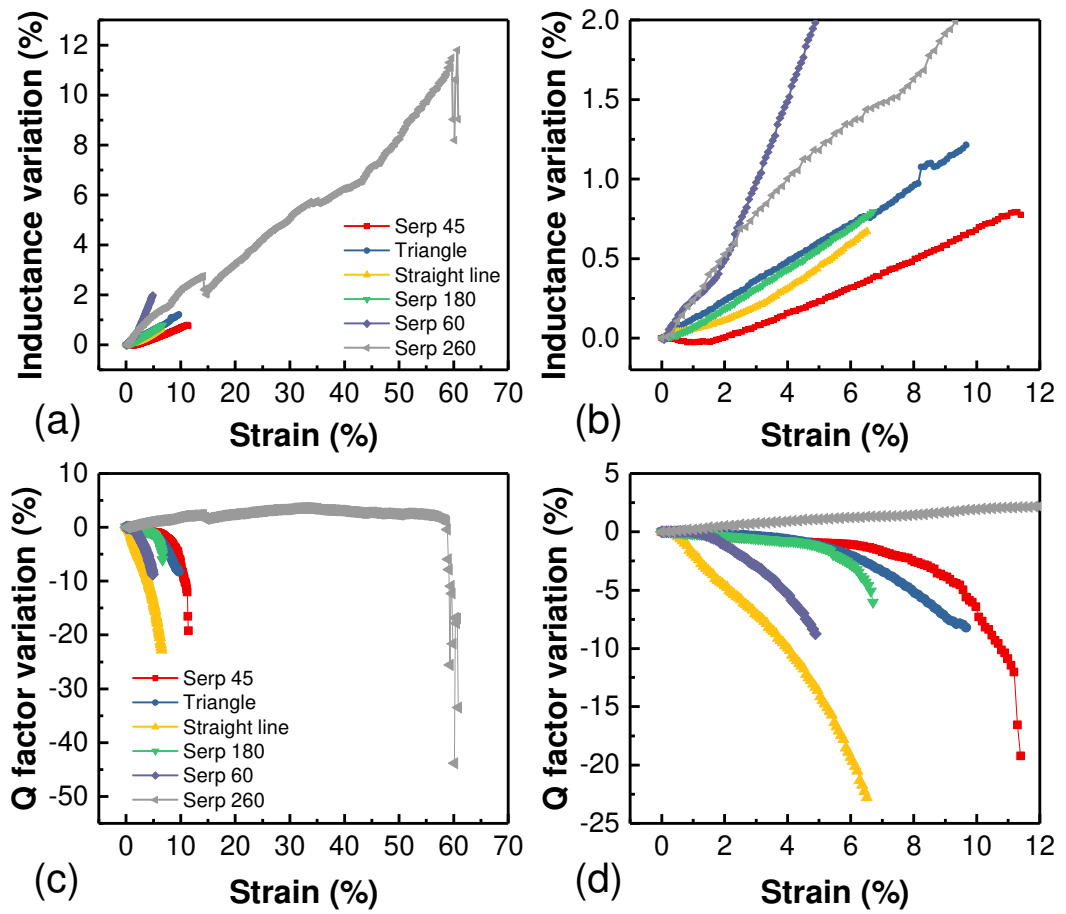


Figure 5.18: Comparison in (a-b) inductance variation between different interconnect designs and (c-d) Q factor variation between different interconnect designs

## Summary

This chapter presented the key results from the developed stretchable interconnects. Concluded in **Table 5.2**, pure metallic thin film based interconnects exhibit a low stretchability due to the dramatically increased density of cracks observed through a microscope. The bulk strip metallic film exhibited a slightly higher degree in stretching, but with an extremely large resistance variation. The stretchability in this case highly relies on crack density in the conductor. If the number of cracks are constant under the same strain, the patterned metallic film will have a higher density of cracks due to the reduced area. Therefore, it is observed that the patterned metallic films have a lower stretchability than bulk film. Compared with pure metallic thin film, the metal-PEDOT:PSS hybrid film has shown a much higher stretchability. Furthermore, the variation in resistance can remain within 1%. Aside from the hybrid film, the graphite-PEDOT:PSS composite also shows similar stretchability (~80%). However, the resistance is not stable against strain. Among all the materials, the Au-PI dual layer interconnects proved to have the most stable electro-mechanical response against strain (0.2%) with the maximum stretchability. If the design at the junction between interconnect and contact pad can be improved, interconnects with higher stretchability can be achieved. Hence, the Au-PI dual layer interconnects are observed to be a potential candidate to be applied in sensors integration, more investigations have been conducted. For example, the encapsulation of interconnects leads to an approximate 16% reduction in stretchability. The electro-mechanical response of the Au-PI interconnect in the AC region was also investigated. In general, the inductance is increasing for all the interconnect designs. However, the Q factor is strongly affected by resistance. The lower the Q factor leads to a higher energy loss within the inductor. Hence, the “Serp260” design has shown its advantages, as its Q factor is stable over a large strain range (~60%). The experiment results for Au-PI interconnects also align with the simulation results discussed in **Chapter 3** except for one design. The sequence of simulated stretchability of different interconnect designs is Serp260 > Serp45 > Triangle > Serp180 > Serp60 > Straight line. However, the experimental results indicate that the “Serp60” design is less stretchable than the straight line design. This may be due to the poor design between the interconnect and the contact pad, as discussed in **Section 5.5**. To achieve a reliable and highly stretchable interconnect, in addition to the design of serpentine-shaped interconnect routings important, the contact pad and its connection designs are also critical to interconnects.

Table 5.2: Comparison of electro-mechanical response among stretchable interconnects based on different materials.

Material	Sheet resistance	Stretchability	Resistance variation	Failing mechanism
<b>Metal (Au)</b>	2.6 $\Omega/\square$	Bulk $\rightarrow$ 4-8% Patterned $\rightarrow$ 1%	Bulk $\rightarrow$ 100 times Patterned $\rightarrow$ 80%	Cracks in films
<b>Au-PEDOT:PSS</b>	8.3 $\Omega/\square$	Patterned $\rightarrow$ 71.9%	Patterned $\rightarrow$ 57000 times	Cracks in films
<b>Graphite-PEDOT:PSS</b>	695.7 $\Omega/\square$	Bulk $\rightarrow$ 80%	Bulk $\rightarrow$ 1000 times	Cracks in films
<b>Au-Polyimide</b>	5.1 $\Omega/\square$	Patterned $\rightarrow$ 101%	Patterned $\rightarrow$ 0.2%	Interconnect-Contact pad junction failure

## Chapter 6 Sensors' integration and applications

This chapter demonstrates the sensors' integration with stretchable interconnects and their applications. Two types of sensors are demonstrated, namely electrochemical pH sensor and strain sensor.

### 6.1 Stretchable system for sweat pH monitoring

This section is extracted from the published paper “Stretchable wireless system for sweat pH monitoring” in *Biosensors and Bioelectronics*, Volume 107, 1 June 2018, Page 192-202 [4].

#### 6.1.1 Introduction

Recent technological advances in the field of flexible electronics and wireless communication have fuelled a new wave in the healthcare sector by enabling non-invasive methods for continuous monitoring of key physiological parameters such as heart rate, blood pressure, skin temperature, electrocardiogram and respiration rate [23]–[26]. Wearable systems based on these technological advances underpin the shift in the healthcare paradigm towards individual-centric management of health, also known as mobile health (mHealth) [211] self-health management [212]. The electronics on flexible and stretchable substrates allows wearable systems to conform to body parts and thus improves the reliability of non-invasive data collection. Non-invasive systems for diagnosis and health monitoring (particularly for chronic ailments) will have a major impact on healthcare practices as patients are likely to be more compliant with such methods [27]. These methods are also attracting a lot of attention due to ease of use. In addition, such systems can be used in low-resource settings without the need for highly-trained medical staff, and have the potential to greatly improve patient care in disease outbreaks where complex sample handling is undesirable. For this reason, recently there has been increased interest in monitoring health conditions through body fluids such as sweat, tears, and urine etc. [213], [214].

As depicted in **Table 6.1**, various analytes such as glucose, urea, ascorbate are found in the blood as well as in tears and sweat and research suggests that there is a correlation between them. These body fluids could be a potential treasure trove for diagnosing several diseases (including chronic diseases) and might eliminate the need for acquiring blood samples. As an example, the pH value of a healthy person is in the range of 4.5-6.5, but

## Chapter 6

patients with cystic fibrosis have alkaline sweat (up to pH 9) due to the defect in bicarbonate-reabsorption ( $H^+$ -secretion) [215]. The pH value in sweat is also an indicator for the human body's exercise intensity and dehydration level. While exercising, the concentration of ammonia in sweat decreases, due to its transformation into ammonium ( $NH_4^+$ ). As  $NH_4^+$  is less diffusible across cellular membranes compared to ammonia, the excess  $NH_4^+$  molecules accumulate ions, which leads to an increase in sweat pH [216], [217]. Considering these, the reliable monitoring of sweat pH is essential for health monitoring and wellness applications. This is a vital step towards realising a multi-sensory conformable system for a comprehensive sweat-based health monitoring.

Table 6.1: Analytes in blood, tears, and sweat with their diagnostic significance [213], [218], [219].

Analytes	Blood (mM)	Tear (mM)	Sweat(mM)	Diagnostic application
<b>Glucose</b>	3.3-6.5	0.013-0.051	0.33-0.65	Hyper/hypo Glycaemia /Diabetes
<b>Lactate</b>	3.6-7.5	1.1-2.1	13.4-26.7	Ischemia, Sepsis, Liver disease, Cancer
<b>Urea</b>	6.2±0.9	3.0-6.0	22.2±8.0	Uraemia indicating Renal dysfunction
<b>Creatinine</b>	0.077-0.127	0.014-0.051	0.014-0.051	Renal dysfunction
<b>Na<sup>+</sup></b>	140.5±2.2	120–165	66.3±46.0	Hyper/hyponatremia
<b>K<sup>+</sup></b>	4.8±0.8	20–42	9.0±4.8	an indicator of ocular disease
<b>Ca<sup>2+</sup></b>	2.0–2.6	0.4–1.1	4-60	Hyper/hypo Calcemia
<b>Mg<sup>2+</sup></b>	0.7–1.1	0.5–0.9	0.6	Acidosis and muscle contraction
<b>Cl<sup>-</sup></b>	98.9±6.7	118–135	59.4±30.4	Hyper/hypo Chloremia
<b>Pyruvate</b>	0.1–0.2	0.05–0.35	0.003- 1	Disorders of energy metabolism
<b>Ascorbate</b>	0.04–0.06	0.22–1.31	0.43	Diabetes

It is challenging to have a fully integrated wearable system (with data process and transmission modules) that could maintain a conformal physical contact with human skin, especially under dynamic motions [25], [220], [221]. A few methods explored to improve conformal contact include using ionogel as a sensitive layer [222], adhesive stickers [223] and tattoo papers [220]. These sensing solutions are not stretchable and long-term wearing of stickers may cause irritation. Furthermore, it is difficult to realise a miniaturised and light-



## Chapter 6

weight wearable system with integrated signal transmission circuitry, especially with non-flexible or rigid devices used for Bluetooth technology [223]–[225]. These reported solutions allow continuous wireless data transmission, but with bulky and rigid Bluetooth modules, which also consume significant energy and require frequent charging. This issue could be addressed with stretchable radio-frequency-identification (RFID) coils, as demonstrated here.

The demonstrated stretchable pH sensing system comprises a stretchable pH sensor with stretchable RFID antenna and data processing and transmission circuitry to communicate with a smartphone, as shown in **Figure 6.1(a)**. This system has several advantages in terms of fast pH sensing response, mechanical robustness and real-time data transmission under dynamic motion. The sensing electrodes of the pH sensor are based on the graphite-polyurethane composite. The pH sensing electrode (SE) and the printed Ag/AgCl quasi-reference electrode (RE) are connected through stretchable interconnects to allow the pH sensor to withstand up to 53% strain without compromising their electrical performance. As human skin experiences an average strain of 30% [226], the stretchable pH sensing patch presented here can be conformably attached to the skin and used with minimal influence on their electrical performance. To demonstrate the wireless data transmission, the pH sensor patch is integrated with a stretchable antenna and the pH value from the sweat equivalent solution is acquired through a mobile phone App.

### 6.1.2 Experiments

#### a. pH sensor design and fabrication

The pH sensor comprises a pair of stretchable interconnects, and graphite-polyurethane composite together with an Ag/AgCl reference electrode as a potentiometric sensing structure, as illustrated in **Figure 6.1(b)**. The optimal geometry of stretchable interconnects which has been optimised in previous studies (**Chapter 3**). The graphite-polyurethane composite-based pH SE and Ag/AgCl RE are deposited on the contact pad ( $1 \times 1 \text{ mm}^2$ ) of interconnects ( $500 \text{ }\mu\text{m}$  width). The overall sensor is encapsulated in the polydimethylsiloxane (PDMS).

## Chapter 6

The detailed fabrication process of stretchable interconnects is illustrated in **Figure 6.1(c)**. Firstly, the polyimide (PI) (DuPont) was spun on 100 nm-thick poly(methyl methacrylate) (PMMA) (Sigma Aldrich) coated silicon wafer at the spin rate of 3000 rpm for 30 s. Curing for three hours at 200°C in nitrogen ambient resulted in the PI film with 7  $\mu\text{m}$  thickness (confirmed by interferometer (Leitz Ergolux) measurement). Then, a stack

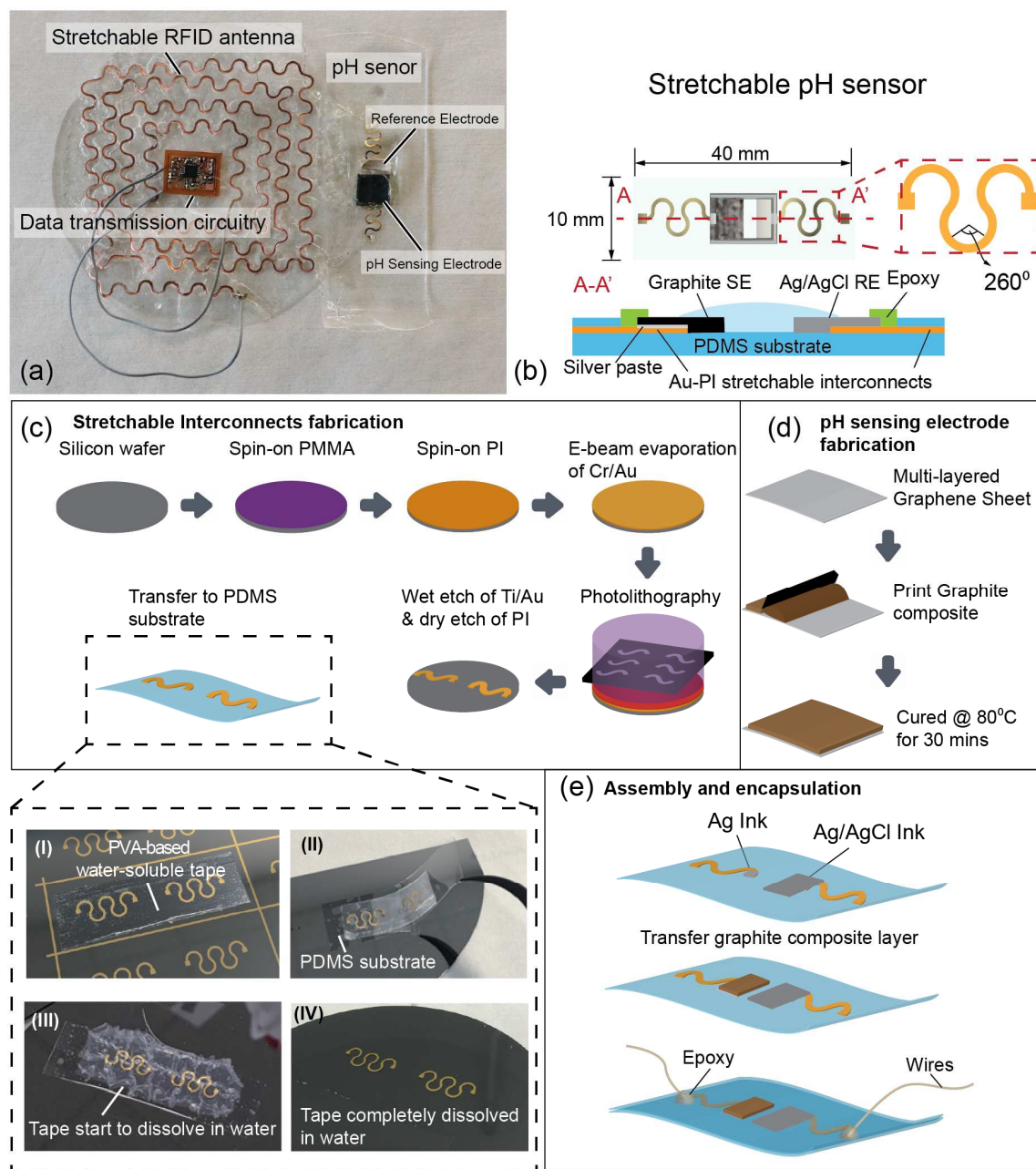


Figure 6.1: (a) Photo of a stretchable wireless system for sweat pH monitoring, (b) Schematic diagram of a stretchable pH sensor with graphite-polyurethane composite SE, Ag/AgCl-based RE and a pair of stretchable interconnects. Schematic diagram of the fabrication process for (c) stretchable interconnects, (d) SE electrodes (e) assembly and encapsulation of sensor patch.

## Chapter 6

of Cr/Au (5/150 nm) metal was electron beam (e-beam) evaporated and this was followed by a brief (15s at 200W) oxygen plasma treatment on PI film. In the next step, a 10- $\mu\text{m}$ -thick positive photoresist was used with a bright field mask. During the UV exposure and development processes, the designed pattern protects the metal stack from wet etching and the PI film from dry etching. The interconnects fabricated on a silicon wafer were then transferred to a PDMS substrate by using water-soluble tape (3M, US), as shown in **Figure 6.1(c)(I-IV)**. The PDMS substrate (180  $\mu\text{m}$  thick) was obtained separately by spin coating a 10:1 (base polymer: crosslink) the solution on a silanised silicon wafer at 300 rpm for 60 s and curing in the oven for 2 hours at 80°C.

For each pH sensor, a pair of stretchable interconnects was previously transferred to the PDMS substrate. The pH SE was fabricated by printing graphite-polyurethane composite (1:1 ratio) paste on the top of multi-layered graphene sheet (Graphene Supermarket, US), which accelerated the electron transportation during the ion exchange between the SE and the solution. The electrode was then cured in an oven at 80°C for 30 minutes. The fabrication procedure of pH SE is shown in **Figure 6.1(d)**. After obtaining the pH SE, the SE and RE electrodes were assembled and encapsulated, as shown in **Figure 6.1(e)**. The pH SE (8×8 mm<sup>2</sup>) was connected to one of the stretchable interconnects by using conductive epoxy silver ink. The Ag/AgCl ink (Gwent Group, UK) [200] then dropped cast to the contact pad from the second interconnect, which is used as RE in the sensor. To ensure a robust connection between SE/RE and stretchable interconnects, the epoxy glue was applied to the connection area. The epoxy glue also serves as a barrier during drop casting of top encapsulation PDMS layer to allow the sensing area to contact with the solution under test.

### b. Stretchable antenna design and fabrication

The stretchable RFID antenna developed here is effective for Near Field Communication (NFC), which requires 13.56 MHz resonant frequency. The antenna is designed to have inductance together with the capacitors and the internal capacitance to match with the RFID transponder IC (TI RF430FRL152H), used here as an interface between the sensor and the antenna coil (**Figure 6.2(a)**). The specification of the transponder IC requires a 1.84  $\mu\text{H}$  inductance. The designed square-shaped spiral coil antenna has an inductance of 1.88  $\mu\text{H}$ . This value was estimated through a modified wheelers equation [227]:

$$L = \frac{\mu n^2 d_{avg} C_1}{2} \left( \ln \left( \frac{C_2}{\rho} \right) + C_3 \rho + C_4 \rho^2 \right) \quad (6-1)$$

## Chapter 6

Where,  $\mu$  refers to the vacuum permittivity ( $4\pi \times 10^{-7}$  H/m),  $n$  is the number of turns in the loop,  $d_{avg}$  is the average diameter of antenna ( $d_{avg} = \frac{d_{out} + d_{in}}{2}$ ),  $\rho$  is the fill ratio ( $\rho = \frac{d_{out} - d_{in}}{d_{out} + d_{in}}$ ) and the  $C_i$  are the coefficient based parameters. The square-shaped antenna has 4 turns with the turn width of 1 mm and 1 mm spacing between adjacent turns. The outer/inner dimension of the antenna is 6/4.6 mm. The antenna design was further modified to obtain wavy or serpentine-shaped coils, as shown in the inset of **Figure 6.2(b)**. The inner/outer radius of the wavy structure is 1.5/2.5 mm with an arc degree of 180°. The minimum space between each turn of the coil is 1 mm. To estimate the influence of stretching on the antenna's output, an approximate estimation was performed using basic magnetic flux  $\frac{d\Phi_B}{dt} = \frac{d}{dt} \int B(t) d(A)$  and self-inductance equations  $\frac{d\Phi_B}{dt} = L \frac{di}{dt}$ . The induced magnetic flux is strongly related to the area enclosed by the coil. The maximum strain which the antenna can withstand (calculated from the length of stretchable antenna) is about 40%. For a square-shaped in-plane coil, the influence of stretching on the area  $A$  was estimated by using equation  $A'/A = (1 + \varepsilon) \cdot (1 - \nu\varepsilon)$ . Here  $A'$  is the enclosed area after stretching,  $\varepsilon$  is the external strain introduced during stretching and  $\nu$  is the Poisson's ratio. Considering the Poisson's ratio is 0.34 (for copper) and 0.4 as strain, the area will increase by 20%.

To fabricate the designed antenna, a rapid prototyping method with blade cutters (Silhouette Cameo) was used. The cutting system used here results in cut-width of about 50  $\mu\text{m}$ . As compared with the standard microfabrication, this method is economical and faster. To obtain the antenna with high conductance, we used a flexible polyimide film with copper clad (Pyrallux, DuPont) on one-side. The thickness of polyimide and copper films are 94  $\mu\text{m}$  and 18  $\mu\text{m}$  respectively. Prior to blade cutting, the water-soluble glue was applied to the copper sheet and the sheet was then laminated to the cutting mat (**Figure 6.2(i, d)**). During blade cutting, the parameters such as blade speed, height, and cutting thickness were adjusted to prevent the copper sheet from being damaged (**Figure 6-2(ii)**). Then, the remainder of the material was carefully removed (**Figure 6.2(iii)**). Afterwards, the patterned antenna structure was transferred to blue tape (dry photoresist) by dissolving the sacrificial water-soluble layer in the water (**Figure 6.2(iv-v, e)**). In the following step, the patterned antenna on blue tape was adhered to the partially cured PDMS substrate (spin-coated on a silicon wafer and baked for 30 mins at 70°C). The blue tape was dissolved in acetone after the PDMS was fully cured (**Figure 6.2(vii, f)**). At last, the stretchable antenna on the PDMS substrate was detached from the silicon wafer (**Figure 6.2(viii)**). The inductance of the fabricated antenna, measured by LCR meter (E4980AL, Keysight), was found to be 1.89  $\mu\text{H}$ .

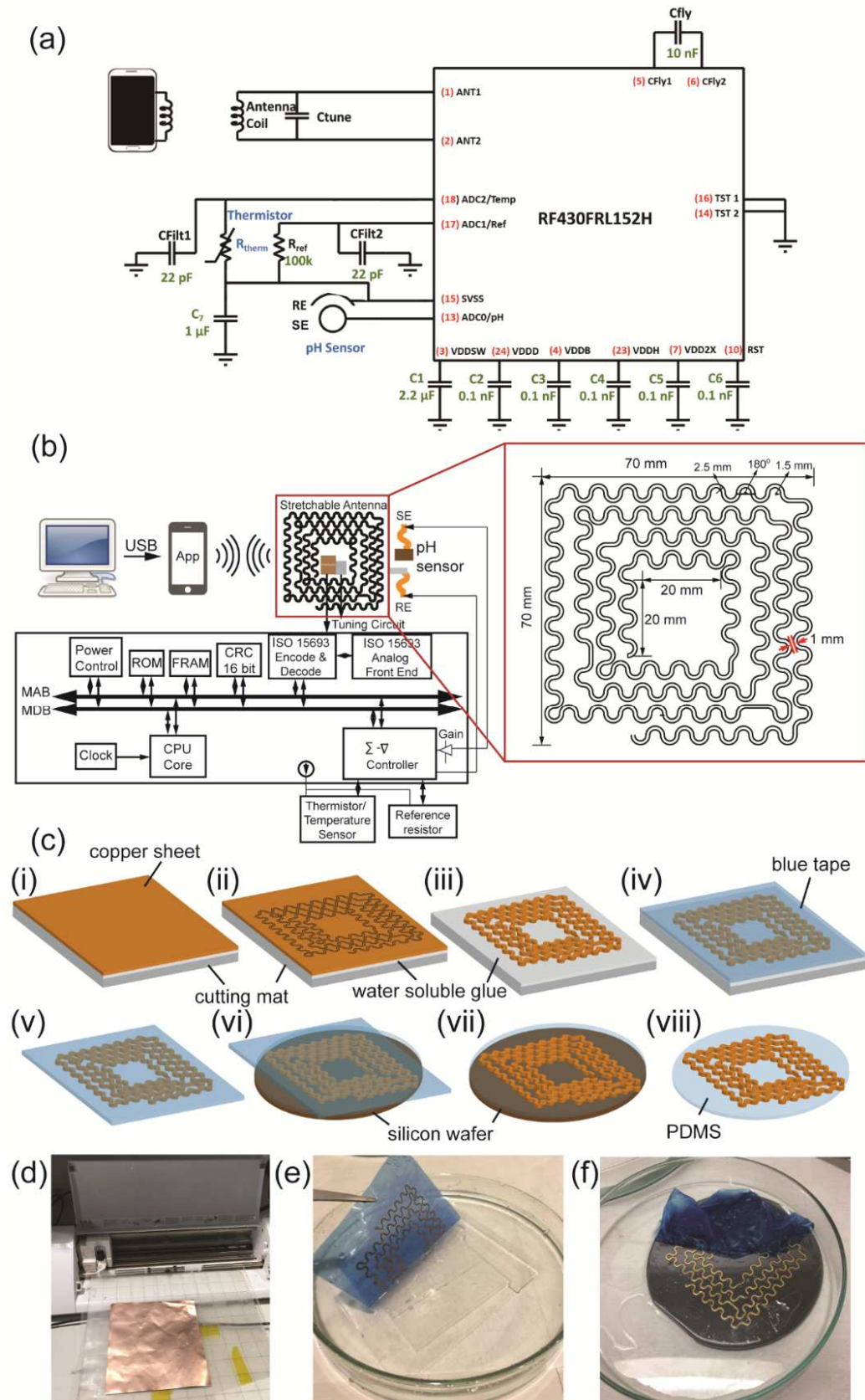


Figure 6.2: (a) Circuit design and (b) system-level block diagram for wireless pH data transmission with the inset image of antenna design and (c) Fabrication steps of stretchable

## Chapter 6

antenna including (i) laminating flexible copper sheet to cutting mat with water-soluble glue as sacrificial layer, (ii) blade cutting the antenna pattern, (iii) removing the reminder of material, (iv) attaching the blue tape over the antenna pattern, (v) dissolving the glue in water and transferring the antenna pattern to blue tape, (vi) adhering to partially cured PDMS substrate (separately prepared through spin-coating on the silicon wafer), (vii) curing PDMS and dissolving blue tape in acetone and (viii) detaching the PDMS substrate from silicon wafer. Photos of critical steps c(i), c(v) and c(vii) are also included in (d), (e) and (f) respectively.

### c. Reagent for pH sensor characterisation

Three sets of testing solution were used for performance analysis of the fabricated sensors. These include: (1) pH buffer solution ranging from 5 to 9 (Sigma Aldrich); (2) Dulbecco's Modified Eagle Medium (DMEM, Sigma-Aldrich), which is a standard culture medium used for maintaining mammalian cell *in vitro*; and (3) solution equivalent of human sweat prepared by mixing NaCl (Sigma Aldrich), KCl (Sigma Aldrich) and lactic acid (Sigma Aldrich) in deionised water according to the concentration in **Table 6.1**. The pH value of DMEM was tuned by adding diluted HCl and KOH solutions. The pH measurement technique used for acquiring reference values in all comparison studies and for calibration were acquired by using a commercial digital pH tester HI 98130 from Hanna® Instruments fitted with an HI 73127 pH electrode, except for some samples in which case standard buffered pH solutions from Sigma Aldrich were used. The pH tester was calibrated with standard buffer solutions before measurement. The specifications of the pH testing system used to acquire reference values include a range of 0.00 to 14.00 pH with a resolution of 0.01 pH and accuracy of  $\pm 0.05$  pH. Further, the system has an automatic temperature compensation by using an inbuilt temperature sensor with resolution and accuracy of 0.1°C and  $\pm 0.5^\circ\text{C}$  respectively. The electrochemical characterisation of the pH sensor was analysed with cyclic voltammetry (CV), electrochemical impedance spectroscopy (EIS) and potentiometric methods in a two-electrode (SE and RE) system with Autolab electrochemical workstation (PGSTAT302N, Metrohm, Netherland). The CV analyses were carried out at a scan rate of 100 mV/s in the potential range of -1 to 1 V. EIS analysis was carried out in a frequency range of 10 Hz to 1 MHz with an amplitude of 10 mV. To test the electrochemical performance of the sensor under the influence of ions and analytes including  $\text{Na}^+$ ,  $\text{K}^+$ , and glucose which can be widely found in sweat (as shown in **Table 6.1**), we

## Chapter 6

prepared dissolved salt solutions of 100 mM NaCl, 100 mM KCl and 100 mM glucose. To further investigate the influence of NaCl on SE's property, we prepared three sets of NaCl concentration (1 mM, 10 mM, and 100 mM). To test the robustness of the fabricated stretchable sensor, the patch was tested with a controlled uniaxial stretch test setup. This stretch test setup has two stepper motors (Micronix, USA) which can stretch the sample from the two sides. For stretchability test of the sensors presented here, the stepper motor was moving at 0.5 mm/s. The resistance between the graphite-polyurethane composite electrode and stretchable interconnect was monitored through a multi-meter (34461A, Agilent).

### 6.1.3 Results and discussion

#### a. pH sensor characterization

The electrochemical reaction at the surface of SE was measured using CV analysis at a scan rate of 100 mV/s. The CV curve of SE in a buffer solution of pH value 7 (**Figure 6.3(a)**) shows that there is no redox or oxidation reaction between the active electrode and the solution. The results from CV analysis (**Figure 6.3(a)**) predict non-Faradaic electrochemical reaction and indicate an ideal CV scan for a graphite-based electrode. As per general mechanism, when the SE reacts with the solution, an electrical double layer (EDL) structure is formed on the surface of the electrode by absorption of ions. This is due to the non-Faradaic electrochemical reaction between the graphite composite based electrode and the solution. The changes in pH value of the solution lead to variations in the solution resistance ( $R_{ser}$ ), charge transfer resistance ( $R_{ct}$ ), double layer capacitance ( $C_{dl}$ ) and ionic exchange resistance at the electrode-solution interface. The variation of these parameters can be measured by using complex impedance data of the EIS analysis. These parameters were optimised by measuring the variations in the impedance and capacitance values with a pH value of the solution. However, with reference to readout electronics, the sensitivity is explained in terms of the potential difference between SE and RE. The potentiometric readout is advantageous as it simplifies the circuit design.

The complex impedance data of the sensor was analysed by using Nyquist plot (**Figure 6.3(b)**), which shows a straight line in the lower frequency section and a semicircle in the higher frequency range. A similar Nyquist plot can be found for graphite-polyurethane composite in ion detection [228]. The straight line could be attributed to the diffusion of  $H^+/OH^-$  ions from the solution into the graphite electrode. The impedance due to the diffusion of ions also depends on the structural properties of the material. For an ideal



## Chapter 6

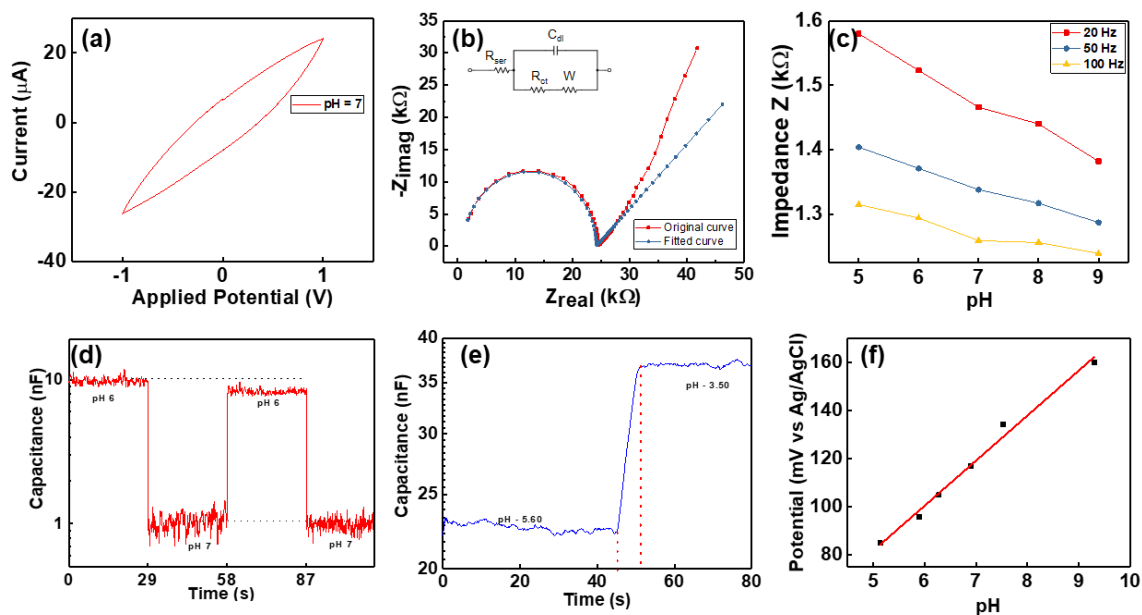


Figure 6.3: (a) CV curve and (b) Nyquist plot for graphite-polyurethane composite electrode at pH 7 buffer solution and fitted curve based on Randles circuit model (c) impedance versus pH measured between SE and RE at selected frequencies (d) hysteresis in pH response and (e) response time of the sensor (f) potentiometric performance of the pH sensor.

capacitor, allowing perfect ion diffusion of the electrode, the angle of this curve should be  $45^\circ$ . However, our experimental results indicate approximately  $32^\circ$ , at a neutral pH value. This indicates a capacitive reactance behaviour due to material structure and less ionic concentration at the neutral solution. The Nyquist plot was analysed using Autolab NOVA software (Metrohm, Netherland). The measured curve was fitted by using the Randles circuit model, which consists of equivalent  $R_{\text{ser}}$ ,  $C_{\text{dl}}$ ,  $R_{\text{ct}}$  and Warburg diffusion element ( $W$ ). The fitted Nyquist curve matches the measured curve perfectly in high-frequency range. The value of  $R_{\text{ct}}$ , which is reflected by the diameter of the semi-circle, was estimated to be  $23.2 \text{ k}\Omega$ . The charge transfer resistance is related to solution/electrode interaction and transfer of electrons from the SE to the external conducting electrode. Some offset in the low frequency range can be observed. This is due to the low diffusion resistance of pH SE. It can indicate a capacitive reactance behaviour due to material structure and less ionic concentration at the neutral solution. The steep line observed in the low frequency region of the Nyquist curve also proves a double layer capacitive behaviour. The EIS analysis (**Figure 6.3(b-c)**) shows that the variations in solution pH changes the electrical properties of EDL and as a result, the impedance of SE varies.



## Chapter 6

The SE electrode was further characterised in DMEM solution, which is a medium used as a blood equivalent solution to check the pH value of a body fluid. This solution offers minimised ion reaction property, which prevents the pH drifting in the solution when diluted HCl/KOH is added for different pH measurement, especially in the range 5-9. **Figure 6.3(c)** exhibits the impedance variation of DMEM solutions at different pH values. A similar observation is found for variations in capacitance at various pH values. The sensor shows a sensitivity of  $49 \Omega/\text{pH}$  at 20 Hz sweeping frequency. The hysteresis effect of the pH sensor was investigated by continuously monitoring its electrical response in terms of capacitance while alternating the pH of the solution between 6 and 7, as shown in **Figure 6.3(d)**. The deviation of the pH sensor's capacitance at the same pH is not significant. The curve indicates a fast and uniform recovery after every cycle. We estimated the response time by altering the pH in the solution and the pH sensor exhibits a fast response with a response time of 8 seconds as shown in **Figure 6.3(e)**. The response time of the sensor is contributed by many factors including the material, the fabrication process and the surface morphology [229]. In general, one of the major issues in thick-film sensors is their high potential to interfere with other ions or analytes in the solution. As shown in **Table 6.1**, sweat contains glucose in the range of 0.33-0.65 mM,  $\text{Na}^+$   $66.3 \pm 46.0$  mM, and  $\text{K}^+$   $9.0 \pm 4.8$  mM. To test the interference effect of the pH sensor with a distinguishable electrical response, the ions and analytes are used here in a much higher concentration (100 mM). The influence from  $\text{Na}^+$ ,  $\text{K}^+$  ions, and glucose on the pH sensor is estimated by monitoring the capacitance of the sensor due to change in the conductivity of the solution by adding salts of  $\text{Na}^+$  and  $\text{K}^+$ . The relative change in the capacitance is -0.32 for  $\text{Na}^+$ , -0.28 for  $\text{Na}^+$  and  $\text{K}^+$  and -0.29 for  $\text{Na}^+$ ,  $\text{K}^+$ , and glucose. A comparatively higher change in capacitance is observed for  $\text{Na}^+$ , which could be attributed to the conductivity of the solution. In addition, no redox or oxidation reaction is observed between SE and the solution. Hence, it can be concluded that major ions and glucose in sweat will have a minor influence on the performance of the fabricated pH sensor.

To transmit pH data in a straightforward way, we also carried out the potentiometric analysis. The measured potential difference (emf- electromotive force) between SE and RE is shown in **Figure 6.3(f)**. We observed a sub-Nernstian response with a sensitivity of  $13.76 \pm 5.45 \text{ mV/pH}$  ( $n=4$ ) in the range of pH 5-9.5 at room temperature.

## Chapter 6

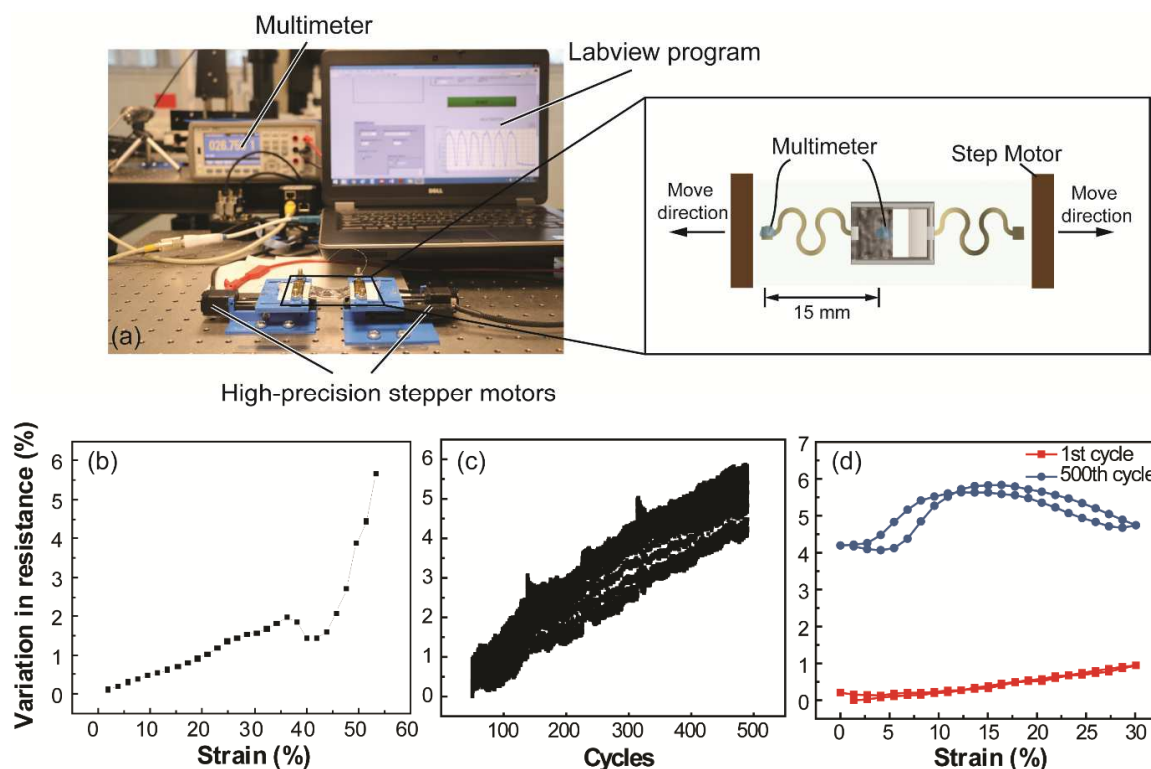


Figure 6.4: (a) The electro-mechanical characterisation setup controlled with custom LabVIEW programme. The inset shows the birds-eye-view of stretchable pH sensor mounted on the setup. The sensor is symmetrically integrated with two interconnects. During stretching, only one side (one interconnect with working electrode) is monitored dynamically. (b) The variation in resistance across pH sensing electrode and stretchable interconnect with respect to the external strain experienced by the pH sensor. (c) Cyclic stretching test for stretchable pH sensor up to 30% strain. (d) Comparison in resistance variation between the first cycle of stretching and releasing and 500<sup>th</sup> cycle.

## b. Characterization of pH sensor under stretch conditions

To test the performance of the pH sensor under stretching conditions, the resistance between the SE and stretchable interconnect is measured with the experimental setup shown in **Figure 6.4(a)**. The original distance between one end of the interconnect and the graphite-polyurethane composite electrode is 15 mm. The maximum extension distance from one side of the stepper motor is 8 mm, which corresponds to 53% uniaxial strain. The failing part from the sensor is at a connection area where the graphite-polyurethane composite and stretchable interconnects joint. At this strain, the resistance variation is 5.6%, as shown in **Figure 6.4(b)**. This resistance variation can be attributed to: (i) the deformation in

## Chapter 6

conductors; (ii) change in contact resistance between the graphite-polyurethane composite and stretchable interconnects; and, (iii) change in surface area of the micro-structured graphite-polyurethane composite electrode during bending. To evaluate the robustness of the pH sensor, a further cyclic stretching test was carried out. The sensor was tested up to 500 cycles under 30% strain and the electrical response was found to be stable (**Figure 6.4(c)**). By comparing the resistance between the first cycle of stretch and the 500<sup>th</sup> cycle (**Figure 6.4(d)**), the variation in resistance increases from about 1% after the first cycle to about 6% after the 500<sup>th</sup> cycle.

### c. Stretchable antenna characterisation

The response of a stretchable antenna was evaluated through a vector network analyser (VNA) (Agilent E8362B). This included performance evaluation during stretching. The S-parameter was measured with a frequency range between 10 MHz to 40 MHz. This parameter represents the power reflected through the antenna. The measurement results reveal that the S11 of the antenna is reduced by - 1.5dB at 13.56 MHz after tuning with the circuit. No shift or distortion was observed in the S-parameter curves for 20% stretched condition. This indicates a stable signal radiation performance of the stretchable antenna.

## Chapter 6

## d. Evaluation of full system

The real-time wireless pH measurement capability of the developed stretchable sensing system was evaluated, as shown in **Figure 6.5**. A custom smartphone App “SenseAble” was developed with two options for pH data display (**Figure 6.5(a)**). The first option allows display of the pH value calibrated on the basis of potentiometric measurement. The second option displays the potential between SE and RE. The temperature from human skin can also be measured as the third option. Considering the influence of temperature on pH sensitivity, the App allows the user to re-calibrate the pH data based on the temperature change. To validate the full system, the fabricated pH sensor was evaluated with a solution equivalent to human sweat. The pH value was wirelessly transmitted to the App as shown in **Figure 6.5(b)**. The sensitivity of the pH sensor with a solution equivalent of human sweat is about  $11.13 \pm 5.8$  mV/pH ( $n=3$ ), which is slightly less compared to the sensitivity with the DMEM solution. Unlike the DMEM solution, the solution equivalent of sweat contains excess ions when the pH is varied. The slight variation in the pH value could be attributed to the excess ions affecting the stability of the solution. The ion reaction disturbs the stability of the solution and leads to pH drifting.

## 6.1.4 Conclusion

In this work, a stretchable system for wireless monitoring of pH from sweat was presented. The pH sensor is based on a novel combination of graphite-polyurethane

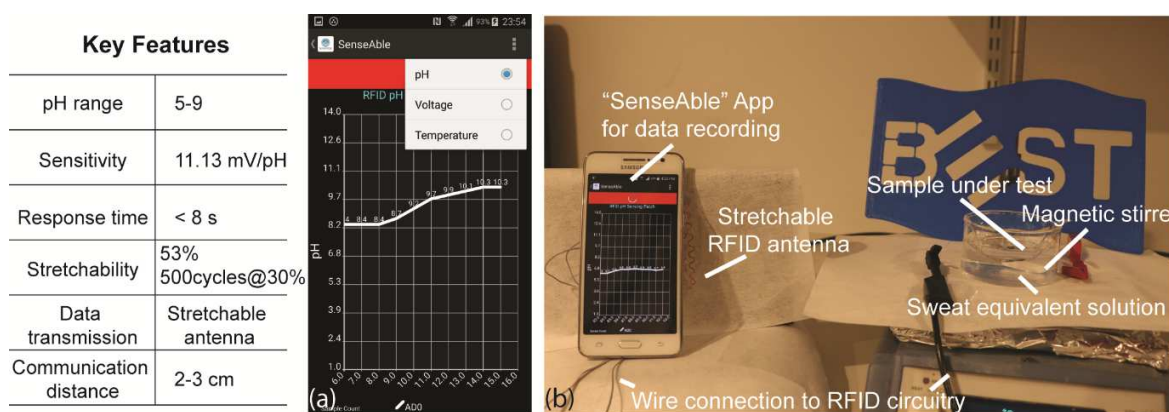


Figure 6.5: (a) Screenshot of smartphone App “SenseAble” and (b) photo of real-time pH monitoring system including stretchable pH sensor in sweat equivalent solution, stretchable antenna and mobile monitoring App.

## Chapter 6

composite material. An extensive electro-chemical study performed to characterise the pH sensor shows the sensor response in the pH range of 5-9. The pH sensitivity of the fabricated stretchable sensor tested on the human sweat equivalent solution is  $11.13 \pm 5.8$  mV/pH. The interference by major ions and glucose in sweat are negligible. The pH sensing patch with integrated stretchable interconnects is robust with stretching up to 53% strain and more than 500 cycles for 30% strain. The stretchable RFID antenna allows the pH data to be read out without external power through a custom-developed smartphone App. The stretchability also leads to improved conformability of pH sensor system. Compared with the reported wearable pH sensing devices, our stretchable system is advantageous in being highly stretchable and conformable to the skin, while offering faster pH sensing response and convenience in terms of wireless data transmission. The costliest component in the developed system is the RF430FRL152H NFC microcontroller IC including which the system could be made less than ~\$3.5. The sensor can be disposed-off separately or the entire system could be disposed of. Further, the use of a low-power microcontroller helps in local computations for carrying out advanced digital signal processing, multi-sensor calibration routines, flexibility, and reconfigurability before transmitting the data to the mobile phone. This feature is not available in other implemented systems reported in the literature. The above research could be extended in several directions, such as detection of multi-biomarkers including glucose, ammonia, and urea with the integrated wearable system, a smart disposable bandage for wound exudate monitoring, multi-biofluidic solutions forming a body area network.

## 6.2 Stretchable strain sensor integrated on the soft robotic finger

This section is extracted from the published paper “Soft robotic finger with integrated stretchable strain sensor” in the Proceeding of IEEE sensors, October 2018 [230]. Copyright © 2018 IEEE.

### 6.2.1 Introduction

Soft robotics is attracting significant attention these days for applications ranging from surgical tools [231] to object handling [28], muscle/tendon rehabilitation [232], and manoeuvring objects under extreme conditions [29]. Unlike rigid-body robots that have restricted movements due to stiff joints, soft materials (e.g. elastomers) in soft robotics

## Chapter 6

expand the degree of freedom from merely the six (three rotations and three translations) to literally infinite [233], [234]. This allows them to perform complex movements of bending, wrinkling, buckling and twisting. The soft materials also act as absorbents or cushions in the event of a collision and thus make soft robots much safer to interact with. These properties are readily available in natural organisms and their complex body/surface architecture has served as inspiration for the development of the coming age of engineered soft devices. However, natural organisms also exhibit tightly integrated sensing, actuation, and computation, which allow them to achieve dynamic shape and appearance changes (e.g. birds in flight), or tactile sensing at very high dynamic range (e.g. human skin) [34]. This is where today's soft robots are failing. While a lot of work is being done on the soft structures (e.g. limbs) to enable complex movements, often by mimicking the morphology of natural organisms, the inherent functionalities such as sensing, actuation, and computation are largely missing. As a result, the real-time feedback and accurate control of soft robots becomes increasingly difficult.

The solutions that are being explored today to address the above issues primarily use off-the-shelf sensing or electronic components [235], [236], which, owing to their rigid structure, nullify to a greater extent the gains made with soft structures. This calls for the development and integration of soft sensor systems with the soft robots. The recent technological advances related to 3D printing of soft materials [237] and printed electronics [89], [238] on soft and stretchable substrates have raised hope for early solutions to the above challenges.

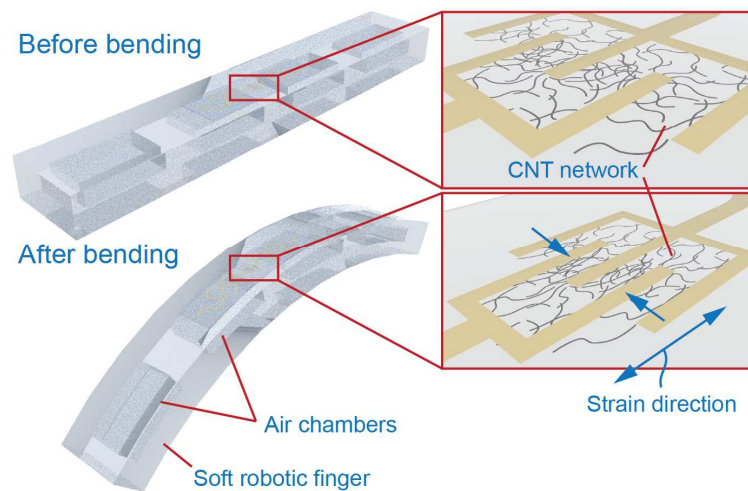


Figure 6.6: Schematic illustration of soft robotic finger with integrated strain sensor. The strain sensor is based on the CNT network.

Building on the advances in stretchable and soft electronics, this paper presents a pneumatic actuated soft robotic finger with integrated stretchable strain sensor based on carbon nanotubes (CNTs) (**Figure 6.6**). The CNT network on interdigitated electrodes of the sensor was assembled with the dielectrophoresis (DEP) method. Further, the sensor is connected to stretchable interconnects to ensure the robust electrical connection during bending of a soft finger. When the robotic finger bends, the stretchable strain sensor experiences changes in the resistance, which can be used to control the actuation and hence the movement of the finger. The developed strain sensor can monitor the bending of a soft robotic finger up to a bending radius of 23 mm.

## 6.2.2 Fabrication and Integration

### a. Fabrication of soft robotic finger

The soft robotic finger was fabricated through the moulding method. The selected material is Ecoflex (Smooth-on, US), which is a highly elastic and biodegradable silicone rubber. The mould was 3D printed (Stratasys, US) with acrylate with the finest structure size of 1 mm. The moulded structure has a length of 40 mm, width of 10 mm and height of 8 mm. The design of the soft robotic finger is composed of four air chambers connected with a 1 mm wide air channel, as illustrated in **Figure 6.7**. After the Ecoflex solution was cured in the mould for 30 minutes at 90°C, the structure can be released from the mould. The TYGON tubing with an inner diameter of 0.8 mm was connected with the air channel in the soft

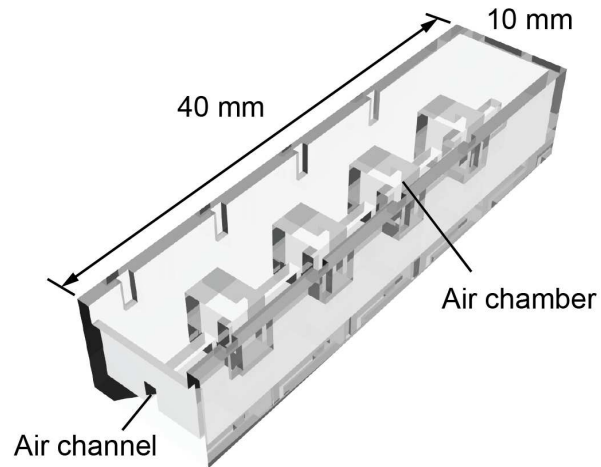


Figure 6.7: Schematic illustration of 3D printed mould to fabricate the soft robotic finger.

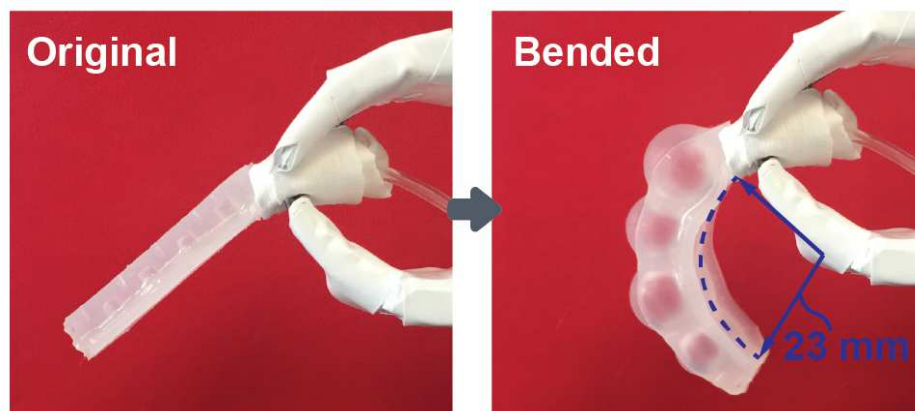


Figure 6.8: Photos of fabricated soft robotic finger before and after pneumatically actuated.

robotic structure and sealed with Teflon tape. The tubing was then connected to the rubber blowing ball. The photos in **Figure 6.8** have shown the pneumatically actuated finger, which is able to bend with a radius of 23 mm under pneumatic actuation. The pneumatic actuation utilises the expansion of the air chamber under air pressure to achieve finger movements.



## b. Fabrication of Stretchable interconnects

The stretchable interconnects were fabricated on silicon (Si) wafer. Firstly, poly (methyl methacrylate) (PMMA) solution was spun on a Si wafer cured on the hotplate at 120°C. Then, PI precursor (PI 2545, HD Microsystems™) solution was spun, as illustrated in **Figure 6.9(a)**. The PI film was soft-baked for 5 minutes at 140°C and fully cured at 200°C for three hours. The thickness of the resultant PI film is ~2 µm. Afterwards, a dual metal layer of titanium (Ti) and gold (Au) with 10 and 100 nm thicknesses were deposited through E-beam evaporation (**Figure 6.9(b)**). The pattern of interconnects was realised by photolithography and the photoresist from this step was used as a protection layer for subsequent etching steps (**Figure 6.9(c-d)**). After this, the pattern was transferred to the elastic PDMS (Sylgard®, Dow Corning) via water-soluble tape (3M, US) as described in **Figure 6.9(e)**. The PDMS has a thickness of 160 µm and the pre-polymer/ cross-link ratio of 10:1. The tape was dissolved in deionised water overnight to ensure no residue was left.

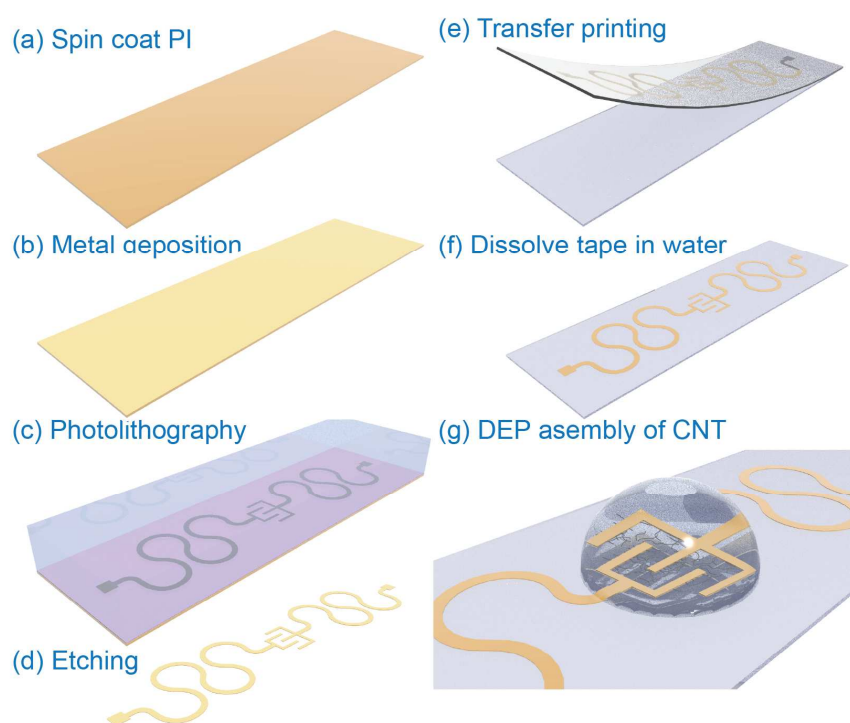


Figure 6.9: Fabrication steps related to strain sensor: (a) spin coating of PI solution, (b) metal deposition on PI film, (c) photolithography patterning of stretchable interconnects, (d) etching, (e) transferring from Si carrier wafer to PDMS substrate (d) dissolving transfer tape in DI water and (g) DEP assembly of CNTs.

## Chapter 6

## c. Sensor Design and Assembly of CNTs

The sensitive part of the strain sensor is designed to have an interdigitated structure with three fingers at a gap of 50  $\mu\text{m}$  (**Figure 6.6**). This is connected to a pair of serpentine-shaped stretchable interconnects with a curved arc of  $260^\circ$ , to obtain high stretchability. The CNTs used in this work were purchased from Sigma-Aldrich. The diameter of the used CNTs is  $43 \pm 4$  nm, which was measured with AFM (**Figure 6.10**). The length of CNTs was estimated through SEM images to be around 2-3  $\mu\text{m}$ . They are dispersed in water with a concentration of 1 mg/mL. The original solution is highly concentrated, and it was diluted in ethanol to obtain a concentration of 1% with a homogeneous dispersion by 5 seconds probe sonication. Afterwards, CNTs were drop-casted on the interdigitated structure and DEP was performed by applying an AC signal. To assemble the CNTs with a homogenous distribution and tune the electrical conductivity to a required level, AC signal with different peak-to-peak voltage (5 V, 10 V, and 15 V) and frequencies (10 kHz, 100kHz, 1 MHz and 10 MHz) were used. The DEP force can be represented as [239]:

$$F_{DEP} = \frac{3}{2} \pi r^2 \epsilon_m \text{Re}\{\tilde{f}_{CM}\} \int_{x_0}^{x_L} \sqrt{1 + (f'(x))^2} |\nabla E|^2 dx \quad (6.2)$$

Where  $r$  is the radius of CNT,  $\epsilon_m$  is permittivity of CNT,  $E$  is the magnitude of AC electric field,  $\tilde{f}_{CM}$  is the Clausius-Mossotti factor, which depends on the permittivity, conductivity of CNTs and the suspending solvent and the frequency of the electrical field. Under a

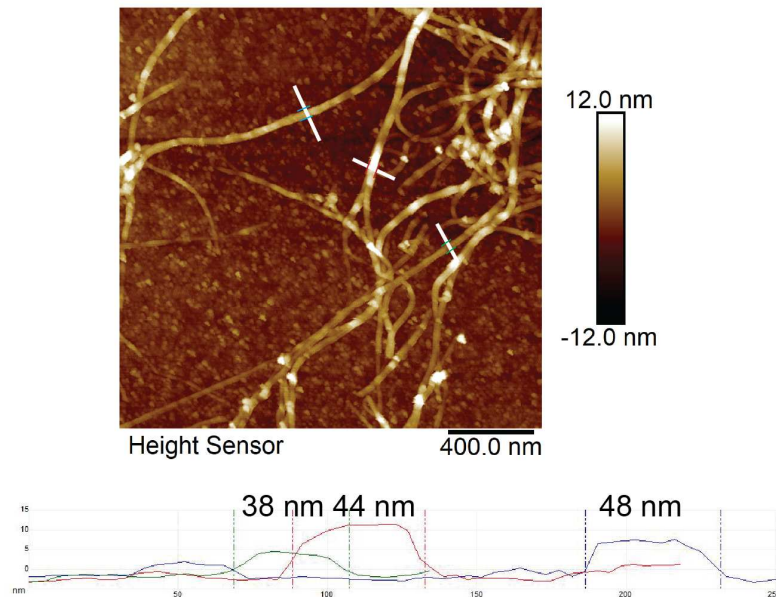


Figure 6.10: AFM measurement of assembled CNT network with three locations' width measurement.

## Chapter 6

constant AC frequency of 1 MHz, the peak-to-peak voltage ( $V_{pp}$ ) is swept from 5, 10 to 15 V. The resistance across the CNT network and scanning electron microscopic (SEM) image were observed. As depicted in **Figure 6.11**, the overall resistance drops dramatically with an increase in  $V_{pp}$  voltage with a reduction in variation. In terms of AC frequencies, a

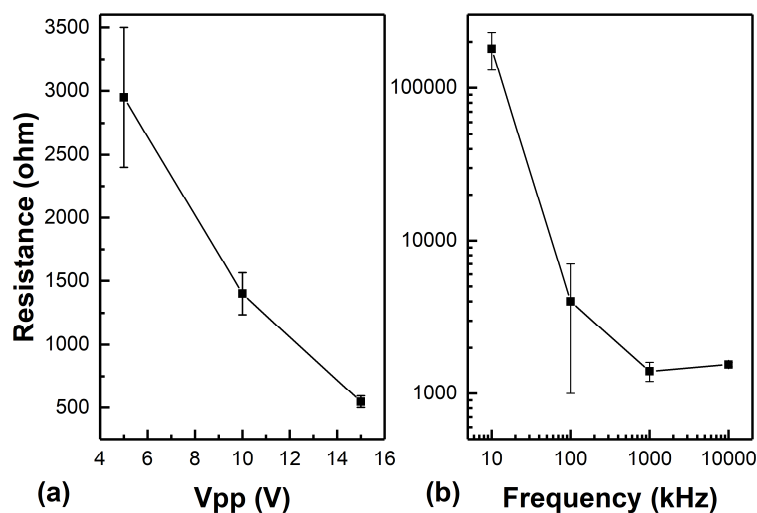


Figure 6.11: Variation in the resistance of DEP assembled CNT network with respect to (a) peak-to-peak voltage ( $V_{pp}$ ) under constant AC frequency of 1 MHz, and (b) AC frequency under constant  $V_{pp}$  voltage of 10 V.

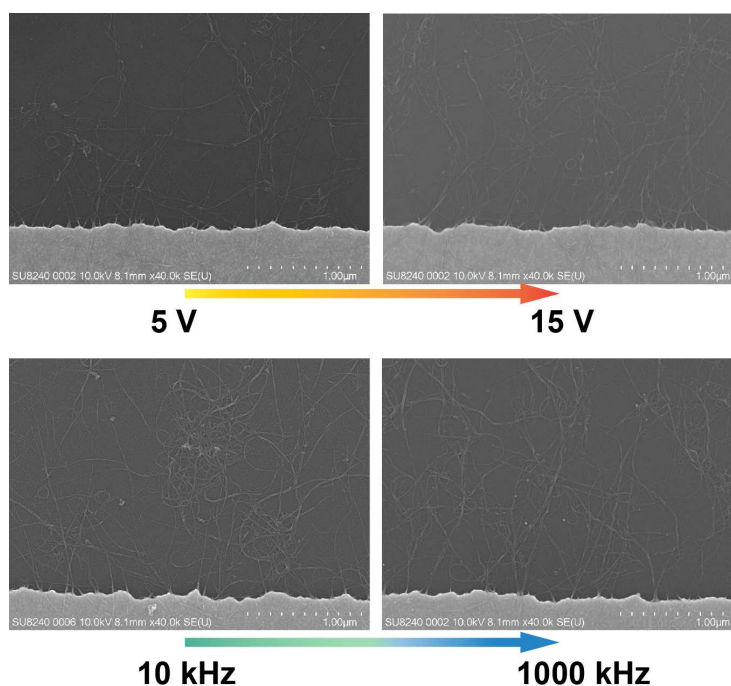


Figure 6.12: SEM images of DEP assembled CNT network near electrode with variations in  $V_{pp}$  and AC frequencies.

## Chapter 6

peak can be found in the trend of resistance variation at 1 MHz. The SEM images (**Figure 6.12**) also exhibit a similar trend. With a lower  $V_{pp}$ , fewer CNTs are observed to bridge the electrode. It is roughly estimated from the SEM images that 3 assembled CNT/ $\mu\text{m}^2$  was found at 5 V peak-to-peak voltage and it is increased to 5.67 assembled CNT/ $\mu\text{m}^2$  at 15 V. The CNTs tend to agglomerate under 10 kHz and for this reason higher frequencies were used. Although higher  $V_{pp}$  voltage leads to a lower resistance ( $<500\ \Omega$ ), 10 V is selected as  $V_{pp}$  because the resistance of Au-PI electrode is in the range of  $50\ \Omega$ . To exclude the effect of the resistance variation of the electrode, the resistance of the strain sensor is tuned to the  $\text{k}\Omega$  range, as measured in **Figure 6.11(a)**. After the DEP of CNTs, another layer of PDMS was spin-coated to protect the CNT network.

In this work, the elastomer PDMS was chosen as the substrate for the strain sensor instead of Ecoflex. The reason behind is due to the stronger adhesion was found between CNT and PDMS compared with CNT and Ecoflex. This adhesion is attributed to the different interaction energy level between CNT and the polymeric substrate. Evidence has been found out regarding this issue. The DEP assembled CNT network exhibits the resistance of  $1.4\ \text{k}\Omega$  before the encapsulation with Ecoflex. However, after the encapsulation, the resistance increased to  $40\ \text{k}\Omega$ . This variation in the resistance of the CNT network's reflects the disturbance that is provided by the viscous polymer solution. The PDMS encapsulation also influences the original resistance of the CNT network, but the variation in resistance is lower than the Ecoflex encapsulation. Comparing the sensor performance between the strain sensor on the PDMS substrate and the Ecoflex substrate, the sensor on the Ecoflex substrate exhibits

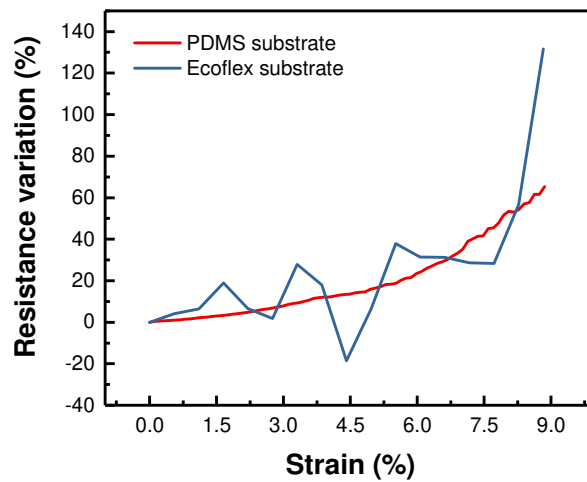


Figure 6.13: Variation in the resistance of the strain sensor on the PDMS substrate and Ecoflex substrate under applied strain.

## Chapter 6

a less stable trend of resistance variation, as depicted in **Figure 6.13**. The observed oscillating behaviour from the sensors on Ecoflex substrate can be attributed to the variation in contact resistance, which also results from the poor adhesion.

### d. Results and discussion

The developed strain sensor was integrated with the soft robotic finger and characterised under custom-developed uniaxial stretching setup. The working principle of the sensor is based on changes in the resistance of the CNT network upon external strain. It is a piezo-resistive type sensor. During measurement, two stepper motors were synchronised to move apart with the overall resistance continuously recorded by a multimeter (Agilent 34461A). The bending of the developed soft robotic finger can be actuated up to a radius of 23 mm which roughly corresponds to 16% strain finger and therefore the strain sensor was characterised up to 16% stretching. As illustrated in **Figure 6.14(a)**, the sensor resistance follows monotonic growth up to 9% strain (strain speed of 50  $\mu\text{m/s}$ ). An increase of 61.6% in resistance is observed with an external strain of 9% (inset of **Figure 6.14(a)**). Afterwards, an exponential growth from 100 to 1300% in resistance can be observed between 9% to 11% strain. Then the variation in resistance is saturated to about 1500% range. A hysteresis effect in the sensor is also noticed after releasing the sensor from 16% to 4% strain. However, the resistance of the sensor was able to return to the original value. Five cycles (out of ten cycles) of up to 11% strain are represented in **Figure 6.14(b)**. The variation in resistance is attributed

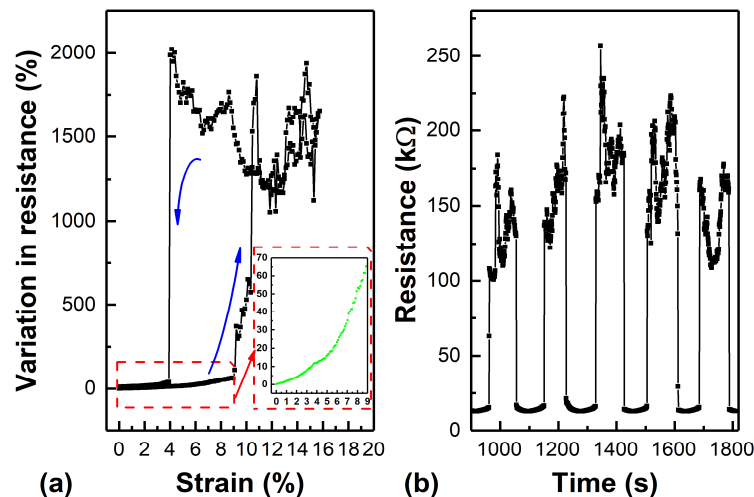


Figure 6.14: (a) Variation in the resistance of sensor under applied strain and (b) the resistance of sensor under five cycles of 11% strain.

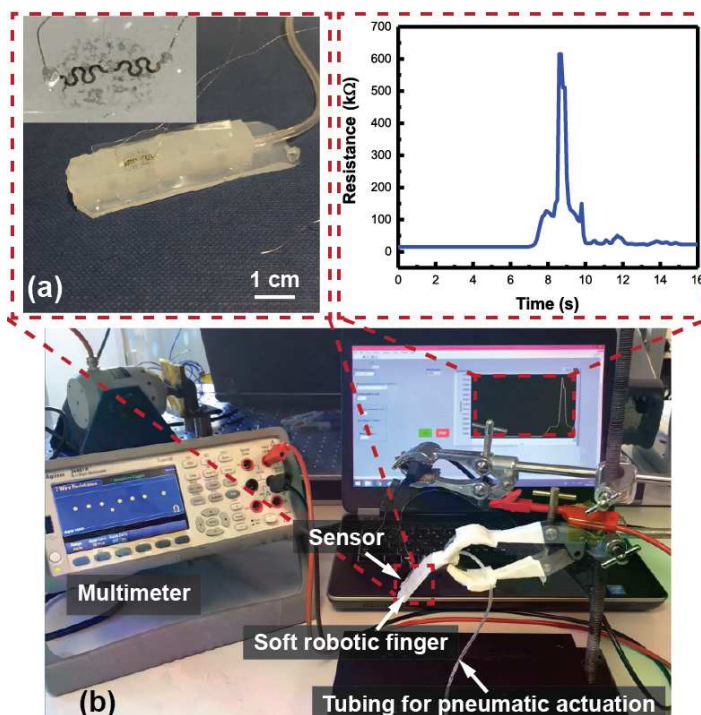


Figure 6.15: Real-time monitoring of the bending of soft robotic finger with integrated CNT based strain sensor.

to the morphology change in CNT network, contact resistance variation between CNT and Au electrode and adjacent CNTs [240], [241].

Finally, the stretchable strain sensor was integrated on the fabricated soft robotic finger as shown in **Figure 6.15(a)**. The pneumatic actuation of the soft robotic finger was realised by connecting to the rubber blowing ball. While compressing the ball, the finger starts to bend with a real-time resistance variation recorded in the Labview programme (**Figure 6.15(b)**). After the releasing of the finger back to its original shape, the resistance is back to the initial value. This demonstrates the capability of the developed strain sensor to facilitate the movement control of the soft robotic finger, as the resistance values of the integrated sensor can be used to monitor the bending of the robotic finger and possibly alarm the users before the soft robotics finger is damaged.

### 6.2.3 Conclusion

This work successfully demonstrated a soft robotic finger integrated with CNT-based stretchable strain sensor. The strain sensor has been characterised by a full working range of soft finger and an increase of 61.6% in resistance is observed with an external strain of 9%.

## Chapter 6

The variation of resistance can reach 1300% in the 9-11% strain range and is saturated to approximately 1500% above 12% strain. The variation in resistance was also noted after the integration of sensors on the soft finger and this demonstrates the possibility of using sensory feedback to control the pneumatic actuation of the finger. The work shows that by integrating different types of sensors it will be possible to use soft fingers to identify the size, hardness, temperature and chemical structure of the objects.

## Summary

This chapter demonstrated two applications of stretchable interconnects integrated with sensors. The first application is the stretchable sweat pH monitoring system, which is based on an electrochemical pH sensor connected with a pair of stretchable interconnects and a stretchable RFID antenna. The connection between the pH sensor and the interconnects is realised through the silver adhesive and further secured by epoxy glue. In this method, the sensor connected with stretchable interconnects can withstand maximum 53% strain, which is lower than the stretchable interconnect without sensors ( $77.7 \pm 23.3\%$ ) as presented in **Chapter 5**. In addition to the restriction from encapsulation, the stretchability of interconnects is limited by the adhesive for sensor connection. The achieved stretchable sensing system can be used for wearable sweat monitoring, as generally human skin experiences an average strain of 30%. Another application is the stretchable strain sensor for the soft robotic finger. In this application, the strain sensor is integrated with interconnects through dielectrophoresis assembly of CNTs on the interdigitated electrode. Here, no extra adhesives are required for sensor's assembly. The variation of contact resistance between CNTs and electrode also contributes to the strain sensitivity of the developed sensor. This stretchable sensing system works in the strain range between 0-10% with a high strain sensitivity. Such a system is aimed to help soft robotics detect the size, hardness, and temperature of the holding objects.



## Chapter 7 Conclusion and future perspective

### 7.1 Conclusion

In this work, three types of stretchable interconnects have been developed. They include the metal (Au)-conductive polymer (PEDOT:PSS) hybrid film, graphite-PEDOT:PSS composite and Au-PI dual-layered interconnects. The achieved interconnects are comparable with the major materials for stretchable interconnects in the state-of-the-art, as illustrated in **Figure 7.1**. Conductive polymer PEDOT:PSS has been widely reported due to its potential for stretchable interconnects. However, due to its high sensitivity to water and other chemicals, it is challenging to pattern the PEDOT:PSS and process the next layers (i.e. semiconductor, dielectric) through an aqueous process. The hybrid structure with an additional metallic film (i.e. Au) can resolve this issue. The additional metallic film helps the hybrid film not only increase the electrical conductivity but also act as a protective encapsulation to isolate PEDOT:PSS film from an aqueous environment. The achieved interconnects can reach 72% with a resistance variation below 1%, which reveals a superior performance compared to the reported results.

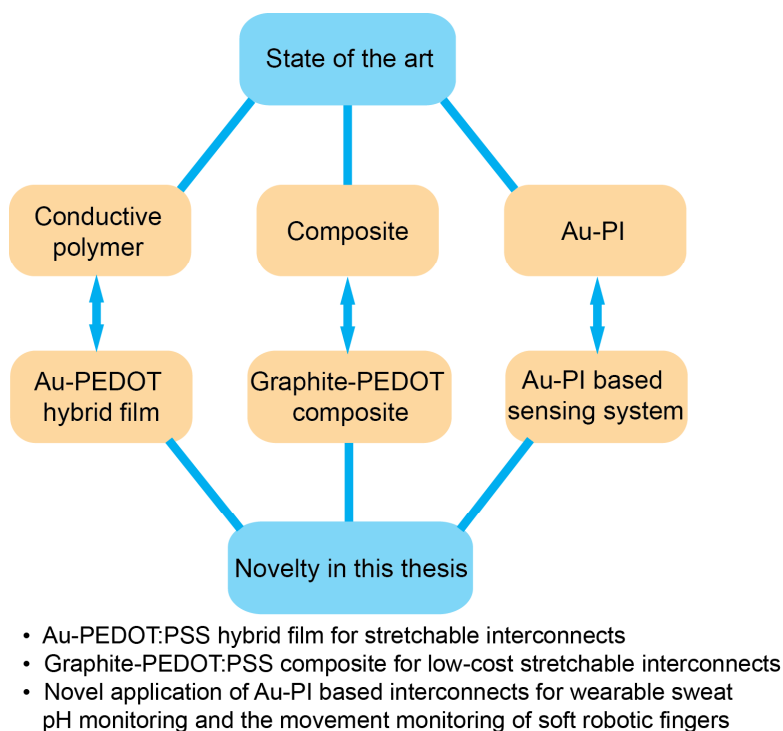


Figure 7.1: Illustration of the major materials presented in Chapter 2 for stretchable interconnects and the comparison with the developed stretchable interconnects in the thesis.



Composites, as one of the widely used conductors for stretchable interconnects, exhibit the high stretchability and high electrical conductivity due to the soft polymer matrix and high aspect ratio of conductive fillers, respectively. One of the drawbacks is their high contact resistance from the dielectric polymer matrix. The achieved composite has graphite flakes as conductive fillers and PEDOT:PSS as a polymer matrix, which results in a low contact resistance ( $35\ \Omega$ ) and low sheet resistance ( $695.7\ \Omega/\square$ ). The stretchability of such composite can reach 80%, which is higher than the reported carbon-based composite. Currently, the composite was deposited on the PDMS substrate through spin-coating and manually dicing. Common strategies for composite patterning include screen-printing, moulding, and contact-printing etc. Further work will be focused on patterning the graphite-PEDOT:PSS composite through a screen-printing process, as it is compatible with the industrial fabrication process.

Au-PI dual-layered has been reported to be used as stretchable interconnects. In this thesis, the interconnects were characterised in both DC and AC ranges in order to integrate with a wider variety of sensors. After characterising different geometrical designs of interconnects, the serpentine-shaped design with arc curvature of 260 degree exhibits the best electro-mechanical performance in both DC and AC ranges. Without the encapsulation of PDMS, the achieved interconnect can be stretched up to 101% with 0.2% variation in DC resistance and a 1% variation of the Q factor in AC range. The encapsulation for this kind of interconnect is expected to be a reduction of 16% in stretchability, due to the limitation of interconnects distortion movement. The fabricated interconnects with optimised geometrical design were demonstrated to integrate with an electrochemical sensor and a strain sensor. The prior stretchable electronic system can be applied to wirelessly monitor the sweat pH and the latter system was applied to a soft robotic finger for monitoring its bending radius.

### General comparison between stretchable interconnects with different materials

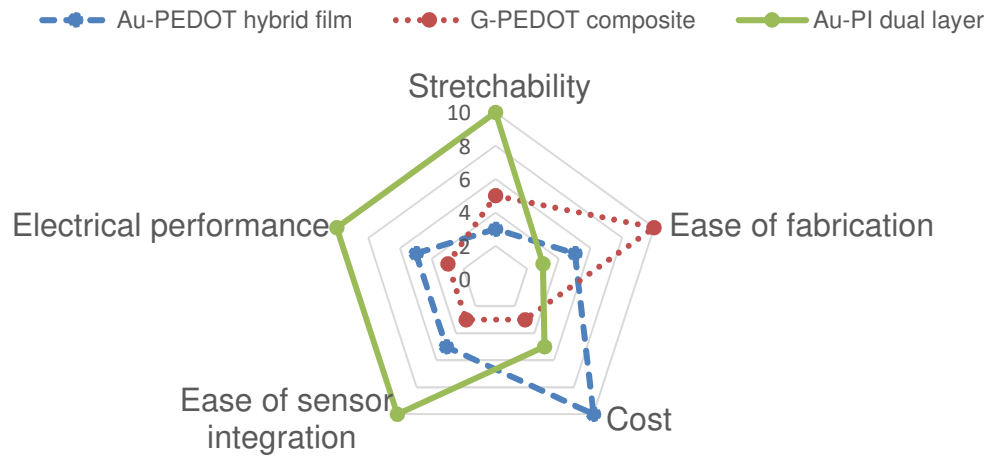


Figure 7.2: General comparison between stretchable interconnects with different materials.

To generally estimate the three stretchable interconnects developed in this thesis, a radar chart is concluded in **Figure 7.2**. Five parameters, including electrical performance, stretchability, ease of fabrication, cost, and ease of sensor integration, are discussed. In terms of stretchability, graphite-PEDOT:PSS composite and Au-PEDOT:PSS hybrid film show a similar degree of stretchability. The Au-PI dual-layered interconnect reveals a higher stretchability. In addition, its electrical performance is more stable compared to the other two interconnects. However, the fabrication process of Au-PI interconnects is the most complicated one. It requires photolithography, wet etch, dry etch and transfer printing steps. These steps cost relatively high and consume longer time. On the other hand, the fabrication of the composite is much simpler. From the step of solution processing, graphite mixing, depositing on the substrate to curing, the overall process takes less than one hour. However, the drawback of composite interconnects is its significant variation in resistance under strain. The Au-PEDOT:PSS hybrid film shares the similar fabrication process with Au-PI interconnects, which requires the photolithography and etching steps, but it does not need an extra step of transferring to the soft substrate. If only the contact resistance is considered for integrating sensors, the interconnects with the metallic contact pad, which refer to Au-PEDOT:PSS hybrid film and Au-PI interconnects, have much lower contact resistance compared to the composite.

In order to integrate multifunctional sensing elements into a stretchable system, the scalability to fabricate the interconnects plays an important role. The microfabrication

process is the option for interconnects' fabrication with high resolutions in wafer scale. However, the fabrication of Au-PI interconnects is restricted to a limited area due to the transfer process, which highly depends on the size of the assistive tape. In this case, only the Au-PEDOT:PSS hybrid interconnects can be fabricated through a wafer-level process.

## 7.2 Future perspective

With the development of printing technology, the high-resolution printing can be realised through inkjet printing and even super inkjet printing. Medium resolution can be obtained by screen printing. With these technologies, the development of composite-based ink can be promising. The current graphite-PEDOT:PSS composite has certain limits and it can be used for screen printing due to the grain size of graphite ( $\sim 45\ \mu\text{m}$ ). Based on its promising electro-mechanical response to strain, further improvements in reducing the grain size of the composite are planned.

Further work also aims to integrate stretchable interconnects with multi-sensing modulus in a higher sensing density. This includes expanding the sweat pH monitoring system into a sweat multi-sensing system and a soft robotic finger multi-sensing system. The more effective method has to be explored for multi-sensors' integration. Currently, the sensors are integrated individually, which consume a long time and reduce the reproducibility of the process. A wafer-level integration for the multi-sensing system is necessary to realise the next-generation of the stretchable electronic system.

## Bibliography

- [1] H. Lee, T. K. Choi, Y. B. Lee, H. R. Cho, R. Ghaffari, L. Wang, H. J. Choi, T. D. Chung, N. Lu, T. Hyeon, S. H. Choi, and D.-H. Kim, "A graphene-based electrochemical device with thermoresponsive microneedles for diabetes monitoring and therapy," *Nat. Nanotechnol.*, vol. 11, pp. 566–572, 2016.
- [2] D.-H. Kim, N. Lu, R. Ma, Y.-S. Kim, R.-H. Kim, S. Wang, J. Wu, S. M. Won, H. Tao, A. Islam, K. J. Yu, T. Kim, R. Chowdhury, M. Ying, L. Xu, M. Li, H.-J. Chung, H. Keum, M. McCormick, P. Liu, Y.-W. Zhang, F. G. Omenetto, Y. Huang, T. Coleman, and J. A. Rogers, "Epidermal Electronics," *Science (80-. )*, vol. 333, pp. 838–844, 2011.
- [3] R. C. Webb, A. P. Bonifas, A. Behnaz, Y. Zhang, K. J. Yu, H. Cheng, M. Shi, Z. Bian, Z. Liu, Y.-S. Kim, W.-H. Yeo, J. S. Park, J. Song, Y. Li, Y. Huang, A. M. Gorbach, and J. A. Rogers, "Ultrathin conformal devices for precise and continuous thermal characterization of human skin," *Nat. Mater.*, vol. 12, no. 10, pp. 938–44, 2013.
- [4] W. Dang, L. Manjakkal, W. T. Navaraj, L. Lorenzelli, V. Vinciguerra, and R. Dahiya, "Stretchable Wireless System for Sweat pH Monitoring," *Biosens. Bioelectron.*, vol. 107, pp. 192–202, 2018.
- [5] T. Yamada, Y. Hayamizu, Y. Yamamoto, Y. Yomogida, A. Izadi-Najafabadi, D. N. Futaba, and K. Hata, "A stretchable carbon nanotube strain sensor for human-motion detection," *Nat. Nanotechnol.*, vol. 6, no. 5, pp. 296–301, 2011.
- [6] T. Il Lee, W. S. Jang, E. Lee, Y. S. Kim, Z. L. Wang, H. K. Baik, and J. M. Myoung, "Ultrathin self-powered artificial skin," *Energy Environ. Sci.*, vol. 7, no. 12, pp. 3994–3999, 2014.
- [7] P. K. Yang, L. Lin, F. Yi, X. Li, K. C. Pradel, Y. Zi, C. I. Wu, J. H. He, Y. Zhang, and Z. L. Wang, "A Flexible, Stretchable and Shape-Adaptive Approach for Versatile Energy Conversion and Self-Powered Biomedical Monitoring," *Adv. Mater.*, vol. 27, no. 25, pp. 3817–3824, 2015.
- [8] R. Liu, X. Kuang, J. Deng, Y. C. Wang, A. C. Wang, W. Ding, Y. C. Lai, J. Chen, P. Wang, Z. Lin, H. J. Qi, B. Sun, and Z. L. Wang, "Shape Memory Polymers for Body Motion Energy Harvesting and Self-Powered Mechanosensing," *Adv. Mater.*, vol. 30, no. 8, p. 1705195 (1-8), 2018.
- [9] H. Jinno, K. Fukuda, X. Xu, S. Park, Y. Suzuki, M. Koizumi, T. Yokota, I. Osaka, K. Takimiya, and T. Someya, "Stretchable and waterproof elastomer-coated organic photovoltaics for washable electronic textile applications," *Nat. Energy*, vol. 2, no. 10, pp. 780–785, 2017.
- [10] J. Kim, M. Lee, H. J. Shim, R. Ghaffari, H. R. Cho, D. Son, Y. H. Jung, M. Soh, C. Choi, S. Jung, K. Chu, D. Jeon, S.-T. Lee, J. H. Kim, S. H. Choi, T. Hyeon, and D.-H. Kim, "Stretchable silicon nanoribbon electronics for skin prosthesis," *Nat. Commun.*, vol. 5, p. 5747, 2014.

- [11] C. G. Nunez, W. T. Navaraj, E. O. Polat, and R. Dahiya, “Energy-Autonomous, Flexible, and Transparent Tactile Skin,” *Adv. Funct. Mater.*, vol. 27, no. 18, p. 1606287, 2017.
- [12] Q. Hua, J. Sun, H. Liu, R. Bao, R. Yu, J. Zhai, C. Pan, and Z. L. Wang, “Skin-inspired highly stretchable and conformable matrix networks for multifunctional sensing,” *Nat. Commun.*, vol. 9, p. 244 (1-11), 2018.
- [13] T. Sekitani and T. Someya, “Stretchable organic integrated circuits for large-area electronic skin surfaces,” *MRS Bull.*, vol. 37, no. 03, pp. 236–245, 2012.
- [14] R.-H. Kim, D.-H. Kim, J. Xiao, B. H. Kim, S.-I. Park, B. Panilaitis, R. Ghaffari, J. Yao, M. Li, Z. Liu, V. Malyarchuk, D. G. Kim, A.-P. Le, R. G. Nuzzo, D. L. Kaplan, F. G. Omenetto, Y. Huang, Z. Kang, and J. A. Rogers, “Waterproof AllnGaP optoelectronics on stretchable substrates with applications in biomedicine and robotics,” *Nat. Mater.*, vol. 9, no. 11, pp. 929–37, 2010.
- [15] S.-I. Park, Y. Xiong, R.-H. Kim, P. Elvikis, M. Meitl, D.-H. Kim, J. Wu, J. Yoon, C.-J. Yu, Z. Liu, Y. Huang, K. Hwang, P. Ferreira, X. Li, K. Choquette, and J. A. Rogers, “Printed assemblies of inorganic light-emitting diodes for deformable and semitransparent displays,” *Science (80-. )*, vol. 325, pp. 977–981, 2009.
- [16] T. Sekitani, H. Nakajima, H. Maeda, T. Fukushima, T. Aida, K. Hata, and T. Someya, “Stretchable active-matrix organic light-emitting diode display using printable elastic conductors,” *Nat. Mater.*, vol. 8, no. 6, pp. 494–499, 2009.
- [17] B. You, Y. Kim, B.-K. Ju, and J.-W. Kim, “Highly stretchable and waterproof electroluminescence device based on superstable stretchable transparent electrode,” *ACS Appl. Mater. Interfaces*, vol. 9, no. 6, pp. 5486–5494, 2017.
- [18] T. Chang, Y. Tanabe, C. C. Wojcik, A. C. Barksdale, S. Doshay, Z. Dong, H. Liu, M. Zhang, Y. Chen, Y. Su, T. H. Lee, J. S. Ho, and J. A. Fan, “A General Strategy for Stretchable Microwave Antenna Systems using Serpentine Mesh Layouts,” *Adv. Funct. Mater.*, vol. 27, p. 1703059 (1-8), 2017.
- [19] M. Kubo, X. Li, C. Kim, M. Hashimoto, B. J. Wiley, D. Ham, and G. M. Whitesides, “Stretchable microfluidic radiofrequency antennas,” *Adv. Mater.*, vol. 22, no. 25, pp. 2749–2752, 2010.
- [20] M. Jobs, K. Hjort, A. Rydberg, and Z. Wu, “A tunable spherical cap microfluidic electrically small antenna,” *Small*, vol. 9, no. 19, pp. 3230–3234, 2013.
- [21] Y. Huang, Y. Wang, L. Xiao, H. Liu, W. Dong, and Z. Yin, “Microfluidic serpentine antennas with designed mechanical tunability,” *Lab Chip*, vol. 14, no. 21, pp. 4205–4212, 2014.
- [22] W. Arden, M. Brillouët, P. Cogez, M. Graef, B. Huizing, and R. Mahnkopf, “‘More-than-Moore’ White Paper.”

- [23] X. Hui and E. C. Kan, "Monitoring vital signs over multiplexed radio by near-field coherent sensing," *Nat. Electron.*, vol. 1, pp. 74–78, 2017.
- [24] L. Y. Chen, B. C.-K. Tee, A. L. Chortos, G. Schwartz, V. Tse, D. J. Lipomi, H.-S. P. Wong, M. V McConnell, and Z. Bao, "Continuous wireless pressure monitoring and mapping with ultra-small passive sensors for health monitoring and critical care.," *Nat. Commun.*, vol. 5, p. 5028, 2014.
- [25] S. Nakata, T. Arie, S. Akita, and K. Takei, "Wearable, Flexible, and Multifunctional Healthcare Device with an ISFET Chemical Sensor for Simultaneous Sweat pH and Skin Temperature Monitoring," *ACS Sensors*, vol. 2, no. 3, pp. 443–448, 2017.
- [26] W. Gao, S. Emaminejad, H. Y. Y. Nyein, S. Challa, K. Chen, A. Peck, H. M. Fahad, H. Ota, H. Shiraki, D. Kiriya, D.-H. Lien, G. A. Brooks, R. W. Davis, and A. Javey, "Fully integrated wearable sensor arrays for multiplexed in situ perspiration analysis," *Nature*, vol. 529, no. 7587, pp. 509–514, 2016.
- [27] World Health Organization, "mHealth: New horizons for health through mobile technologies," *Observatory*, vol. 3, no. June, pp. 66–71, 2011.
- [28] J. Shintake, S. Rosset, B. Schubert, D. Floreano, and H. Shea, "Versatile Soft Grippers with Intrinsic Electrodehesion Based on Multifunctional Polymer Actuators," *Adv. Mater.*, vol. 28, no. 2, pp. 231–238, 2016.
- [29] K. C. Galloway, K. P. Becker, B. Phillips, J. Kirby, S. Licht, D. Tchernov, R. J. Wood, and D. F. Gruber, "Soft Robotic Grippers for Biological Sampling on Deep Reefs," *Soft Robot.*, vol. 3, no. 1, pp. 23–33, 2016.
- [30] K. Hayward, G. James, and X. He, "Stretchable Electronics 2018-2028 (IDTechEx Research)."
- [31] C. Pylatiuk, A. Kargov, and S. Schulz, "Design and Evaluation of a Low-Cost Force Feedback System for Myoelectric Prosthetic Hands," *JPO J. Prosthetics Orthot.*, vol. 18, no. 2, pp. 57–61, 2006.
- [32] T. Yoshikai, H. Fukushima, M. Hayashi, and M. Inaba, "Development of soft stretchable knit sensor for humanoids' whole-body tactile sensibility," in *9th IEEE-RAS International Conference on Humanoid Robots, HUMANOIDS09*, 2009, pp. 624–631.
- [33] Y. Chen, M. Yu, H. A. Bruck, and E. Smela, "Stretchable touch-sensing skin over padding for co-robots," *Smart Mater. Struct.*, vol. 25, no. 5, p. 055006 (1-16), 2016.
- [34] R. S. Dahiya and M. Valle, "Robotic tactile sensing: technologies and system," in *Springer Science + Business Media, Dordrecht*, Springer Science & Business Media, 2013, pp. 1–248.
- [35] D.-H. Kim, N. Lu, R. Ghaffari, Y.-S. Kim, S. P. Lee, L. Xu, J. Wu, R.-H. Kim, J. Song, Z. Liu, J. Viventi, B. de Graff, B. Elolampi, M. Mansour, M. J. Slepian, S.

- Hwang, J. D. Moss, S.-M. Won, Y. Huang, B. Litt, and J. A. Rogers, "Materials for multifunctional balloon catheters with capabilities in cardiac electrophysiological mapping and ablation therapy," *Nat. Mater.*, vol. 10, no. 4, pp. 316–23, 2011.
- [36] S. Wang, J. Xu, W. Wang, G.-J. N. Wang, R. Rastak, F. Molina-Lopez, J. W. Chung, S. Niu, V. R. Feig, J. Lopez, T. Lei, S.-K. Kwon, Y. Kim, A. M. Foudeh, A. Ehrlich, A. Gasperini, Y. Yun, B. Murmann, J. B.-H. Tok, and Z. Bao, "Skin electronics from scalable fabrication of an intrinsically stretchable transistor array," *Nature*, vol. 555, pp. 83–88, 2018.
- [37] S. P. Lacour, J. Jones, S. Wagner, T. Li, and Z. Suo, "Stretchable Interconnects for Elastic Electronic Surfaces," *Proceedings of the IEEE*, vol. 93, no. 8, pp. 1459–1467, 2005.
- [38] A. E. Hess-Dunning, D. J. Tyler, and C. A. Zorman, "STRETCHABLE THIN-FILM METAL STRUCTURES ON A STIMULI-RESPONSIVE POLYMER NANOCOMPOSITE FOR MECHANICALLY-DYNAMIC MICROSYSTEMS," in *Transducers 2013, Barcelona, SPAIN*, 2013, pp. 2229–2232.
- [39] H. Stoyanov, M. Kollosche, S. Risse, R. Waché, and G. Kofod, "Soft conductive elastomer materials for stretchable electronics and voltage controlled artificial muscles," *Adv. Mater.*, vol. 25, no. 4, pp. 578–583, 2013.
- [40] D. J. Lipomi, J. A. Lee, M. Vosgueritchian, B. C.-K. Tee, J. A. Bolander, and Z. Bao, "Electronic Properties of Transparent Conductive Films of PEDOT:PSS on Stretchable Substrates," *Chem. Mater.*, vol. 24, no. 2, pp. 373–382, 2012.
- [41] J. Liang, K. Tong, and Q. Pei, "A Water-Based Silver-Nanowire Screen-Print Ink for the Fabrication of Stretchable Conductors and Wearable Thin-Film Transistors," *Adv. Mater.*, vol. 28, pp. 5986–5996, 2016.
- [42] J. Suikkola, T. Björninen, M. Mosallaei, T. Kankkunen, P. Iso-ketola, L. Ukkonen, J. Vanhala, and M. Mäntysalo, "Screen-Printing Fabrication and Characterization of Stretchable Electronics," *Sci. Rep.*, vol. 6, p. 25784 (1-8), 2016.
- [43] S. H. Jeong, S. Zhang, K. Hjort, J. Hilborn, and Z. Wu, "PDMS-Based Elastomer Tuned Soft, Stretchable, and Sticky for Epidermal Electronics," *Adv. Mater.*, vol. 28, pp. 5830–5836, 2016.
- [44] B. B. Plovie, Y. Yang, J. Guillaume, S. Dunphy, K. Dhaenens, S. Van Put, T. Vervust, F. Bossuyt, and J. Vanfleteren, "Arbitrarily Shaped 2.5D Circuits using Stretchable Interconnects Embedded in Thermoplastic Polymers," *Adv. Eng. Mater.*, vol. 19, no. 8, p. 1700032 (1-8), 2017.
- [45] G. A. Salvatore, J. Sülzle, F. D. Valle, G. Cantarella, F. Robotti, P. Jokic, S. Knobelspies, A. Daus, L. Büthe, L. Petti, N. Kirchgessner, R. Hopf, M. Magno, and G. Tröster, "Biodegradable and Highly Deformable Temperature Sensors for the Internet of Things," *Adv. Funct. Mater.*, vol. 27, no. 35, p. 1702390 (1-10), 2017.
- [46] Dow Corning, "Product Information: Dow Corning 184 Silicone Elastomer," 2010.

- [47] I. D. Johnston, D. K. McCluskey, C. K. L. Tan, and M. C. Tracey, "Mechanical characterization of bulk Sylgard 184 for microfluidics and microengineering," *J. Micromechanics Microengineering*, vol. 24, no. 3, p. 0350117 (1-7), 2014.
- [48] A. Blau, A. Murr, S. Wolff, E. Sernagor, P. Medini, G. Iurilli, C. Ziegler, and F. Benfenati, "Flexible, all-polymer microelectrode arrays for the capture of cardiac and neuronal signals," *Biomaterials*, vol. 32, no. 7, pp. 1778–1786, 2011.
- [49] K. Tybrandt, D. Khodagholy, B. Dielacher, F. Stauffer, A. F. Renz, G. Buzsáki, and J. Vörös, "High-Density Stretchable Electrode Grids for Chronic Neural Recording," *Adv. Mater.*, vol. 30, no. 15, p. 1706520 (1-7), 2018.
- [50] A. Carlson, A. M. Bowen, Y. Huang, R. G. Nuzzo, and J. A. Rogers, "Transfer printing techniques for materials assembly and micro/nanodevice fabrication," *Adv. Mater.*, vol. 24, no. 39, pp. 5284–5318, 2012.
- [51] Y. Gao, H. Ota, E. W. Schaler, K. Chen, A. Zhao, W. Gao, H. M. Fahad, Y. Leng, A. Zheng, F. Xiong, C. Zhang, L.-C. Tai, P. Zhao, R. S. Fearing, and A. Javey, "Wearable Microfluidic Diaphragm Pressure Sensor for Health and Tactile Touch Monitoring," *Adv. Mater.*, vol. 29, no. 39, p. (1-8) 1701985, 2017.
- [52] I. Vroman and L. Tighzert, "Biodegradable polymers," *Materials (Basel)*, vol. 2, no. 2, pp. 307–344, 2009.
- [53] J. C. Case, E. L. White, and R. K. Kramer, "Soft Material Characterization for Robotic Applications," *Soft Robot.*, vol. 2, no. 2, pp. 80–87, 2015.
- [54] R. Mieczkowski, "Solubility parameter components of some polyurethanes," *Eur. Polym. J.*, vol. 28, no. 1, pp. 53–55, 1992.
- [55] Y. Qu, T. Nguyen-Dang, A. G. Page, W. Yan, T. Das Gupta, G. M. Rotaru, R. M. Rossi, V. D. Favrod, N. Bartolomei, and F. Sorin, "Superelastic Multimaterial Electronic and Photonic Fibers and Devices via Thermal Drawing," *Adv. Mater.*, vol. 30, no. 27, p. 1707251 (1-8), 2018.
- [56] H. Microsystems, "Datasheet PI-2545," 2009.
- [57] J. J. Qin, T. S. Chung, and Y. Cao, "Solvent selection for manufacture of fluorinated polyimide composite membranes," *Desalination*, vol. 193, pp. 8–13, 2006.
- [58] P. Du, X. Lin, and X. Zhang, "Dielectric Constants of PDMS Nanocomposites using Conducting Polymer Nanowires," in *IEEE Transducers*, 2011, pp. 645–648.
- [59] J. N. Lee, C. Park, and G. M. Whitesides, "Solvent Compatibility of Poly(dimethylsiloxane)-Based Microfluidic Devices," *Anal. Chem.*, vol. 75, no. 23, pp. 6544–6554, 2003.
- [60] M. Zhai and G. B. McKenna, "Elastic modulus and surface tension of a polyurethane rubber in nanometer thick films," *Polym. (United Kingdom)*, vol. 55, no. 11, pp. 2725–



2733, 2014.

- [61] H. Koerner, W. Liu, M. Alexander, P. Mirau, H. Dowty, and R. a. Vaia, “Deformation–morphology correlations in electrically conductive carbon nanotube—thermoplastic polyurethane nanocomposites,” *Polymer (Guildf)*, vol. 46, no. 12, pp. 4405–4420, May 2005.
- [62] M. Pavlova and M. Draganova, “Biocompatible and biodegradable polyurethane polymers,” *Biomaterials*, vol. 14, no. 13, pp. 1024–1029, 1993.
- [63] Datasheet, “PU chemical resistance: general information.”.
- [64] R. A. Weiss, A. Sen, L. A. Pottick, and C. L. Willis, “Block copolymer ionomers: 2. Viscoelastic and mechanical properties of sulphonated poly(styrene-ethylene/butylene-styrene),” *Polymer (Guildf)*, vol. 32, no. 15, pp. 2785–2792, 1991.
- [65] R. M. Grigorescu, F. Ciuprina, P. Ghioca, M. Ghiurea, L. Iancu, B. Spurcaci, and D. M. Panaitescu, “Mechanical and dielectric properties of SEBS modified by graphite inclusion and composite interface,” *J. Phys. Chem. Solids*, vol. 89, pp. 97–106, 2016.
- [66] R. A. Weiss, A. Sen, C. L. Willis, and L. A. Pottick, “Block copolymer ionomers: 1. Synthesis and physical properties of sulphonated poly(styrene-ethylene/butylene-styrene),” *Polymer (Guildf)*, vol. 32, no. 10, pp. 1867–1874, 1991.
- [67] R. P. Von Metzen and T. Stieglitz, “The effects of annealing on mechanical, chemical, and physical properties and structural stability of Parylene C,” *Biomed. Microdevices*, vol. 15, no. 5, pp. 727–735, 2013.
- [68] N. Ranjan and M. Mertig, “Dielectrophoretically assembled carbon nanotube-metal hybrid structures with reduced contact resistance,” *Phys. Status Solidi Basic Res.*, vol. 245, no. 10, pp. 2311–2314, 2008.
- [69] H. C. Koydemir, H. K ulah, and C.  zgen, “Solvent compatibility of parylene c film Layer,” *J. Microelectromechanical Syst.*, vol. 23, no. 2, pp. 298–307, 2014.
- [70] Y. Chang, T. Chiu, Y. Yang, Y. Tseng, X. Chen, P. Huang, and C. Rd, “Fatigue Response of Polyimide Thin Film under Cyclic Loading,” in *International Microsystem, Packaging, Assembly and Circuits Technology conference*, 2015, pp. 233–236.
- [71] A. Kahouli, A. Sylvestre, L. Ortega, F. Jomni, B. Yangui, M. Maillard, B. Berge, J. C. Robert, and J. Legrand, “Structural and dielectric study of parylene C thin films,” *Appl. Phys. Lett.*, vol. 94, no. 15, p. 152901, 2009.
- [72] H. J. Han, J. W. Jeong, S. R. Yang, C. Kim, H. G. Yoo, J. B. Yoon, J. H. Park, K. J. Lee, T. S. Kim, S. W. Kim, and Y. S. Jung, “Nanotransplantation Printing of Crystallographic-Orientation-Controlled Single-Crystalline Nanowire Arrays on Diverse Surfaces,” *ACS Nano*, vol. 11, no. 11, pp. 11642–11652, 2017.

- [73] N. P. Dasgupta, J. Sun, C. Liu, S. Brittman, S. C. Andrews, J. Lim, H. Gao, R. Yan, and P. Yang, “25th anniversary article: Semiconductor nanowires - Synthesis, characterization, and applications,” *Adv. Mater.*, vol. 26, no. 14, pp. 2137–2183, 2014.
- [74] J. Xu, S. Wang, G. N. Wang, C. Zhu, S. Luo, L. Jin, X. Gu, S. Chen, V. R. Feig, J. W. F. To, S. Rondeau-gagné, J. Park, B. C. Schroeder, C. Lu, J. Y. Oh, Y. Wang, Y. Kim, H. Yan, R. Sinclair, D. Zhou, G. Xue, B. Murmann, C. Linder, W. Cai, and J. B. Tok, “Highly stretchable polymer semiconductor films through the nanoconfinement effect,” *Science (80-. )*, vol. 355, pp. 59–64, 2017.
- [75] Y. Yao, H. Dong, and W. Hu, “Charge Transport in Organic and Polymeric Semiconductors for Flexible and Stretchable Devices,” *Adv. Mater.*, vol. 28, no. 22, pp. 4513–4523, 2016.
- [76] S. K. Lee, B. J. Kim, H. Jang, S. C. Yoon, C. Lee, B. H. Hong, J. A. Rogers, J. H. Cho, and J. H. Ahn, “Stretchable graphene transistors with printed dielectrics and gate electrodes,” *Nano Lett.*, vol. 11, no. 11, pp. 4642–4646, 2011.
- [77] T. Takahashi, K. Takei, A. G. Gillies, R. S. Fearing, and A. Javey, “Carbon Nanotube Active-Matrix Backplanes for Conformal Electronics and Sensors,” *Nano Lett.*, vol. 11, pp. 5408–5413, 2011.
- [78] S. Gupta, W. T. Navaraj, L. Lorenzelli, and R. Dahiya, “Ultra-thin chips for high-performance flexible electronics,” *npj Flex. Electron.*, vol. 2, no. 1, p. 8, 2018.
- [79] D.-Y. Khang, H. Jiang, Y. Huang, and J. A. Rogers, “A Stretchable Form of Single Crystal Silicon for High Performance Electronics on Rubber Substrates,” *Science (80-. )*, vol. 311, pp. 208–212, 2006.
- [80] K. S. Kim, Y. Zhao, H. Jang, S. Y. Lee, J. M. Kim, K. S. Kim, J.-H. Ahn, P. Kim, J.-Y. Choi, and B. H. Hong, “Large-scale pattern growth of graphene films for stretchable transparent electrodes,” *Nature*, vol. 457, no. 7230, pp. 706–710, 2009.
- [81] J. Young Oh, S. Rondeau-Gagné, Y.-C. Chiu, A. Chortos, F. Lissel, G.-J. Nathan Wang, B. C. Schroeder, T. Kurosawa, J. Lopez, T. Katsumata, J. Xu, C. Zhu, X. Gu, W.-G. Bae, Y. Kim, L. Jin, J. Won Chung, J. B-H Tok, and Z. Bao, “Intrinsically stretchable and healable semiconducting polymer for organic transistors,” *Nat. Publ. Gr.*, vol. 539, no. 7629, pp. 411–415, 2016.
- [82] D. J. Lipomi, H. Chong, M. Vosgueritchian, J. Mei, and Z. Bao, “Toward mechanically robust and intrinsically stretchable organic solar cells: Evolution of photovoltaic properties with tensile strain,” *Sol. Energy Mater. Sol. Cells*, vol. 107, pp. 355–365, 2012.
- [83] C. Müller, S. Goffri, D. W. Breiby, J. W. Andreasen, H. D. Chanzy, R. A. J. Janssen, M. M. Nielsen, C. P. Radano, H. Sirringhaus, P. Smith, and N. Stingelin-Stutzmann, “Tough, semiconducting polyethylene-poly(3-hexylthiophene) diblock copolymers,” *Adv. Funct. Mater.*, vol. 17, no. 15, pp. 2674–2679, 2007.

- [84] T. Sekitani, Y. Noguchi, K. Hata, T. Fukushima, T. Aida, and T. Someya, "A Rubberlike Stretchable Active Matrix Using Elastic Conductors," *Science* (80-. ), vol. 321, pp. 1468–1473, 2008.
- [85] Y. Zhang, C. J. Sheehan, J. Zhai, G. Zou, H. Luo, J. Xiong, Y. T. Zhu, and Q. X. Jia, "Polymer-embedded carbon nanotube ribbons for stretchable conductors," *Adv. Mater.*, vol. 22, no. 28, pp. 3027–3031, 2010.
- [86] S. Khan, W. Dang, L. Lorenzelli, and R. Dahiya, "Flexible Pressure Sensors Based on Screen-Printed P(VDF-TrFE) and P(VDF-TrFE)/MWCNTs," *IEEE Trans. Semicond. Manuf.*, vol. 28, no. 4, pp. 486–493, 2015.
- [87] W. Dang, S. Khan, L. Lorenzelli, V. Vinciguerra, and R. Dahiya, "Stretchable Interconnects using Screen Printed Nanocomposites of MWCNTs with PDMS and P(VDF-TrFE)," in *IEEE PRIME*, 2015.
- [88] K. Noda, E. Iwase, K. Matsumoto, and I. Shimoyama, "Stretchable liquid tactile sensor for robot-joints," in *IEEE International Conference on Robotics and Automation*, 2010, pp. 4212–4217.
- [89] N. Yogeswaran, W. Dang, W. T. Navaraj, D. Shakthivel, S. Khan, E. O. Polat, S. Gupta, H. Heidari, M. Kaboli, L. Lorenzelli, G. Cheng, and R. Dahiya, "New materials and advances in making electronic skin for interactive robots," *Adv. Robot.*, vol. 29, no. 21, pp. 1359–1373, 2015.
- [90] D. Alemu, H.-Y. Wei, K.-C. Ho, and C.-W. Chu, "Highly conductive PEDOT:PSS electrode by simple film treatment with methanol for ITO-free polymer solar cells," *Energy Environ. Sci.*, vol. 5, no. 11, p. 9662, 2012.
- [91] Y. H. Kim, C. Sachse, M. L. Machala, C. May, L. Müller-Meskamp, and K. Leo, "Highly Conductive PEDOT:PSS Electrode with Optimized Solvent and Thermal Post-Treatment for ITO-Free Organic Solar Cells," *Adv. Funct. Mater.*, vol. 21, no. 6, pp. 1076–1081, Mar. 2011.
- [92] T. Takano, H. Masunaga, A. Fujiwara, H. Okuzaki, and T. Sasaki, "PEDOT nanocrystal in highly conductive PEDOT:PSS polymer films," *Macromolecules*, vol. 45, no. 9, pp. 3859–3865, 2012.
- [93] S. Timpanaro, M. Kemerink, F. J. Touwslager, M. M. De Kok, and S. Schrader, "Morphology and conductivity of PEDOT/PSS films studied by scanning-tunneling microscopy," *Chem. Phys. Lett.*, vol. 394, pp. 339–343, 2004.
- [94] C. K. Cho, W. J. Hwang, K. Eun, S. H. Choa, S. I. Na, and H. K. Kim, "Mechanical flexibility of transparent PEDOT:PSS electrodes prepared by gravure printing for flexible organic solar cells," *Sol. Energy Mater. Sol. Cells*, vol. 95, no. 12, pp. 3269–3275, 2011.
- [95] C. Ladd, J. H. So, J. Muth, and M. D. Dickey, "3D printing of free standing liquid metal microstructures," *Adv. Mater.*, vol. 25, no. 36, pp. 5081–5085, 2013.

- [96] H.-J. Kim, C. Son, and B. Ziaie, "A multiaxial stretchable interconnect using liquid-alloy-filled elastomeric microchannels," *Appl. Phys. Lett.*, vol. 92, no. 1, p. 011904, 2008.
- [97] S. Kim, J. Lee, and B. Choi, "Stretching and twisting sensing with liquid-metal strain gauges printed on silicone elastomers," *IEEE Sens. J.*, vol. 15, no. 11, pp. 6077–6078, 2015.
- [98] D. Kim, D. Jung, J. H. Yoo, Y. Lee, W. Choi, G. S. Lee, K. Yoo, and J.-B. Lee, "Stretchable and bendable carbon nanotube on PDMS super-lyophobic sheet for liquid metal manipulation," *J. Micromechanics Microengineering*, vol. 24, no. 5, p. 055018 (1-6), 2014.
- [99] T. P. Yadav, R. M. Yadav, and D. P. Singh, "Mechanical Milling : a Top Down Approach for the Synthesis of Nanomaterials and Nanocomposites," *Nanosci. Nanotechnol.*, vol. 2, no. 3, pp. 22–48, 2012.
- [100] F. Delogu, G. Gorrasi, and A. Sorrentino, "Progress in Materials Science Fabrication of polymer nanocomposites via ball milling : Present status and future perspectives," *Prog. Mater. Sci.*, vol. 86, pp. 75–126, 2017.
- [101] C.-X. Liu and J.-W. Choi, "Improved Dispersion of Carbon Nanotubes in Polymers at High Concentrations," *Nanomaterials*, vol. 2, no. 4, pp. 329–347, Oct. 2012.
- [102] S. Khan, S. Tinku, L. Lorenzelli, and R. S. Dahiya, "Flexible tactile sensors using screen-printed P(VDF-TrFE) and MWCNT/PDMS composites," *IEEE Sens. J.*, vol. 15, no. 6, pp. 3146–3155, 2015.
- [103] S. De and J. N. Coleman, "The effects of percolation in nanostructured transparent conductors," *MRS Bull.*, vol. 36, no. 10, pp. 774–781, Oct. 2011.
- [104] S. Kumar, J. Y. Murthy, and M. A. Alam, "Percolating conduction in finite nanotube networks," *Phys. Rev. Lett.*, vol. 95, no. 6, p. 066802 (1-4), 2005.
- [105] D. A. Jack, C.-S. Yeh, Z. Liang, S. Li, J. G. Park, and J. C. Fielding, "Electrical conductivity modeling and experimental study of densely packed SWCNT networks," *Nanotechnology*, vol. 21, no. 19, 2010.
- [106] S. Colasanti, V. D. Bhatt, and P. Lugli, "3D Modeling of CNT Networks for Sensing Applications," in *IEEE PRIME*, 2014.
- [107] I. Balberg, "Tunnelling and percolation in lattices and the continuum," *J. Phys. D. Appl. Phys.*, vol. 42, no. 6, p. 064003, 2009.
- [108] X. Zheng, M. G. Forest, R. Vaia, M. Arlen, and R. Zhou, "A strategy for dimensional percolation in sheared nanorod dispersions," *Adv. Mater.*, vol. 19, no. 22, pp. 4038–4043, 2007.
- [109] W. S. Bao, S. A. Meguid, Z. H. Zhu, and G. J. Weng, "Tunneling resistance and its

- effect on the electrical conductivity of carbon nanotube nanocomposites,” *J. Appl. Phys.*, vol. 111, no. 9, p. 093726, 2012.
- [110] J. C. Halpin and J. L. Kardos, “The Halpin-Tsai equations: A review,” *Polym. Eng. Sci.*, vol. 16, no. 5, pp. 344–352, 1976.
- [111] L. E. Nielsen, “Generalized equation for the elastic moduli of composite materials,” *J. Appl. Phys.*, vol. 41, no. 11, pp. 4626–4627, 1970.
- [112] L. Li and D. D. . Chung, “Electrically conducting powder filled polyimidesiloxane,” *Composites*, vol. 22, no. 3, pp. 211–218, 1991.
- [113] H. Jung, J. Moon, D. Baek, J. Lee, Y. Choi, and J. Hong, “CNT / PDMS Composite Flexible Dry Electrodes for Long-Term ECG Monitoring,” *IEEE Trans. Biomed. Eng.*, vol. 59, no. 5, pp. 1472–1479, 2012.
- [114] Y. Hou, D. Wang, X.-M. Zhang, H. Zhao, J.-W. Zha, and Z.-M. Dang, “Positive piezoresistive behavior of electrically conductive alkyl-functionalized graphene/polydimethylsilicone nanocomposites,” *J. Mater. Chem. C*, no. March 2016, pp. 515–521, 2013.
- [115] W.-P. Shih, L.-C. Tsao, C.-W. Lee, M.-Y. Cheng, C. Chang, Y.-J. Yang, and K.-C. Fan, “Flexible temperature sensor array based on a graphite-polydimethylsiloxane composite,” *Sensors (Basel)*, vol. 10, no. 4, pp. 3597–610, Jan. 2010.
- [116] A. Celzard, E. McRae, J. F. Marêché, G. Furdin, and B. Sundqvist, “Conduction mechanisms in some graphite–polymer composites: Effects of temperature and hydrostatic pressure,” *J. Appl. Phys.*, vol. 83, no. 3, p. 1410, 1998.
- [117] N. Serra, T. Maedera, P. Lemaire, and P. Ryser, “Formulation of Composite Resistive Pastes for Micro-Heater Manufacturing,” *Procedia Chem.*, vol. 1, no. 1, pp. 48–51, Sep. 2009.
- [118] R. B. Mathur, S. R. Dhakate, D. K. Gupta, T. L. Dhami, and R. K. Aggarwal, “Effect of different carbon fillers on the properties of graphite composite bipolar plate,” *J. Mater. Process. Technol.*, vol. 203, no. 1–3, pp. 184–192, Jul. 2008.
- [119] V. S. Mironov, J. K. Kim, M. Ñ. Park, S. Lim, and W. K. Cho, “Comparison of electrical conductivity data obtained by four-electrode and four-point probe methods for graphite-based polymer composites,” *Polym. Test.*, vol. 26, pp. 547–555, 2007.
- [120] K. Nagata, H. Iwabuki, and H. Nigo, “Effect of particle size of graphites on electrical conductivity of graphite/polymer composite,” *Compos. Interfaces*, vol. 6, no. 5, pp. 483–495, Jan. 1998.
- [121] X. S. Du, M. Xiao, and Y. Z. Meng, “Synthesis and characterization of polyaniline/graphite conducting nanocomposites,” *J. Polym. Sci. Part B Polym. Phys.*, vol. 42, no. 10, pp. 1972–1978, May 2004.

- [122] F. D. C. Fim, J. M. Guterres, N. R. S. Basso, and G. B. Galland, "Polyethylene/graphite nanocomposites obtained by in situ polymerization," *J. Polym. Sci. Part A Polym. Chem.*, vol. 48, no. 3, pp. 692–698, Feb. 2010.
- [123] G. Chen, H. Wang, and W. Zhao, "Fabrication of highly ordered polymer/graphite flake composite with eminent anisotropic electrical property," *Polym. Adv. Technol.*, vol. 19, no. 8, pp. 1113–1117, Aug. 2008.
- [124] A. Khosla and B. L. Gray, "Preparation, characterization and micromolding of multi-walled carbon nanotube polydimethylsiloxane conducting nanocomposite polymer," *Mater. Lett.*, vol. 63, no. 13–14, pp. 1203–1206, May 2009.
- [125] J.-B. Lee and D.-Y. Khang, "Electrical and mechanical characterization of stretchable multi-walled carbon nanotubes/polydimethylsiloxane elastomeric composite conductors," *Compos. Sci. Technol.*, vol. 72, no. 11, pp. 1257–1263, Jun. 2012.
- [126] C.-X. Liu and J.-W. Choi, "Patterning conductive PDMS nanocomposite in an elastomer using microcontact printing," *J. Micromechanics Microengineering*, vol. 19, no. 8, p. 085019 (1-7), 2009.
- [127] J. Lu, M. Lu, A. Bermak, S. Member, and Y. Lee, "Study of Piezoresistance Effect of Carbon Nanotube-PDMS Composite Materials for Nanosensors," in *7th IEEE International Conference on Nanotechnology*, 2007, pp. 1240–1243.
- [128] M. Špírková, A. Duszová, R. Pore, J. Kredatusová, R. Bureš, M. Fáberová, and M. Šlouf, "Thermoplastic polybutadiene-based polyurethane / carbon nanofiber composites," *Compos. Part B*, vol. 67, pp. 434–440, 2014.
- [129] I. Moreno, N. Navascues, M. Arruebo, S. Irusta, and J. Santamaria, "Facile preparation of transparent and conductive polymer films based on silver nanowire/polycarbonate nanocomposites," *Nanotechnology*, vol. 24, no. 27, p. 275603 (1-11), 2013.
- [130] S.-P. Chen and Y.-C. Liao, "Highly stretchable and conductive silver nanowire thin films formed by soldering nanomesh junctions," *Phys. Chem. Chem. Phys.*, vol. 16, no. 37, pp. 19856–60, 2014.
- [131] P. Lee, J. Ham, J. Lee, S. Hong, S. Han, Y. D. Suh, S. E. Lee, J. Yeo, S. S. Lee, D. Lee, and S. H. Ko, "Highly stretchable or transparent conductor fabrication by a hierarchical multiscale hybrid nanocomposite," *Adv. Funct. Mater.*, vol. 36, pp. 5671–5678, 2014.
- [132] M. S. Lee, K. Lee, S. Y. Kim, H. Lee, J. Park, K. H. Choi, H. K. Kim, D. G. Kim, D. Y. Lee, S. Nam, and J. U. Park, "High-performance, transparent, and stretchable electrodes using graphene-metal nanowire hybrid structures," *Nano Lett.*, vol. 13, no. 6, pp. 2814–2821, 2013.
- [133] T. Araki, M. Nogi, K. Suganuma, M. Kogure, and O. Kiriara, "Printable and stretchable conductive wirings comprising silver flakes and elastomers," *IEEE Electron Device Lett.*, vol. 32, no. 10, pp. 1424–1426, 2011.

- [134] W. Hu, X. Niu, L. Li, S. Yun, Z. Yu, and Q. Pei, “Intrinsically stretchable transparent electrodes based on silver-nanowire-crosslinked-polyacrylate composites,” *Nanotechnology*, vol. 23, no. 34, p. 344002, 2012.
- [135] A. Larmagnac, S. Eggenberger, H. Janossy, and J. Vörös, “Stretchable electronics based on Ag-PDMS composites,” *Sci. Rep.*, vol. 4, p. 7254 (1-7), 2014.
- [136] V. Martinez, F. Stauffer, M. O. Adagunodo, C. Forro, J. Vörös, and A. Larmagnac, “Stretchable Silver Nanowire–Elastomer Composite Microelectrodes with Tailored Electrical Properties,” *ACS Appl. Mater. Interfaces*, vol. 7, no. 24, pp. 13467–13475, 2015.
- [137] L. Song, A. C. Myers, J. J. Adams, and Y. Zhu, “Stretchable and reversibly deformable radio frequency antennas based on silver nanowires,” *ACS Appl. Mater. Interfaces*, vol. 6, no. 6, pp. 4248–4253, 2014.
- [138] K. Tybrandt, F. Stauffer, and J. Vörös, “Multilayer Patterning of High Resolution Intrinsically Stretchable Electronics,” *Sci. Rep.*, vol. 6, p. 25641 (1-6), 2016.
- [139] F. Xu and Y. Zhu, “Highly conductive and stretchable silver nanowire conductors,” *Adv. Mater.*, vol. 24, no. 37, pp. 5117–5122, 2012.
- [140] K. K. Kim, S. Hong, H. M. Cho, J. Lee, Y. D. Suh, J. Ham, and S. H. Ko, “Highly Sensitive and Stretchable Multidimensional Strain Sensor with Prestrained Anisotropic Metal Nanowire Percolation Networks,” *Nano Lett.*, vol. 15, no. 8, pp. 5240–5247, 2015.
- [141] S. Yun, X. Niu, Z. Yu, W. Hu, P. Brochu, and Q. Pei, “Compliant silver nanowire-polymer composite electrodes for bistable large strain actuation,” *Adv. Mater.*, vol. 24, no. 10, pp. 1321–1327, 2012.
- [142] D. Doganay, S. Coskun, C. Kaynak, and H. E. Unalan, “Electrical, mechanical and thermal properties of aligned silver nanowire / polylactide nanocomposite films,” *Compos. Part B*, vol. 99, pp. 288–296, 2016.
- [143] W. Xu, Q. Xu, Q. Huang, R. Tan, W. Shen, and W. Song, “Electrically conductive silver nanowires-filled methylcellulose composite transparent films with high mechanical properties,” *Mater. Lett.*, vol. 152, pp. 173–176, 2015.
- [144] S. Narayanan, J. R. Hajzus, C. E. Treacy, M. R. Bockstaller, and L. M. Porter, “Polymer Embedded Silver-Nanowire Network Structures - A Platform for the Facile Fabrication of Flexible Transparent Conductors,” *ECS J. Solid State Sci. Technol.*, vol. 3, no. 11, pp. P363–P369, 2014.
- [145] J. Lee, P. Lee, H. B. Lee, S. Hong, I. Lee, J. Yeo, S. S. Lee, T. S. Kim, D. Lee, and S. H. Ko, “Room-temperature nanosoldering of a very long metal nanowire network by conducting-polymer-assisted joining for a flexible touch-panel application,” *Adv. Funct. Mater.*, vol. 23, no. 34, pp. 4171–4176, 2013.

- [146] L. Q. Cortes, A. Lonjon, E. Dantras, and C. Lacabanne, "High-performance thermoplastic composites poly(ether ketone ketone)/silver nanowires: Morphological, mechanical and electrical properties," *J. Non. Cryst. Solids*, vol. 391, pp. 106–111, 2014.
- [147] A. Lonjon, I. Caffrey, D. Carponcin, E. Dantras, and C. Lacabanne, "High electrically conductive composites of Polyamide 11 filled with silver nanowires: Nanocomposites processing, mechanical and electrical analysis," *J. Non. Cryst. Solids*, vol. 376, pp. 199–204, 2013.
- [148] M. Sureshkumar, H. Y. Na, K. H. Ahn, and S. J. Lee, "Conductive nanocomposites based on polystyrene microspheres and silver nanowires by latex blending," *ACS Appl. Mater. Interfaces*, vol. 7, no. 1, pp. 756–764, 2015.
- [149] S. Choi, J. Park, W. Hyun, J. Kim, J. Kim, Y. B. Lee, C. Song, H. J. Hwang, J. H. Kim, T. Hyeon, and D. H. Kim, "Stretchable Heater Using Ligand-Exchanged Silver Nanowire Nanocomposite for Wearable Articular Thermotherapy," *ACS Nano*, vol. 9, no. 6, pp. 6626–6633, 2015.
- [150] Y. Tang, S. Gong, Y. Chen, L. W. Yap, and W. Cheng, "Manufacturable Conducting Rubber Ambers and Stretchable Conductors from Copper Nanowire Aerogel Monoliths," *ACS Nano*, vol. 8, no. 6, pp. 5707–5714, 2014.
- [151] H. Im, S. Jung, J. Jin, D. Lee, J. Lee, D. Lee, and J. Lee, "Flexible Transparent Conducting Hybrid Film Using a Surface- Embedded Copper Nanowire Network : A Highly Oxidation-Resistant Copper Nanowire Electrode for Flexible Optoelectronics," *ACS Nano*, vol. 8, no. 10, pp. 10973–10979, 2014.
- [152] G. A. Gelves, B. Lin, U. Sundararaj, and J. A. Haber, "Low electrical percolation threshold of silver and copper nanowires in polystyrene composites," *Adv. Funct. Mater.*, vol. 16, no. 18, pp. 2423–2430, 2006.
- [153] B. W. An, E. J. Gwak, K. Kim, Y. C. Kim, J. Jang, J. Y. Kim, and J. U. Park, "Stretchable, Transparent Electrodes as Wearable Heaters Using Nanotrough Networks of Metallic Glasses with Superior Mechanical Properties and Thermal Stability," *Nano Lett.*, vol. 16, no. 1, pp. 471–478, 2016.
- [154] A. Lonjon, L. Laffont, P. Demont, E. Dantras, and C. Lacabanne, "New Highly Conductive Nickel Nanowire-Filled P ( VDF-TrFE ) Copolymer Nanocomposites : Elaboration and Structural Study," *J. Phys. Chem. C*, vol. 113, pp. 12002–12006, 2009.
- [155] A. Lonjon, L. Laffont, P. Demont, E. Dantras, and C. Lacabanne, "Structural and electrical properties of gold nanowires/P(VDF-TrFE) nanocomposites," *J. Phys. D. Appl. Phys.*, vol. 43, p. 345401, 2010.
- [156] J. Ge, L. Sun, F. R. Zhang, Y. Zhang, L. A. Shi, H. Y. Zhao, H. W. Zhu, H. L. Jiang, and S. H. Yu, "A Stretchable Electronic Fabric Artificial Skin with Pressure-, Lateral Strain-, and Flexion-Sensitive Properties," *Adv. Mater.*, vol. 28, no. 4, pp. 722–728, 2016.



- [157] M.-Y. Cheng, C.-M. Tsao, Y.-Z. Lai, and Y.-J. Yang, "The development of a highly twistable tactile sensing array with stretchable helical electrodes," *Sensors Actuators A Phys.*, vol. 166, no. 2, pp. 226–233, Apr. 2011.
- [158] M. Y. Cheng, C. M. Tsao, and Y. J. Yang, "An anthropomorphic robotic skin using highly twistable tactile sensing array," *Proc. 2010 5th IEEE Conf. Ind. Electron. Appl. ICIEA 2010*, pp. 650–655, 2010.
- [159] E. Bonderover and S. Wagner, "A woven inverter circuit for e-textile applications," *IEEE Electron Device Lett.*, vol. 25, no. 5, pp. 295–297, 2004.
- [160] M. Hamed, R. Forchheimer, and O. Inganäs, "Towards woven logic from organic electronic fibres," *Nat. Mater.*, vol. 6, no. 5, pp. 357–362, 2007.
- [161] T. Hoshi and H. Shinoda, "Robot skin based on touch-area-sensitive tactile element," in *IEEE International Conference on Robotics and Automation*, 2006, pp. 3463–3468.
- [162] B. Huyghe, H. Rogier, J. Vanfleteren, and F. Axisa, "Design and Manufacturing of Stretchable High-Frequency Interconnects," *IEEE Trans. Adv. Packag.*, vol. 31, no. 4, pp. 802–808, 2008.
- [163] D. Brosteaux, M. Gonzalez, and J. Vanfleteren, "Design and Fabrication of Elastic Interconnections for Stretchable Electronic Circuits," *IEEE Electron Device Lett.*, vol. 28, no. 7, pp. 552–554, Jul. 2007.
- [164] R. Verplancke, F. Bossuyt, D. Cuypers, and J. Vanfleteren, "Thin-film stretchable electronics technology based on meandering interconnections: fabrication and mechanical performance," *J. Micromechanics Microengineering*, vol. 22, no. 1, Jan. 2012.
- [165] D.-H. Kim, Z. Liu, Y.-S. Kim, J. Wu, J. Song, H.-S. Kim, Y. Huang, K.-C. Hwang, Y. Zhang, and J. A. Rogers, "Optimized structural designs for stretchable silicon integrated circuits," *Small*, vol. 5, no. 24, pp. 2841–2847, Dec. 2009.
- [166] Y. Zhang, H. Fu, Y. Su, S. Xu, H. Cheng, J. A. Fan, K. C. Hwang, J. A. Rogers, and Y. Huang, "Mechanics of ultra-stretchable self-similar serpentine interconnects," *Acta Mater.*, vol. 61, no. 20, pp. 7816–7827, 2013.
- [167] Z. Fan, Y. Zhang, Q. Ma, F. Zhang, H. Fu, K. Hwang, and Y. Huang, "A finite deformation model of planar serpentine interconnects for stretchable electronics," *Int. J. Solids Struct.*, vol. 91, pp. 46–54, 2016.
- [168] H. Hocheng and C.-M. Chen, "Design, fabrication and failure analysis of stretchable electrical routings," *Sensors (Basel)*, vol. 14, no. 7, pp. 11855–77, Jan. 2014.
- [169] Y. Sun, W. M. Choi, H. Jiang, Y. Y. Huang, and J. A. Rogers, "Controlled buckling of semiconductor nanoribbons for stretchable electronics," *Nat. Nanotechnol.*, vol. 1, no. 3, pp. 201–207, 2006.

- [170] J. Rogers, Y. Huang, O. G. Schmidt, and D. H. Gracias, “Origami MEMS and NEMS,” *MRS Bull.*, vol. 41, no. 02, pp. 123–129, 2016.
- [171] H. Lee, C. Bae, L. T. Duy, I. Sohn, D. Kim, Y. Song, Y. Kim, and N. Lee, “Mogul-Patterned Elastomeric Substrate for Stretchable Electronics,” *Adv. Mater.*, vol. 28, pp. 3069–77, 2016.
- [172] Y. Yu, J. Zeng, C. Chen, Z. Xie, R. Guo, Z. Liu, X. Zhou, Y. Yang, and Z. Zheng, “Three-dimensional compressible and stretchable conductive composites,” *Adv. Mater.*, vol. 26, no. 5, pp. 810–815, 2014.
- [173] X. Gui, A. Cao, J. Wei, H. Li, Y. Jia, Z. Li, L. Fan, K. Wang, H. Zhu, and D. Wu, “Soft , Highly Conductive Nanotube Compressibility,” *ACS Nano*, vol. 4, no. 4, pp. 2320–6, 2010.
- [174] Z. Chen, W. Ren, L. Gao, B. Liu, S. Pei, and H.-M. Cheng, “Three-dimensional flexible and conductive interconnected graphene networks grown by chemical vapour deposition,” *Nat. Mater.*, vol. 10, no. 6, pp. 424–8, 2011.
- [175] C. F. Guo, T. Sun, Q. Liu, Z. Suo, and Z. Ren, “Highly stretchable and transparent nanomesh electrodes made by grain boundary lithography,” *Nat. Commun.*, vol. 5, 2014.
- [176] A. Bagal, E. C. Dandley, J. Zhao, X. A. Zhang, C. J. Oldham, G. N. Parsons, and C.-H. Chang, “Multifunctional nano-accordion structures for stretchable transparent conductors,” *Mater. Horizons*, vol. 2, no. 5, pp. 486–494, 2015.
- [177] F. Bossuyt, T. Vervust, and J. Vanfleteren, “Stretchable Electronics Technology for Large Area Applications: Fabrication and Mechanical Characterization,” *IEEE Trans. Components, Packag. Manuf. Technol.*, vol. 3, no. 2, pp. 229–235, Feb. 2013.
- [178] S. Ha, Y. Huang, J. A. Rogers, H. C. Ko, G. Shin, S. Wang, M. P. Stoykovich, J. W. Lee, D. Kim, J. S. Ha, Y. Huang, K. Hwang, and A. Rogers, “Curvilinear Electronics Formed Using Silicon Membrane Circuits and Elastomeric Transfer Elements,” *Small*, vol. 5, no. 23, pp. 2703–2709, 2009.
- [179] C. García Núñez, F. Liu, W. T. Navaraj, A. Christou, D. Shakthivel, and R. Dahiya, “Heterogeneous integration of contact-printed semiconductor nanowires for high-performance devices on large areas,” *Microsystems Nanoeng.*, vol. 4, no. 1, p. 22, 2018.
- [180] C. G. Núñez, F. Liu, S. Xu, and R. Dahiya, *Integration Techniques for Micro/Nanostructure-Based Large-Area Electronics (Elements in Flexible and Large-Area Electronics)*. Cambridge University Press, 2018.
- [181] Z. Fan, J. C. Ho, Z. A. Jacobson, R. Yerushalmi, R. L. Alley, H. Razavi, and A. Javey, “Wafer-scale assembly of highly ordered semiconductor nanowire arrays by contact printing,” *Nano Lett.*, vol. 8, no. 1, pp. 20–25, 2008.

- [182] T.-H. Kim, A. Carlson, J.-H. Ahn, S. M. Won, S. Wang, Y. Huang, and J. a. Rogers, “Kinetically controlled, adhesiveless transfer printing using microstructured stamps,” *Appl. Phys. Lett.*, vol. 94, no. 11, p. 113502, 2009.
- [183] G. M. McClelland, M. W. Hart, C. T. Rettner, M. E. Best, K. R. Carter, and B. D. Terris, “Nanoscale patterning of magnetic islands by imprint lithography using a flexible mold,” *Appl. Phys. Lett.*, vol. 81, no. 8, pp. 1483–1485, 2002.
- [184] C.-X. Liu and J.-W. Choi, “Patterning conductive PDMS nanocomposite in an elastomer using microcontact printing,” *J. Micromechanics Microengineering*, vol. 19, no. 8, p. 085019 (1-7), Aug. 2009.
- [185] V. K. Sangwan, V. W. Ballarotto, D. R. Hines, M. S. Fuhrer, and E. D. Williams, “Controlled growth, patterning and placement of carbon nanotube thin films,” *Solid. State. Electron.*, vol. 54, no. 10, pp. 1204–1210, Oct. 2010.
- [186] A. Abdelhalim, A. Abdellah, G. Scarpa, and P. Lugli, “Fabrication of carbon nanotube thin films on flexible substrates by spray deposition and transfer printing,” *Carbon N. Y.*, vol. 61, pp. 72–79, Sep. 2013.
- [187] A. Bédier, F. Seichepine, E. Flahaut, and C. Vieu, “A simple and versatile micro contact printing method for generating carbon nanotubes patterns on various substrates,” *Microelectron. Eng.*, vol. 97, pp. 301–305, Sep. 2012.
- [188] S. Khan, L. L. Member, R. Dahiya, and S. Member, “Flexible MISFET Devices From Transfer Printed Si Microwires and Spray Coating,” *J. Electron Devices Soc.*, vol. 4, no. 4, pp. 189–196, 2016.
- [189] S. Khan, N. Yogeswaran, W. Taube, L. Lorenzelli, and R. Dahiya, “Flexible FETs using ultrathin Si microwires embedded in solution processed dielectric and metal layers,” *J. Micromechanics Microengineering*, vol. 25, no. 12, p. 125019, 2015.
- [190] M. Singh, H. M. Haverinen, P. Dhagat, and G. E. Jabbour, “Inkjet printing-process and its applications,” *Adv. Mater.*, vol. 22, no. 6, pp. 673–685, 2010.
- [191] P. F. Moonen, I. Yakimets, and J. Huskens, “Fabrication of transistors on flexible substrates: From mass-printing to high-resolution alternative lithography strategies,” *Adv. Mater.*, vol. 24, no. 41, pp. 5526–5541, 2012.
- [192] J. M. Verilhac, M. Benwadih, A. L. Seiler, S. Jacob, C. Bory, J. Bablet, M. Heitzman, J. Tallal, L. Barbut, P. Frère, G. Sicard, R. Gwoziecki, I. Chartier, R. Coppard, and C. Serbutoviez, “Step toward robust and reliable amorphous polymer field-effect transistors and logic functions made by the use of roll to roll compatible printing processes,” *Org. Electron. physics, Mater. Appl.*, vol. 11, no. 3, pp. 456–462, 2010.
- [193] B. J. De Gans and U. S. Schubert, “Inkjet printing of polymer micro-arrays and libraries: Instrumentation, requirements, and perspectives,” *Macromol. Rapid Commun.*, vol. 24, no. 11, pp. 659–666, 2003.

- [194] N. P. Pham, J. N. Burghartz, and P. M. Sarro, "Spray coating of photoresist for pattern transfer on high topography surfaces," *J. Micromechanics Microengineering*, vol. 15, no. 4, pp. 691–697, 2005.
- [195] C. Girotto, B. P. Rand, J. Genoe, and P. Heremans, "Exploring spray coating as a deposition technique for the fabrication of solution-processed solar cells," *Sol. Energy Mater. Sol. Cells*, vol. 93, no. 4, pp. 454–458, 2009.
- [196] G. Susanna, L. Salamandra, T. M. Brown, A. Di Carlo, F. Brunetti, and A. Reale, "Airbrush spray-coating of polymer bulk-heterojunction solar cells," *Sol. Energy Mater. Sol. Cells*, vol. 95, no. 7, pp. 1775–1778, 2011.
- [197] D. Tobjörk and R. Österbacka, "Paper Electronics," *Adv. Mater.*, vol. 23, pp. 1935–1961, 2011.
- [198] D. Gross, W. Hauger, J. Schroeder, W.A.Wall, and J.Bonet, *Engineering Mechanics* 2. 2011.
- [199] X. Chen, B. L. Kirsch, R. Senter, S. H. Tolbert, and V. Gupta, "Tensile testing of thin films supported on compliant substrates," *Mech. Mater.*, vol. 41, no. 7, pp. 839–848, 2009.
- [200] A. C. Ferrari, "Raman spectroscopy of graphene and graphite: Disorder, electron-phonon coupling, doping and nonadiabatic effects," *Solid State Commun.*, vol. 143, pp. 47–57, 2007.
- [201] Z. Piatek and B. Baron, "Exact Closed Form Formula for Self Inductance of Conductor of Rectangular Cross Section," *Prog. Electromagn. Res. M*, vol. 26, pp. 225–236, 2012.
- [202] L. Yu, "The adhesion of poly(dimethylsiloxane) to silica substrates," 2014.
- [203] B. Miliare, M. Thomas, A. Ferreira, H. Xu, M. Holesinger, and V. I. Vullev, "Dependence of the quality of adhesion between poly(dhnethylsiloxane) and glass surfaces on the conditions of treatment with oxygen plasma," *Langmuir*, vol. 24, no. 22, pp. 13218–13224, 2008.
- [204] S. Tinku, E. Iacob, L. Lorenzelli, and R. Dahiya, "Surface Characterization Of Polydimethylsiloxane : An AFM Study," in *2015 XVIII AISEM Annual Conference*, 2015.
- [205] S. J. Yu, Y. P. Du, Y. D. Sun, Q. L. Ye, and H. Zhou, "Wrinkling patterns in metal films sputter deposited on viscoelastic substrates," *Thin Solid Films*, vol. 638, pp. 230–235, 2017.
- [206] X. Crispin, F. L. E. Jakobsson, M. Berggren, and E. Al, "The origin of the high conductivity of poly(3,4-ethylenedioxythiophene)-poly(styrenesulfonate) (PEDOT-PSS) plastic electrodes," *Chem. Mater.*, vol. 18, no. 4, pp. 4354–4360, 2006.

- [207] O. P. Dimitriev, D. A. Grinko, Y. V. Noskov, N. A. Ogurtsov, and A. A. Pud, "PEDOT:PSS films—Effect of organic solvent additives and annealing on the film conductivity," *Synth. Met.*, vol. 159, no. 21–22, pp. 2237–2239, 2009.
- [208] D. P. Kepić, Z. M. Marković, S. P. Jovanović, D. B. Peruško, M. D. Budimir, I. D. Holclajtner-Antunović, V. B. Pavlović, and B. M. Todorović Marković, "Preparation of PEDOT:PSS thin films doped with graphene and graphene quantum dots," *Synth. Met.*, vol. 198, pp. 150–154, 2014.
- [209] W. Dang, V. Vinciguerra, L. Lorenzelli, and R. Dahiya, "Metal-organic Dual Layer Structure for Stretchable Interconnects," *Procedia Eng.*, vol. 168, pp. 1559–1562, 2016.
- [210] Datasheet, "PI2525 HD MicroSystems," 2012.
- [211] D. Quesada-González and A. Merkoçi, "Mobile phone-based biosensing: An emerging 'diagnostic and communication' technology," *Biosens. Bioelectron.*, vol. 92, no. October 2016, pp. 549–562, 2017.
- [212] M. Haghi, K. Thurow, and R. Stoll, "Wearable devices in medical internet of things: Scientific research and commercially available devices," *Healthc. Inform. Res.*, vol. 23, no. 1, pp. 4–15, 2017.
- [213] N. M. Farandos, A. K. Yetisen, M. J. Monteiro, C. R. Lowe, and S. H. Yun, "Contact lens sensors in ocular diagnostics," *Adv. Healthc. Mater.*, vol. 4, no. 6, pp. 792–810, 2015.
- [214] W. Gao, S. Emaminejad, H. Y. Y. Nyein, S. Challa, K. Chen, A. Peck, H. M. Fahad, H. Ota, H. Shiraki, D. Kiriya, D.-H. Lien, G. A. Brooks, R. W. Davis, and A. Javey, "Fully integrated wearable sensor arrays for multiplexed in situ perspiration analysis," *Nature*, vol. 529, no. 7587, pp. 509–514, 2016.
- [215] W. P. Nikolajek and H. M. Emrich, "pH of sweat of patients with cystic fibrosis," *Klin. Wochenschr.*, vol. 54, no. 6, pp. 287–288, 1976.
- [216] D. Czarnowski and J. Górski, "Sweat ammonia excretion during submaximal cycling exercise.," *J. App. Physiol.*, vol. 70, pp. 371–374, 1991.
- [217] Z. Sonner, E. Wilder, J. Heikenfeld, G. Kasting, F. Beyette, D. Swaile, F. Sherman, J. Joyce, J. Hagen, N. Kelley-Loughnane, and R. Naik, "The microfluidics of the eccrine sweat gland, including biomarker partitioning, transport, and biosensing implications," *Biomicrofluidics*, vol. 9, no. 3, pp. 1–19, 2015.
- [218] S. R. Corrie, J. W. Coffey, J. Islam, K. A. Markey, and M. A. F. Kendall, "Blood, sweat, and tears: developing clinically relevant protein biosensors for integrated body fluid analysis," *Analyst*, vol. 140, no. 13, pp. 4350–4364, 2015.
- [219] S. Tinku, C. Collini, L. Lorenzelli, and F. B. Kessler, "Smart Contact Lens Using Passive Structures," in *Sensors, IEEE*, 2014.

- [220] A. J. Bandodkar, V. W. S. Hung, W. Jia, G. Valdés-Ramírez, J. R. Windmiller, A. G. Martinez, J. Ramírez, G. Chan, K. Kerman, and J. Wang, “Tattoo-based potentiometric ion-selective sensors for epidermal pH monitoring,” *Analyst*, vol. 138, no. 1, pp. 123–128, 2013.
- [221] H. Lee, C. Song, Y. S. Hong, M. S. Kim, H. R. Cho, T. Kang, K. Shin, S. H. Choi, T. Hyeon, and D.-H. Kim, “Wearable/disposable sweat-based glucose monitoring device with multistage transdermal drug delivery module,” *Sci. Adv.*, vol. 3, no. 3, p. e1601314, 2017.
- [222] V. F. Curto, C. Fay, S. Coyle, R. Byrne, C. O’Toole, C. Barry, S. Hughes, N. Moyna, D. Diamond, and F. Benito-Lopez, “Real-time sweat pH monitoring based on a wearable chemical barcode micro-fluidic platform incorporating ionic liquids,” *Sensors Actuators, B Chem.*, vol. 171–172, pp. 1327–1334, 2012.
- [223] S. Anastasova, B. Crewther, P. Bembnowicz, V. Curto, H. M. Ip, B. Rosa, and G. Z. Yang, “A wearable multisensing patch for continuous sweat monitoring,” *Biosens. Bioelectron.*, vol. 94, p. 730, 2017.
- [224] J. Kim, A. Banks, H. Cheng, Z. Xie, S. Xu, K. I. Jang, J. W. Lee, Z. Liu, P. Gutruf, X. Huang, P. Wei, F. Liu, K. Li, M. Dalal, R. Ghaffari, X. Feng, Y. Huang, S. Gupta, U. Paik, and J. A. Rogers, “Epidermal electronics with advanced capabilities in near-field communication,” *Small*, vol. 11, no. 8, pp. 906–912, 2015.
- [225] G. Liu, C. Ho, N. Slappey, Z. Zhou, S. E. Snelgrove, M. Brown, A. Grabinski, X. Guo, Y. Chen, K. Miller, J. Edwards, and T. Kaya, “A wearable conductivity sensor for wireless real-time sweat monitoring,” *Sensors Actuators, B Chem.*, vol. 227, pp. 35–42, 2016.
- [226] N. Matsuhisa, M. Kaltenbrunner, T. Yokota, H. Jinno, K. Kuribara, T. Sekitani, and T. Someya, “Printable elastic conductors with a high conductivity for electronic textile applications,” *Nat. Commun.*, vol. 6, p. 7461, 2015.
- [227] S. S. Mohan, M. D. M. Hershenson, S. P. Boyd, and T. H. Lee, “Simple accurate expressions for planar spiral inductances,” *IEEE J. Solid-State Circuits*, vol. 34, no. 10, pp. 1419–1420, 1999.
- [228] I. Cesarino, C. Gouveia-Caridade, R. Pauliukaite, É. T. G. Cavaleiro, and C. M. A. Bretta, “Characterization and application of bismuth-film modified graphite-polyurethane composite electrodes,” *Electroanalysis*, vol. 22, no. 13, pp. 1437–1445, 2010.
- [229] B. Lakard, O. Segut, S. Lakard, G. Herlem, and T. Gharbi, “Potentiometric miniaturized pH sensors based on polypyrrole films,” *Sensors Actuators, B Chem.*, vol. 122, no. 1, pp. 101–108, 2007.
- [230] W. Dang, E. S. Hosseini, and R. Dahiya, “Soft Robotic Finger with Integrated Stretchable Strain Sensor,” in *2018 IEEE Sensors*, 2018, pp. 1–4.
- [231] M. Cianchetti, T. Ranzani, G. Gerboni, T. Nanayakkara, K. Althoefer, P. Dasgupta,

- and A. Menciassi, "Soft Robotics Technologies to Address Shortcomings in Today's Minimally Invasive Surgery: The STIFF-FLOP Approach," *Soft Robot.*, vol. 1, no. 2, pp. 122–131, 2014.
- [232] P. Polygerinos, S. Lyne, Z. Wang, L. F. Nicolini, B. Mosadegh, G. M. Whitesides, and C. J. Walsh, "Towards a soft pneumatic glove for hand rehabilitation," *IEEE Int. Conf. Intell. Robot. Syst.*, pp. 1512–1517, 2013.
- [233] S. I. Rich, R. J. Wood, and C. Majidi, "Untethered soft robotics," *Nat. Electron.*, vol. 1, no. 2, pp. 102–112, 2018.
- [234] D. Rus and M. T. Tolley, "Design, fabrication and control of soft robots," *Nature*, vol. 521, no. 7553, pp. 467–475, 2015.
- [235] A. Rafsanjani, Y. Zhang, B. Liu, S. M. Rubinstein, and K. Bertoldi, "Kirigami skins make a simple soft actuator crawl," *Sci. Robot.*, vol. 3, p. eaar7555 (1-7), 2018.
- [236] A. D. Marchese, C. D. Onal, and D. Rus, "Autonomous Soft Robotic Fish Capable of Escape Maneuvers Using Fluidic Elastomer Actuators," *Soft Robot.*, vol. 1, no. 1, pp. 75–87, 2014.
- [237] R. L. Truby, M. Wehner, A. K. Grosskopf, D. M. Vogt, S. G. M. Uzel, R. J. Wood, and J. A. Lewis, "Soft Somatosensitive Actuators via Embedded 3D Printing," *Adv. Mater.*, p. 1706383 (1-8), 2018.
- [238] W. Dang, V. Vinciguerra, L. Lorenzelli, and R. Dahiya, "Printable stretchable interconnects," *Flex. Print. Electron.*, vol. 2, p. 013003, 2017.
- [239] U. C. Wejinya, N. Xi, K. W. C. Lai, J. Zhang, and Y. Shen, "Design and generation of DEP force for assembly of CNT-based nano devices," *2008 IEEE/RSJ Int. Conf. Intell. Robot. Syst. IROS*, pp. 925–930, 2008.
- [240] N. Hu, Y. Karube, C. Yan, Z. Masuda, and H. Fukunaga, "Tunneling effect in a polymer/carbon nanotube nanocomposite strain sensor," *Acta Mater.*, vol. 56, no. 13, pp. 2929–2936, 2008.
- [241] M. Amjadi, K. U. Kyung, I. Park, and M. Sitti, "Stretchable, Skin-Mountable, and Wearable Strain Sensors and Their Potential Applications: A Review," *Adv. Funct. Mater.*, vol. 26, no. 11, pp. 1678–1698, 2016.
- [242] W. Dang, L. Lorenzelli, V. Vinciguerra, and R. Dahiya, "Hybrid Structure of Stretchable Interconnect for Reliable E-skin Application," in *Industrial Electronics (ISIE)-IEEE*, 2017, pp. 2093–2096.